UNIVERSITÀ DEGLI STUDI DI PADOVA

DIPARTIMENTO DI FISICA E ASTRONOMIA "GALILEO GALILEI"

Master Degree in PHYSICS OF DATA

Final dissertation

COMPARISON OF EXPERIMENTAL AND SIMULATED BEAMLET DEFLECTION IN A MITICA-LIKE EXTRACTION SYSTEM AT BATMAN UPGRADE

Thesis supervisor
PROF. DR. URSEL FANTZ
IPP Garching

Candidate
BEATRICE SEGALINI
Student ID 1234430

Thesis co-supervisors
DR. ANDREW HURLBATT *IPP Garching*
DR. NIEK DEN HARDER *IPP Garching*
DR. CHRISTIAN WIMMER *IPP Garching*
DR. GIANLUIGI SERIANNI *Università degli Studi di Padova*

ACADEMIC YEAR 2020/2021

Abstract

In collaboration with ITER, a MITICA-like extraction was installed at the BATMAN Upgrade test facility in 2021 (BUG-MLE). One main difference to the previous extraction system is the presence of additional deflection compensation magnets which are designed to suppress the row-wise zig-zag deflection of the accelerated negative ions caused by the co-extracted electron suppression magnets, mounted in the second grid of the extraction and acceleration system.

The effect of the deflection correction magnets was characterized in dedicated scans with the available beam diagnostic tools (Carbon Fiber Composite tile calorimetry and Beam Emission Spectroscopy). Since the correction magnets are installed only in the upper grid half, the corrected beam can be directly compared to an uncompensated beam.

The experimental investigations are accompanied by simulations. IBSimu is used to model the beamlet formation and ion-optics inside the extraction system. The in-house developed BBCNI code is exploited to track the particles towards the CFC and generate synthetic beamlet emission spectra.

The work focuses on physics interpretation by directly comparing measured and synthetic data. In particular, after outlining the main theoretical aspects behind the BUG-MLE experiment, a series of simulations is performed with both of the aforementioned codes, allowing a detailed understanding of the expected results and providing insight on both the robustness of the horizontal deflection correction and its impact on the estimated beamlet divergence.

Finally, the experimental outcomes are presented and analysed, from both of the diagnostic tools, and compared with the simulations in order to evaluate the action of the additional magnets in different conditions.

Contents

Listing of acronyms

ADCM ..... Asymmetric Deflection Compensation Magnet(s)

AG ..... Acceleration Grid

BATMAN ... Bavarian Test Machine for Negative Ions

BBCNI ..... Bavarian Beam Code for Negative Ions

BES ..... Beam Emission Spectroscopy

BUG ..... BATMAN Upgrade

BUG-MLE ... BUG Mitica-Like Extraction

CESM ..... Co-Extracted Electrons Suppression Magnet(s)

CFC ..... Carbon Fibre Composite

EG ..... Extraction Grid

GG ..... Grounded Grid

FF ..... Filter Field

IPP ..... Max Planck Institute for Plasma Physics

LOS ..... Line of Sight

MITICA ..... Megavolt ITER Injector Concept Advancement

NBI ..... Neutral Beam Injection/Injectors

NITS ..... Negative Ion Test Stand

PG ..... Plasma Grid

PRIMA ..... Padua Research on ITER Megavolt Accelerator

SPIDER ..... Source for Production of Ion of Deuterium Extracted from RF plasma

1 Introduction

1.1. Fusion and the energy problem

With the global population swelling and industrialisation on the rise in developing nations, humanity's hunger for energy has reached unprecedented levels. As shown in Figure 1.1, world energy consumption has been almost constantly on the rise, with a particularly steep increase in the last 50 years. Covid-19 pandemic only slightly decelerated this process during 2020, but as reported in Figure 1.2, the trend is predicted to return to its previous state.

Observing the graph 1.1, it is clear that globally the largest amount of energy is derived from oil, followed by coal, gas, and only then by a non-fossil fuel power. The massive use of fossil fuels impacts significantly on carbon dioxide emissions, which are the primary driver of global climate change. It is widely recognised that, to avoid the worst impacts of climate change, the world needs to urgently reduce emissions.

Thus, one of the most relevant issues for scientific research concerns the development of new, renewable energy sources, and in this framework, nuclear fusion could represent one of the solutions for the world energy issue.

Nuclear fusion energy can be produced with many possible reactions, although only some of them are energetically favourable. The main ones are the following:

$$^2D + {}^2D \overset{50\%}{\Rightarrow} {}^3He(0.82\,\text{MeV}) + n(2.45\,\text{MeV}) \tag{1.1}$$

$$^2D + {}^2D \overset{50\%}{\Rightarrow} {}^3T(1.01\,\text{MeV}) + {}^1H(3.02\,\text{MeV}) \tag{1.2}$$

$$^2D + {}^3T \Rightarrow {}^4He(3.5\,\text{MeV}) + n(14.1\,\text{MeV}) \tag{1.3}$$

$$^2D + {}^4He \Rightarrow {}^4He(3.6\,\text{MeV}) + {}^1H(14.7\,\text{MeV}) \tag{1.4}$$

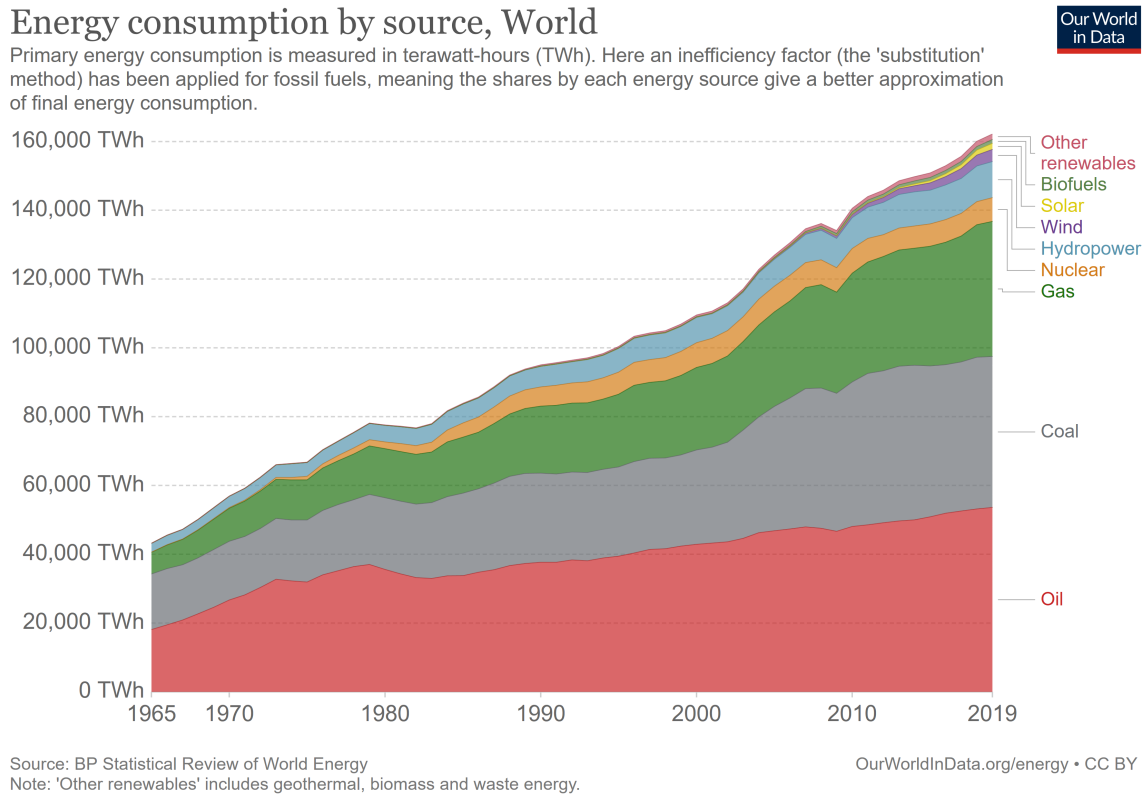

Figure 1.1: Global energy consumption in TW h divided by source, from 1965 to 2019. Interactive plot available here: [1].

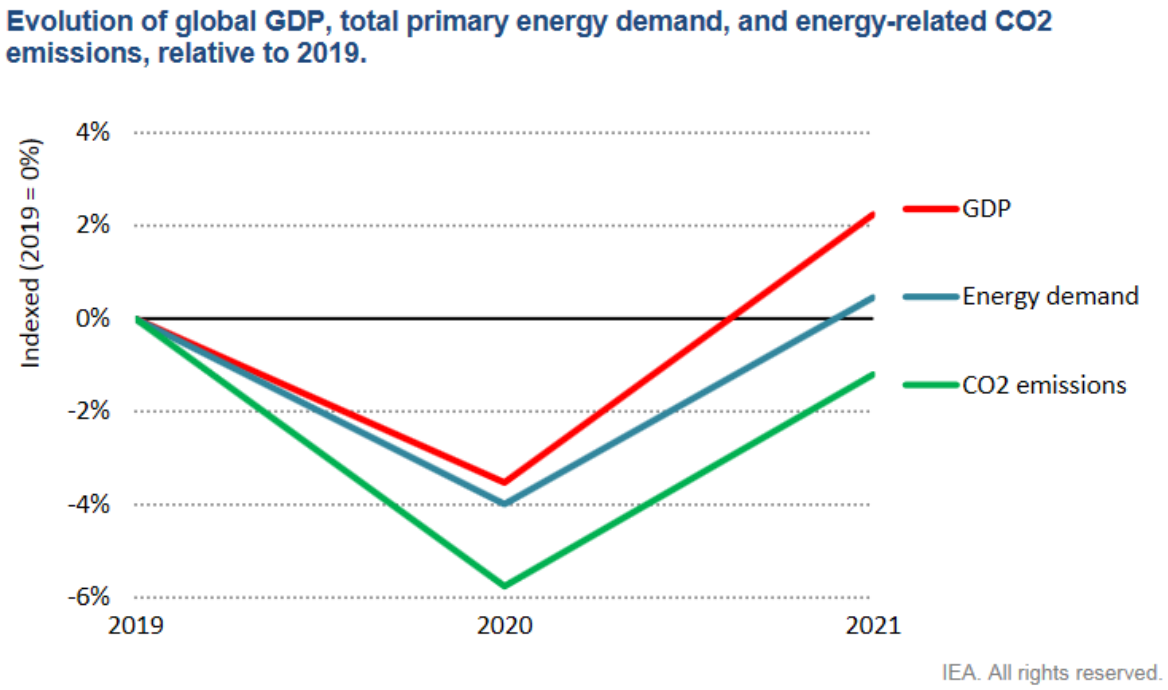

Figure 1.2: Predictions of global gross domestic product (GDP), energy demand and CO2 emissions for 2021, relative to 2019. The impact of Covid-19 pandemic is evident, but a relevant increase is expected due to the economy recovery. Interactive graph available at [2].

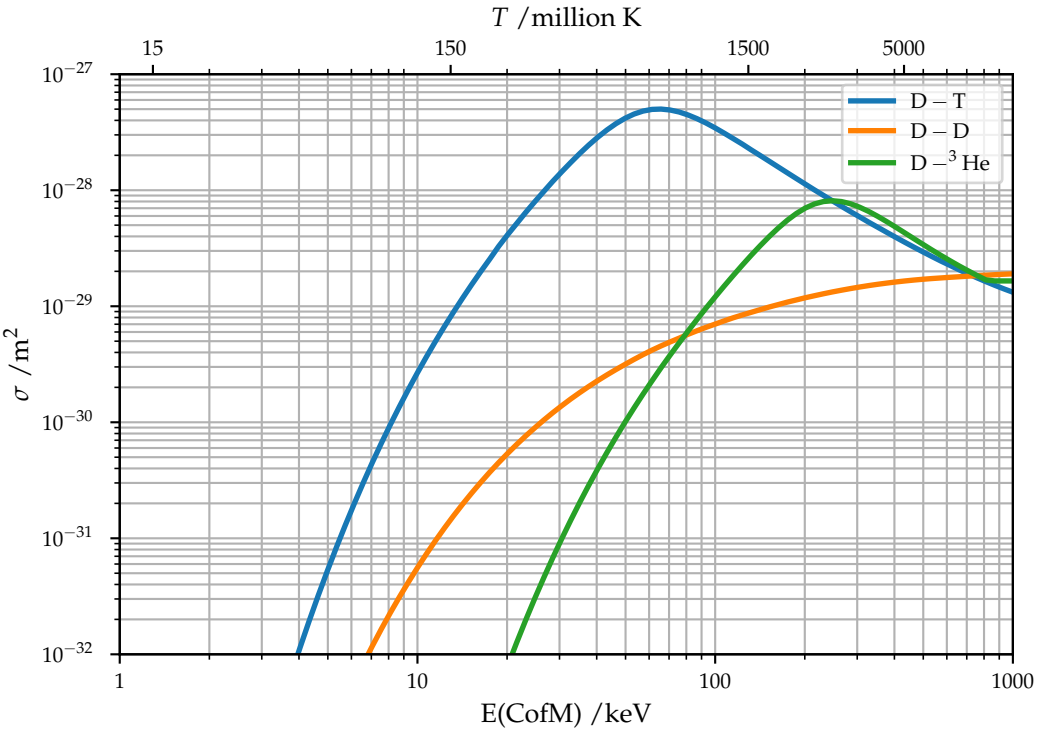

Figure 1.3: Cross sections of the main fusion reactions, as a function of both the Centre of Mass energy [keV] and the temperature T [10^6K]. Data fetched from [3].

However, while fusion processes happen naturally in the stars, on Earth nuclear fusion is quite an unlikely process, limited by the high temperature and pressure required for overcoming the Coulomb repulsion. The probability for a fusion reaction to occur depends on the cross-section σ, which is dependent on the particle energy as shown in Figure 1.3. As can be seen, the reaction with the highest cross section at the lowest temperature is the one involving deuterium and tritium (1.3).

Both these hydrogen isotopes are present abundantly or can be produced on Earth. In particular, Deuterium has an abundance of 0.015% in the ocean's water, therefore it can be considered practically infinite with respect to the needs for the future fusion reactors. Tritium, on the other hand, is more rare, but can be obtained by using lithium and the neutrons produced by the fusion reactions themselves:

$$n + {}^6Li \Rightarrow {}^4He(2.1\,\mathrm{MeV}) + {}^3T(2.7\,\mathrm{MeV})$$

and thus the boundaries are set by lithium availability, which is not a pressing issue at present [4].

All this considered, the research on fusion, even if long and difficult, will give humankind access to an essentially limitless source of energy.

1.2. The ITER project

In this framework, the biggest international collaboration is ITER: an experiment whose aim is to create the first nuclear fusion reactor, suitable for energy production. The ITER project is the result of an agreement signed in 2006 by China, the European Union, India, Japan, Korea, Russia and the United States, and at the moment several test facilities are contributing to the development of each part of the future nuclear fusion reactor. For example, PRIMA (Padova Research on ITER Megavolt Accelerator) is hosted in Padua, testbed for both the full-scale prototype of ITER Heating Neutral Beam (HNB) injector (SPIDER) and the full-size radio frequency negative-ions source (MITICA) [5].

ITER will be the world's largest *tokamak*, a toroidal fusion device based on plasma magnetic confinement. Inside its vacuum chamber, the fusion conditions of extreme heat and pressure are reproduced, and gaseous hydrogen fuel becomes a plasma, hence creating the proper environment for fusion energy production. To achieve this goal, ITER is designed with the parameters reported in Table 1.1: these characteristics will allow ITER to become the first fusion device to effectively produce net energy.

Parameter	Value
Fusion power	500 MW
Power gain factor Q	10
Plasma major radius	6.2 m
Plasma minor radius	2.0 m
Plasma current	15 MA
Toroidal field at 6.2 m radius	5.3 T

Table 1.1: Some of ITER design parameters. [6]

Unfortunately, this is a challenging task, and while the final goal is constantly approached, several parameters still have to match the necessary requirements. To reach this objective, other facilities in the world are studying the various aspects and problems concerning fusion, with the same final aim.

1.3. Neutral Beam Injection

One of the most challenging tasks concerns plasma heating. In fact, to reach the ignition conditions and the required power gain factor, ITER needs to rely not only on ohmic heating, but also on two additional systems: radiofrequency heating, thanks to which plasma is heated externally through electromagnetic radiation, and Neutral Beam Injection (NBI).

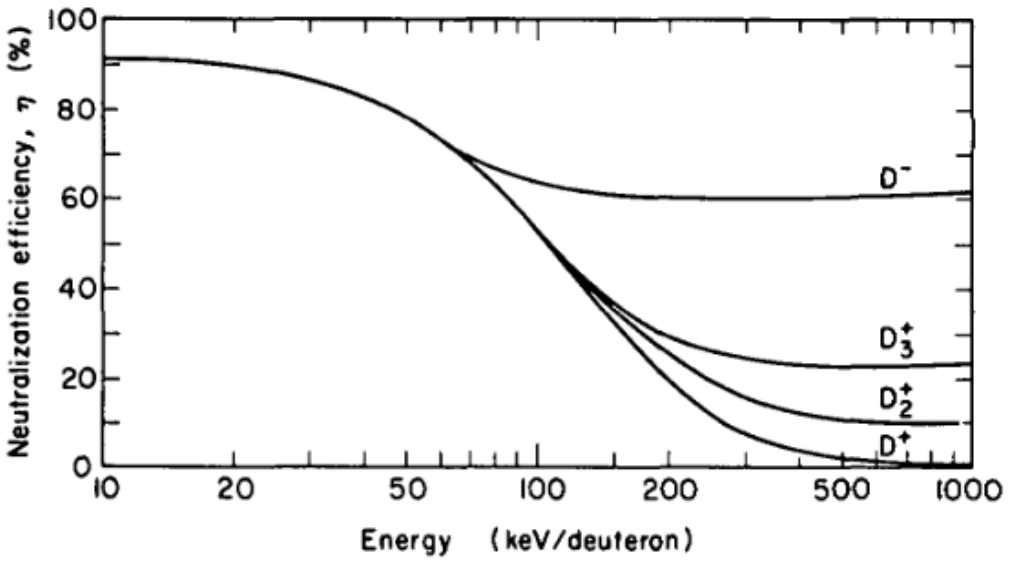

Figure 1.4: Maximum neutralisation efficiency of a fast D ion beam in a gas cell, as a function of the ion energy.[7]

NBI consists of a beam of highly-energetic neutral particles that, inserted in the plasma chamber, convey heat to the plasma, by transferring their kinetic energy through collisions with the plasma after their ionization. However, neutrals cannot be easily accelerated to the high energies required by simply applying a potential difference, given their absence of charge: therefore, the energetic neutral beam is generated by neutralising a precursor ion beam, properly accelerated.

Positive ion beams are generally more easily manageable: since they carry a positive charge, there is no risk of simultaneously extracting and accelerating plasma electrons, which can cause structural damage to the beamline components if fully accelerated with the rest of the ions, and can lead to worse performances in terms of energy efficiency.

However, as shown in Figure 1.4, at the high energies required for the ITER project ($\approx$ 1 MeV), it is very difficult to obtain a neutral beam that is sufficiently energetic from positive ions. Negative ions, on the other hand, feature a much higher neutralisation efficiency, given that the bond energy of the additional electron is only 0.75 eV and they have a very large cross-section for electron detachment in this energy range.

Therefore, ITER NBI will be generated by a negative ion beam, which will be produced by a negative ion source with the following parameters (Table 1.2):

	Unit	H	D
Beam energy	keV	870	1000
Current density of ions extracted from the plasma	Am^{-2}	329	286
Beam-on time	s	1000	3600
Max beam source filling pressure	Pa	0.3	0.3
Max deviation from uniformity	%	± 10	± 10
Beamlet core divergence	mrad	≤ 7	≤ 7
Beamlet halo divergence	mrad	≤ 30	≤ 30
Core/halo fraction		85/15	85/15
Co-extracted electron fraction $(e-/H-)$ and $(e-/D-)$		< 0.5	< 1
Horizontal beamlet misalignment	mrad	± 2	± 2
Vertical beamlet misalignment	mrad	± 4	± 4

Table 1.2: Design parameters for ITER NNBI system [8], [9].

1.4. BATMAN-Upgrade

BATMAN (BAvarian Test MAchine for Negative ions) [10] is one of the first negative-ion Radio Frequency (RF) sources developed for neutral beam injectors, active since 1996 in IPP-Garching (Munich) and one of the oldest test facilities related to ITER. The experiment has been constantly improved over the years, but especially in 2018 it was significantly upgraded, among others with a new extraction system, making it closer to the ITER source design [11].

The machine was provided with a new grid system, composed of 3 grids (Plasma Grid, Extraction Grid, Grounded Grid) with 5×14 apertures each, representing approximately one ITER beamlet group, which is instead composed of 1280 apertures divided into 16 beamlet groups (Figure 1.5). The new grid system also plays a relevant role in the magnetic Filter Field (FF) formation: before the upgrade, the magnetic filter field was only generated by permanent magnets placed at the lateral walls of the source, while now it can be additionally produced by a vertical current I_{PG} flowing through the plasma grid, reducing the co-extracted electron density and cooling them down in the region close to the PG, but causing a vertical deflection of the beam.

Furthermore, to avoid accelerating wastefully the co-extracted electrons to full beam energy, the EG is provided with some embedded magnets (Co-extracted Electron Suppression Magnets), that deflect the electrons onto the grid. However, the CESM cause an unwanted row-wise deflection of the beamlets, the so-called **zig-zag deflection**, which should be corrected in order to satisfy the beamlet misalignment ITER requirements (± 2 mrad horizontally, ± 4 mrad vertically [9]). As a consequence, in 2021 the additional Asymmetric Deflection Compensation Magnets (ADCM) have

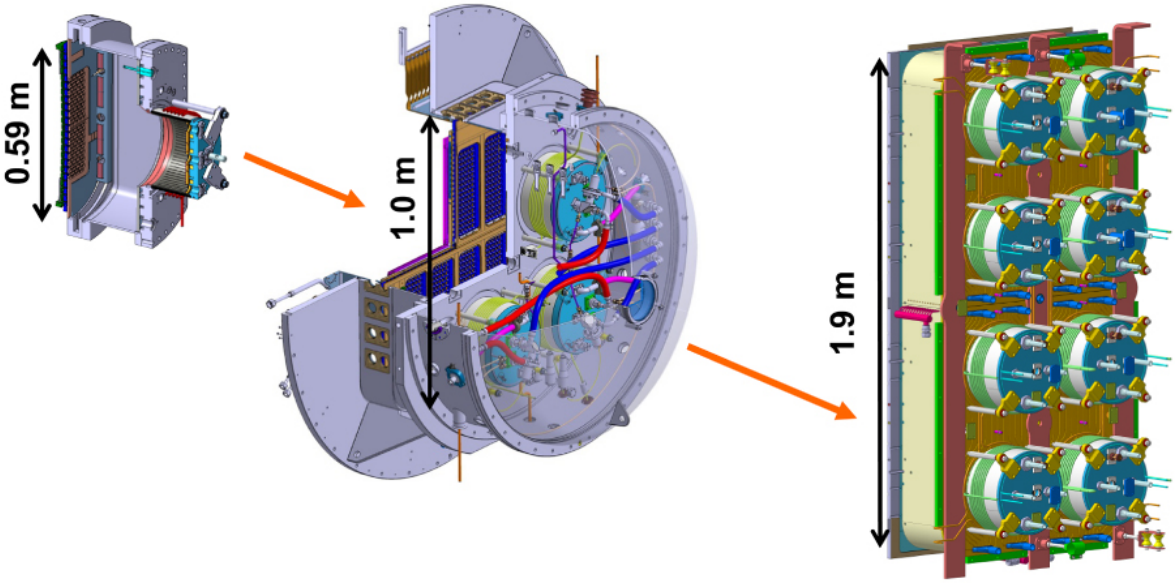

Figure 1.5: Size scaling from BATMAN (left) to the ion source of the ELISE test facility (centre), to the full negative ion source for ITER NBI (SPIDER, right). [12]

been installed on BUG-MLE on the top-half of the EG, which correct the beamlet angles by strengthening the field upstream of the grid. The experimental apparatus will be described in more detail in chapter 3.

1.5. Aim and layout of the thesis

This work intends to pursue two main objectives: to study the zig-zag deflection problem and to evaluate the robustness of the compensation performed by the ADCMs. For achieving these tasks, a comparison between theoretical, computational and experimental aspects is included in this dissertation in order to have a complete overview of the topics treated.

More specifically, chapter 2 provides the description of the main physical phenomena related to negative ion sources, especially focusing in the negative ions formation and extraction (section 2.1). In section 2.2, instead, the theory behind the diagnostics employed (BES in section 2.2.1, CFC in section 2.2.2) is presented. Chapter 3 describes the experimental apparatus of BUG-MLE (section 3.1) and the technical details about the BES and CFC are provided in 3.2.

Following, in chapter 4 the computational work is displayed. Firstly the main software exploited is described in section 4.1, then the general simulation routine is defined (section 4.2). The main results obtained are reported in section 4.3 for the CFC and in 4.4 for the BES. The next chapter includes the analysis of the data collected during the experimental campaign. More in detail, section 5.1 presents an overview of the data taking sessions, while section 5.2 contains the obtained results, for both the CFC (section 5.2.1) and the BES (section 5.2.2). Finally, conclusions are drawn in chapter 6.

Even though we should learn from those who came before us, we must also forge our own path.

Avatar Korra

2

Theoretical overview

To thoroughly understand how to approach the zig-zag deflection issue, it is important to understand how negative ion sources, precursors of the neutral beam, work, focusing in particular on the main physical processes involved in negative ion production and in beam extraction.

In this chapter, at first some details about the general structure of negative ion sources are displayed in section 2.1, in which first the production processes and the first stages of beam formation are displayed in 2.1.1 and following, the principal beam extraction phenomena are described in 2.1.2.

Finally, a presentation of the main functioning of the two diagnostic systems adopted in this thesis, namely the Beam Emission Spectroscopy and the Carbon Fiber Composite Calorimetry, can be found in 2.2.

2.1. Negative ion sources

As already introduced in chapter 1, to obtain a neutral beam able to heat the plasma at the high energies required for ITER project, the precursor beam must be composed of negative ions. The classical structure of a negative ion source is represented in the scheme in Figure 2.1. In the following paragraphs, the main functioning will be described, along with the principal issues and physical phenomena occurring during beam formation.

2.1.1. The driver and the expansion region

The **driver** is constituted by an alumina cylinder and is the region in which the plasma is first generated, by providing energy through the RF coils around it.

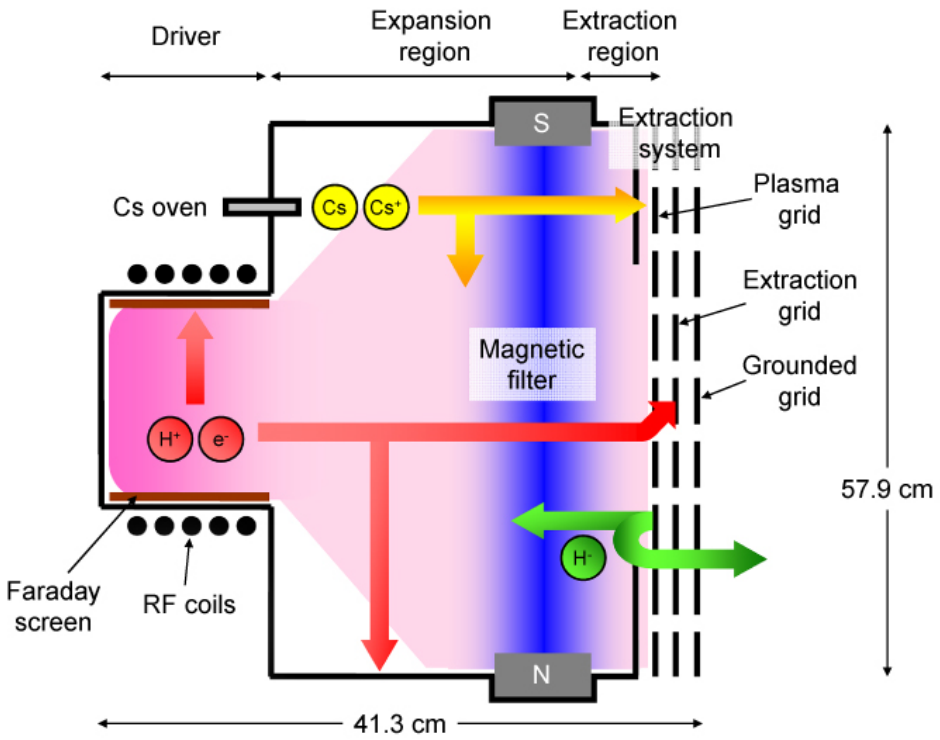

Figure 2.1: Schematic view of the IPP prototype negative hydrogen ion source.[12]

In order to protect the ceramic walls of the drivers from the plasma influence, a Faraday screen is added inside the cylinder. This also makes the coupling between the radio-frequency and the plasma purely inductive: thus, calibrating properly the matching frequency becomes a crucial step in the design of a source.

The driver is directly followed by the **expansion region**, in which the plasma can diffuse and the electron temperature can cool down. In this volume, the electron temperature T_e usually decreases strongly also due to the presence of a magnetic field parallel to the plasma grid of approximately one order of magnitude (from $\approx 10\,\text{eV}$ to $\approx 2\,\text{eV}$).

This 2-stage structure is needed for guaranteeing the best condition for the so-called **volume production** of negative ions [13]. Low electron temperatures are required for one of the main processes that ensures the formation of negative hydrogen ions, namely the "dissociative electron attachment", in which highly rovibrationally excited molecules of H_2 (or D_2) collide with an electron. However, since more energetic electrons are necessary to create the highly vibrationally excited molecules, the production process is divided into two phases (in the drivers and in the expansion region) that allows the decrease of T_e towards the PG.

Nonetheless, volume production alone is not sufficient for producing the flux of negative ions needed for ITER NBI, as a consequence, also **surface production** must be considered and enhanced. In this process, negative ions are produced by the interactions between the plasma and a metal surface, more specifically the main area in which surface production is important is the Plasma Grid (PG). This grid is

the boundary between the expansion region and the acceleration stage, and allows plasma particles that impinge on it to collect the extra electron required for ionisation.

To enhance this reaction, the PG is covered with a layer of caesium, which lowers the surface work function enough to increase the probability of surface production. The deposition of the Cs layer is performed via a Cs oven that vaporises Cs inside the source. Homogeneous Cs deposition is ensured by monitoring the source temperature and by heating the PG [14].

The negative ions created by the surface process are backscattered towards the expansion region, but, near the PG apertures, they are attracted by the electric field on the other side of the PG. In addition, this grid is provided with a magnetic field parallel to its plane (the already mentioned FF, $\approx 1 - 10\text{mT}$), that is used to lower even more the electron temperature. Moreover, it reduces the velocity of the electrons orthogonal to the PG, and also actively decreases the electron detachment process which destroys negative ions.

Another important aspect to consider is the amount of co-extracted electrons. These particles are naturally present in the plasma and can be generated in many ways. They are problematic because they could compromise the energetic efficiency and the safety of the NBI, by increasing the thermal load on the beamline components while actually not contributing to carrying power for the beam. The aforementioned filter field helps also in keeping the ratio of co-extracted electrons and negative ions low, by deflecting the lighter particles more than the ions due to their mass difference.

In addition to the FF, a commonly adopted technique to reduce the amount of co-extracted electrons consists in biasing the PG positively against the source body: to do this, a bias plate (BP) is installed next to the PG, connected to the source walls and covers the external borders of the extraction area.

The bias and the filter field magnitude need to be properly adjusted in order to minimise plasma drifts, which could cause beam inhomogeneities, while reducing the number of high energy electrons, which could destroy the negative ions [15].

The extra electron of the negative H^-/D^- ions is only weakly bound (0.75 eV). This is beneficial for the neutralisation, but also leads to unwanted **stripping losses**, where the ion loses its electron inside the grid system due to the collisions with the background gas, and is therefore not fully accelerated. Most stripping losses occur between the PG and EG, due to the higher cross section (see Figure 1.4). To limit the stripping losses, the pressure inside the grid system must be kept as low as possible, which is why the filling pressure is present in ITER requirements' table 1.2.

2.1.2. Beam extraction and acceleration

After the drivers and the expansion region, the next area is the **extraction region**. Here, the ions are drawn through the apertures of the PG by an electric field, created by the potential difference between the PG and the Extraction Grid (EG), and are

further accelerated by the potential difference between the EG and the Grounded Grid (GG)[1].

The grid voltages are held at specific potentials relative to the GG, and the extraction and acceleration voltages are defined relatively between the grids as follows:

$$U_{ext} = U_{EG} - U_{PG}; \tag{2.1}$$

$$U_{acc} = U_{GG} - U_{EG} = -U_{EG}. \tag{2.2}$$

Depending on U_{ext}, U_{acc}, two other important quantities to be defined are:

$$U_{tot} = U_{ext} + U_{acc}; \tag{2.3}$$

$$U_{ratio} = \frac{U_{acc}}{U_{ext}}. \tag{2.4}$$

that are respectively the total voltage applied between the PG and the GG and the ratio between acceleration an extraction voltage.

Due to the electric field induced by the potential differences, the ions form several **beamlets**, namely small beams centred in each PG aperture, which are then accelerated. The main issue in this delicate stage is the co-extracted electrons, which, despite the filter field, might be nevertheless present in the beamlets. To reduce their impact and to prevent them from being wastefully accelerated, the EG is provided with an arrangement of permanent magnets embedded around its apertures (Co-extracted Electrons Suppression Magnets, CESM): in this way, the electrons are deflected and are dumped on the EG instead of remaining in the beamlets, given their significantly lower mass compared to the ions ($m_{H^-}/m_e \approx 1836$).

However, the ions are not unaffected by the action of the CESM. The magnetic field generated is perpendicular to the filter field (so it is vertical) and thus will result in a horizontal row-wise alternate deflection of the beamlets named **zig-zag deflection**[2]. An example can be seen in the bottom half of the grid represented in Figure 2.2: one can clearly notice that the beamlet footprints are shifted leftward/rightward due to the action of the CESM.

To counter this effect, a new improvement to the EG is added for this experimental campaign: in the top half of the grid some other permanent magnets are installed, the Asymmetric Deflection Compensation Magnets (ADCM). Their goal is to compensate for the zig-zag deflection by adding a new magnetic field component that makes the vertical field B_z asymmetric in the extraction region, as reported in Figure 2.3.

[1] In some cases, more than 3 grids are present, for example, the older version of BUG had 4 grids, with the Repeller Grid, positioned between the EG and the GG.[11]

[2] The CESM-induced field could also be horizontal and the zig-zag deflection vertical, depending on magnets orientation.

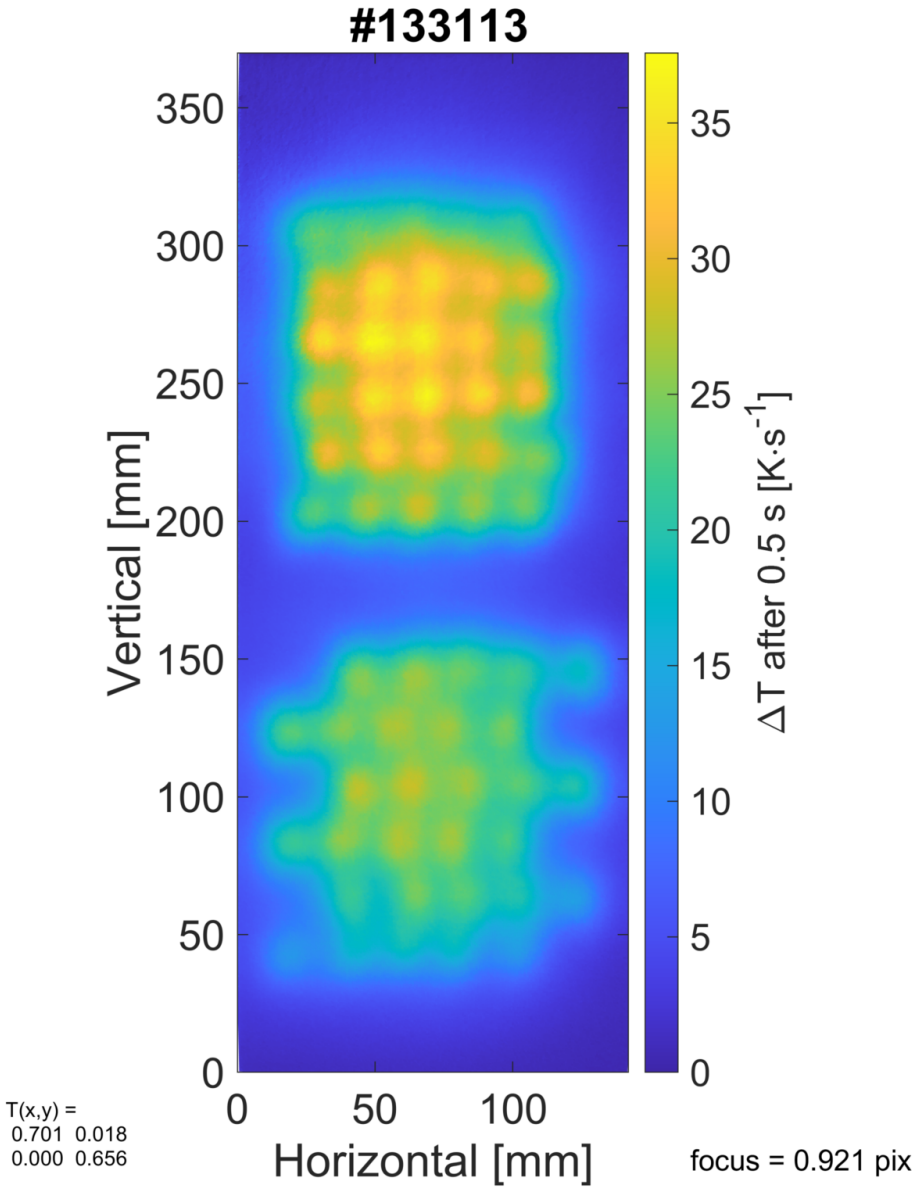

Figure 2.2: Processed images from the CFC tile. The shot parameters are $I_{PG} = 1.5\,\mathrm{kA}$, $U_{ext} = 5\,\mathrm{kV}$, $U_{acc} = 32.5\,\mathrm{kV}$, $p_{fill} = 0.6\,\mathrm{Pa}$, $P_{RF} = 70\,\mathrm{kW}$.

In fact, the beamlet deviation angle at the end of the grid system depends on the ratio of the magnetic field upstream and downstream of the extraction grid, which is different from zero since the magnetic field is shielded in the plasma [16]. Adding the ADCMs strengthen the upstream magnetic field and weaken the downstream field and hence impacts on the deflection, as it can be seen from the upper part of Figure 2.2, in which the zig-zag deflection is compensated by the ADCMs. The technical details about the ADCMs are presented in chapter 3.

It is clear that the design of the aperture and the positioning of the grids are critical aspects to be considered. Additionally, changes in the trajectory due to mutual beamlet repulsion and the deviations induced by the magnetic field (vertical

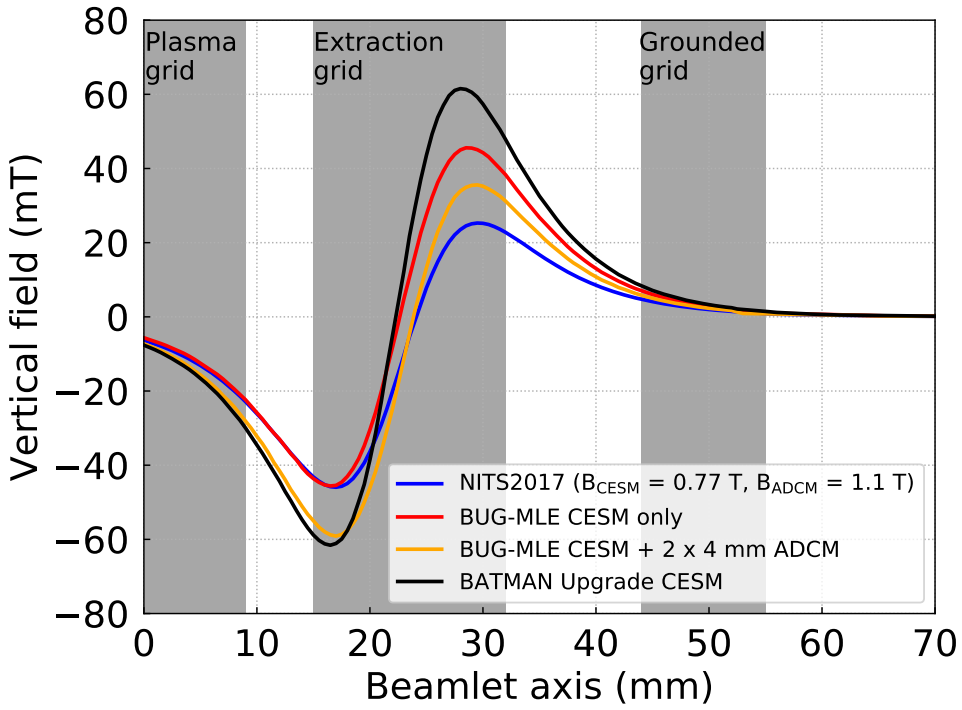

Figure 2.3: Comparison of the vertical magnetic field component for BUG, BUG-MLE without ADCMs, BUG-MLE with ADCMs and the QST experimental campaign [17].

deflection from the FF, zig-zag deflection, ADCMs compensation) needs to be taken into account. Thus, the grids and their apertures must be properly placed in order to avoid further losses and damages to the apparatus.

Given the action of the CESM, the EG must be properly cooled since it is constantly hit by electrons. The maximum acceptable power load on the EG sets two important upper limits: on the extracted ion current and on the extraction potential $U_{ext} \leq 10\,\text{kV}$, both for limiting the amount of electrons and hence the damages to the EG.

Moreover, the EG potential determines the first step of the acceleration process: the voltages set, the geometry of the grid system (aperture shapes, distance between them) and the current carried by the beamlets constitute the electrostatic **lens** effect, which influences the trajectories of the ions.

In particular, the profile of the electric field, especially in the region between the PG and the EG, define the so-called **meniscus**, i.e. the equipotential surface through which ions are extracted from the plasma. Its concavity depends on the extraction voltage U_{ext}, the size of the apertures and the plasma parameters [18]. The shape of the meniscus determines the position of the beamlet focal point, as can be seen in the 3 pictures in Figure 2.4.

If the meniscus is too concave, the focal point usually is too close to the PG, therefore the resulting beamlet will tend to diverge beyond the focus and the extracted current density is particularly low (Figure 2.4.(a)). The beamlet diverges also if the

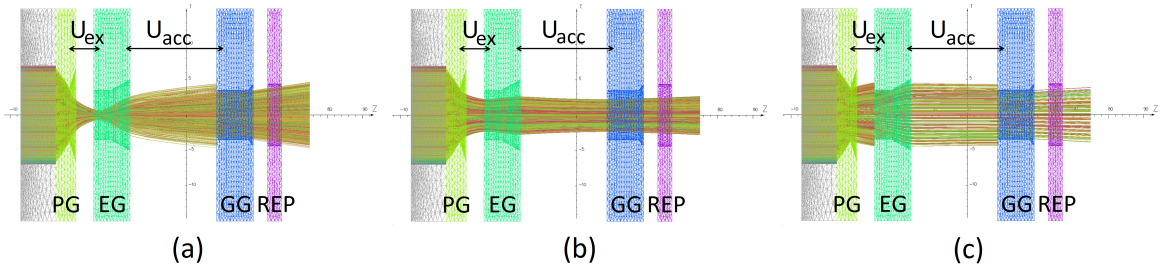

Figure 2.4: Simulation of beam acceleration for the NIO1 ion source by the code OPERA [19], $U_{ex} = 5\text{kV}, U_{acc} = 45\text{kV}$. Z axis is compressed by a factor 2. (a) $J_{ext} = 10\text{A m}^{-2}$, $P = 4 \cdot 10^{-10}\text{A/m}^{3/2}$; (b) $J_{ext} = 30\text{A m}^{-2}$, $P = 1.2 \cdot 10^{-9}$ A/V$^{3/2}$; (c) $J_{ext} = 100\text{A m}^{-2}, P = 4 \cdot 10^{-9}\text{A/m}^{3/2}$.

meniscus is too flat: in this case, even if the extracted current and the plasma density are high, the beamlet will be improperly focused by the action of the lens (Figure 2.4.(c)). An optimum condition can be found between the two [20] (Figure 2.4.(b)): the beamlet will be well focused and not spread in space, transporting the beam energy up to the end of the accelerator and limiting damages to the beamline components.

In summary, the shape of the meniscus and all the main source parameters (source pressure p_{fill}, RF power P_{RF}, extraction voltage U_{ext}) have an impact on the amount of extracted ions and hence a direct influence on the extracted current density, which can be modelled with the **Child-Langmuir** law (2.5) [20]:

$$J_{ext} = \frac{4}{9}\epsilon_0 \sqrt{\frac{2Ze}{m}} \frac{U_{ext}^{3/2}}{d^2} \tag{2.5}$$

Eq. (2.5) allows computing the maximum current density of an ion with mass m and charge Ze when a voltage U_{ext} is applied between two electrodes at distance d. Child-Langmuir law also states that lighter ions can provide the most current density, given the dependence on $\propto m^{-1/2}$.

The most important dependence is, though, on the extraction voltage: if U_{ext} is too small, the extracted current will not reach high values, despite increasing the RF power given from the source. At the same time, U_{ext} cannot be increased at will, as previously mentioned, because there is nevertheless a limit set by the source pressure and the power supplied.

To link the extracted current and the beam optics determined by PG and EG, a very important beam(let) parameter is defined, the **perveance** P:

$$P = \frac{I_{ext}}{U_{ext}^{3/2}} \tag{2.6}$$

where I_{ext} is the extracted current, equal to the product of J_{ext} multiplied by the correspondent area. To compare the values of P between different machines, the perveance is often normalised with respect to its value P_0 given by the Child-Langmuir law and the extraction area, when the flow of the beam particles is limited

only by their space charge:

$$P_0 = \frac{4}{9}\pi\epsilon_0\sqrt{\frac{2Ze}{m}}\left(\frac{R}{d_{\text{grids}}}\right)^2 \tag{2.7}$$

in which R is the radius of the grid apertures.

The normalised perveance P/P_0 is particularly important in the context of evaluating the beam quality, because it is related to the **beam(let) divergence**. The divergence is a parameter that quantifies how divergent, i.e. spread in space, is a beamlet and it can be calculated as the angle between the beamlet axis and locations where the power density is reduced a factor $1/e$ with respect to the on-axis value, according to (2.8):

$$\text{Divergence} = \theta_{1/e} = \sqrt{2 \cdot \frac{\sum_{i=1}^{N}\left(y'_i - y'_{avg}\right)^2}{N}} \tag{2.8}$$

where y'_i is the horizontal position of the $i-$th particle and y'_{avg} is the average horizontal particle position of a beamlet with N particles. Monitoring the beamlets' divergence is crucial: a beamlet with low divergence helps in keeping the thermal load on the beamline components within the safety levels and hence ensure the durability of the experiment. The normalised perveance P/P_0 can be used in this context as a similarity parameter between different systems, helping to distinguish whether the beam is well focused or not. Observing Figure 2.4 with this in mind, one can notice that 3 regimes are present:

- an optimum divergence regime (Figure 2.4.(b)), in which the beam has minimum divergence associated to a certain value of P/P_0;
- an under-perveant regime, with normalised perveance lower than the optimum one (Figure 2.4.(a));
- an over-perveant regime (Figure 2.4.(c)), in which the value of P/P_0 is higher than the optimal one.

Thus, after assessing the normalised perveance, choosing properly the extraction potential is fundamental for keeping the beamlet divergence under the limits, because the goal of a NBI is to inject the beam particles into a fusion reactor and to this purpose having a well-focused, precisely aimed beam of accelerated particles is essential.

To obtain conditions of optimum beamlet divergence, it is also critical to study thoroughly the aperture shape. The principal aim is to minimize the so-called **halo**, i.e. an external layer with higher divergence located around the more focused central beamlet **core**. The halo is generated by many different physical processes, namely optic aberrations at the grids, caesium deposition on the downstream face of the

apertures of the PG, in addition to the aperture geometry and the meniscus shape [21].

The main issue with the halo is that the ions extracted from this area might be intercepted by the grids and some additional heat might be deposited on their surfaces, leading to significant power losses that can result in not having enough neutrals to be injected into the tokamak.

2.2. Diagnostic systems

Analysing the beam profile in fusion experiments is a difficult yet crucial step. In particular, for neutral beams employed for plasma heating, using material targets is challenging due to the high power density of the accelerated beams. Therefore, other techniques are developed, such as Beam Emission Spectroscopy (BES).

BES is a simple and reliable tool based on the Doppler effect ([22], [23]). It requires no absolute intensity calibration, it is non-invasive and the presence of magnetic fields or high potentials does not disturb the acquired spectra. Thanks to BES, it is possible to measure the beam divergence, needed to monitor the safety of the beamline components, and the beam uniformity, which defines the quality of the produced beam itself. The main physics behind BES is displayed in section 2.2.1.

The other diagnostic adopted in BUG-MLE is a Carbon Fibre Composite (CFC) calorimeter, presented in 2.2.2, which is a retractable tile [24] that allows the detection of the beamlet footprints via infrared thermography.

2.2.1. Beam Emission Spectroscopy and the Doppler effect

The Doppler shift $\Delta\lambda$ of a spectral line λ_0 emitted by a beam particle at a viewing angle θ (see Figure 2.5) with respect to the beam velocity $\beta = \frac{v}{c}$ is:

$$\Delta\lambda = -\lambda_0(\gamma(1 + \beta\cos\theta) - 1), \tag{2.9}$$

with $\gamma = \frac{1}{\sqrt{1-\beta^2}}$ the relativistic Lorentz factor. In an non-relativistic approximation, $\gamma \approx 1$ and hence it holds:

$$\Delta\lambda = -\lambda_0\beta\cos\theta. \tag{2.10}$$

When computing the beam divergence, one of the possible approaches is to consider only small variations around a central Doppler shift.

When considering an experimental setting, reported in Figure 2.5, usually line broadening is a consequence of both a distribution of θ and a distribution of the beam energies, therefore, both these factors need to be taken into account.

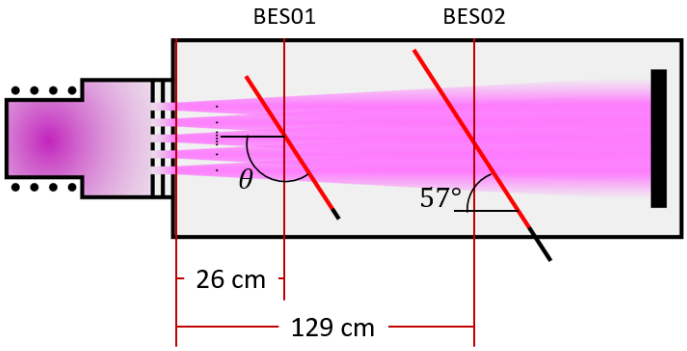

Figure 2.5: Scheme of the experimental setting, with θ pointed out. More details can be found in chapter 3.

Generally, the wavelength variation of an average beam with velocity v_0 that follows a trajectory with viewing angle θ_0 will be:

$$\Delta\lambda_0 = -\lambda_0 \frac{v_0}{c} \cos\theta_0, \tag{2.11}$$

and as a consequence, its variation can be computed by considering the differentials $\mathrm{d}v_{\parallel}$ and $\mathrm{d}v_{\perp} = v_0\,\mathrm{d}\theta$, leading to:

$$\delta \equiv \mathrm{d}(\Delta\lambda) = \Delta\lambda_0 \left(\frac{\mathrm{d}v_{\parallel}}{v_0} + \tan\theta_0\,\mathrm{d}\theta \right). \tag{2.12}$$

as reported in [25]. This quantity can be used as a base to compute the divergence of the beam. Assuming a Maxwell-Boltzmann distribution for velocities:

$$f(v)\mathrm{d}v \propto \exp\left[-\frac{mv^2}{2T} \right] \mathrm{d}v, \tag{2.13}$$

the divergence is the $1/e$ half-width of the velocity distribution (2.13), and is linked to the temperature T with the following expression:

$$\epsilon = \sqrt{\frac{T}{E_{\mathrm{beam}}}}, \tag{2.14}$$

It is important to state that the assumption on the **Gaussian** distribution of velocities is a strong hypothesis, required to obtain a single evaluation of the divergence and hence to compare different experimental results and conditions. However, the direct consequence is a loss of generality, which limits the analysis.

Divergence ϵ (2.14) can be defined for both the parallel and the perpendicular component of v, induced respectively by parallel and perpendicular temperatures, $T_{\parallel}$ and $T_{\perp}$. Therefore, combining (2.14) and (2.12), the line broadening given by

perpendicular temperature $T_\perp$ is:

$$\delta_\perp = \epsilon_\perp \Delta\lambda_0 \tan\theta_0 = \sqrt{\frac{T_\perp}{E_{\text{beam}}}} \Delta\lambda_0 \tan\theta_0; \tag{2.15}$$

while the one derived from the parallel one is:

$$\delta_\parallel = \epsilon_\parallel \Delta\lambda_0 = \sqrt{\frac{T_\parallel}{E_{\text{beam}}}} \Delta\lambda_0 \tag{2.16}$$

Nevertheless, experimental evidence and simulations prove that the parallel temperature contribution (2.16) is less relevant with respect to the perpendicular one (2.15) on the divergence of the beam, and the two contributions cannot be distinguished with a single measurement, as proved by [25]. This is generally due to imperfections of the acceleration structures, and since the energy spread which cause the line broadening on the parallel component is usually compressed by the parallel acceleration, the contribution of $\epsilon_\parallel$ can be considered negligible.

Furthermore, it is worth noticing that the experimental conditions may be another source of line broadening, e.g.:

1. the aperture width of the light collecting system, which gives a contribution $\delta_{\text{coll}} = \epsilon_{\text{coll}} \Delta\lambda_0 \tan\theta_0$, with ϵ_{coll} a parameter given by the geometry of the system;
2. other effects due to the experimental conditions (i.e., the width of the slits of the spectrometer entrance and exits, the imperfections in the collimation process, the camera lens resolution), represented by the term δ_{instr}.

Combining all these effects, the total line width will be:

$$\delta = \sqrt{\delta_\perp^2 + \delta_{\text{instr}}^2 + \delta_{\text{coll}}^2}$$

and hence the total divergence can be estimated as:

$$\epsilon = \sqrt{\frac{\delta^2 - \delta_{\text{instr}}^2}{(\Delta\lambda_0 \tan\theta_0)^2} - \epsilon_{\text{coll}}^2}$$

BES spectrum analysis

For hydrogen or deuterium beams, the most commonly observed line emission is the H_α / D_α radiation ($\lambda_0 = 656.2793$nm for hydrogen, $\lambda_0 = 656.1032$nm for deuterium), since it is the most intense line in the visible spectrum. The H_α / D_α photons are produced by the de-excitation to the $n = 2$ level of H/D atoms, previously excited to the $n = 3$ level by the following reactions, where the neutrals and the positive ions of the beam are produced in the interaction of the beam itself with the background gas:

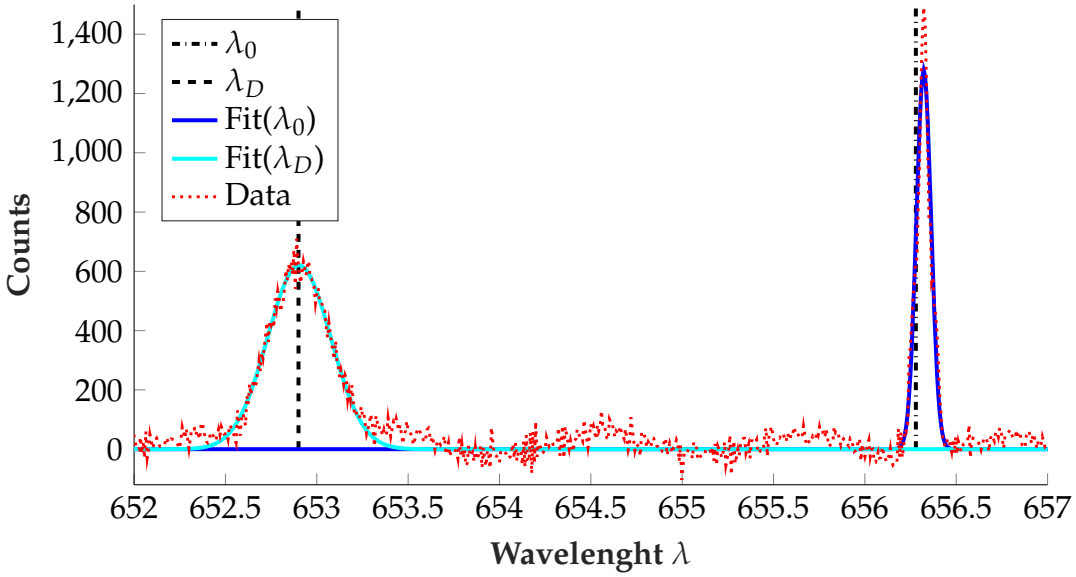

Figure 2.6: Experimental BES spectrum acquired by the detector BES02-02 mounted on BATMAN-Upgrade, with Gaussian fits of the two main peaks (corresponding to λ_0 and λ_D). Shot number 132812.

$$H^-_{beam} + H_2 \Longrightarrow H^*_{beam} + H_2 + e \tag{2.17}$$
$$H_{beam} + H_2 \Longrightarrow H^*_{beam} + H_2 \tag{2.18}$$
$$H^+_{beam} + H_2 \Longrightarrow H^*_{beam} + H^+_2 \tag{2.19}$$
$$H^-_{beam} + H_2 \Longrightarrow H_{beam} + H + H^* + e \tag{2.20}$$
$$H_{beam} + H_2 \Longrightarrow H_{beam} + H + H^* \tag{2.21}$$
$$H^+_{beam} + H_2 \Longrightarrow H^+_{beam} + H + H^* \tag{2.22}$$

Reactions (2.17), (2.18) and (2.19) lead to the excitation of the fast beam particles: the wavelength of the resulting photons is Doppler shifted according to equation (2.10) (or (2.9), if necessary). As a consequence, a general spectrum collected by a BES system will look like the one reported in Figure (2.6). In this spectrum, two peaks, corresponding to the unshifted wavelength λ_0 and the Doppler-shifted one λ_D can be clearly observed, and are fitted with Gaussian functions to estimate their position and width.

The analysis of the collected spectra can help to infer several pieces of information on the beam, in particular on the beam divergence and on the beam direction.

The former, as already introduced in 2.1.2, is the width of the angular distribution of the beam particles trajectories around their main direction given by θ (eq. (2.8)). Through formula (2.10) fluctuations of θ are translated in fluctuations of wavelength, which are globally observed as a broadening of the main Doppler shifted peak, as described in the previous section.

The latter can be computed in terms of the angle θ between the beam itself and the direction along which the H_α / D_α photons are collected, assuming that the difference between the expected Doppler shift and the measured one is only due to different horizontal deflection. Let θ be the observation angle, $\langle\beta\rangle$ the expected particle velocity relative to c, $\langle\gamma\rangle$ the expected Lorentz factor, α the extra deflection. According to eq. (2.9), the expected Doppler shift $\langle\Delta\lambda\rangle$ is:

$$\langle\Delta\lambda\rangle = \lambda_0\langle\gamma\rangle(1 + \langle\beta\rangle\cos\theta)$$

While the measured one will depend also on the extra deflection α:

$$\Delta\lambda_{\text{meas}} = \lambda_0\langle\gamma\rangle(1 + \langle\beta\rangle\cos(\theta + \alpha))$$

Therefore the relative difference, normalised to the unshifted length λ_0 is:

$$\frac{\langle\Delta\lambda\rangle}{\lambda_0} - \frac{\Delta\lambda_{\text{meas}}}{\lambda_0} = \langle\gamma\rangle(1 + \langle\beta\rangle\cos\theta) - \langle\gamma\rangle(1 + \langle\beta\rangle\cos(\theta + \alpha))$$

which leads to:

$$\alpha = \cos^{-1}\left(\cos\theta - \frac{\langle\Delta\lambda\rangle - \Delta\lambda_{\text{meas}}}{\langle\gamma\rangle\langle\beta\rangle\lambda_0}\right) - \theta. \tag{2.23}$$

However, this method is limited by the difficulty of defining exactly the viewing angle θ: in fact, the angle is subject to several systematic errors and hence it is only reasonable to compute **relative** α measurements.

2.2.2. CFC Calorimetry

A CFC calorimeter is a well-known beam diagnostic [26] that relies on infrared thermography: the process of using a thermal imager to detect radiation (heat) coming from an object, converting it to temperature and displaying an image of the temperature distribution.

On BUG-MLE [24], the images collected are the thermal footprints of the beamlets that impact on the tile. Of course, they hit on the front of the CFC, depositing power on this surface. However, the footprint of the beam is viewed from the backside of the tile through an external infrared (IR) camera, installed on the side of the vacuum tank.

Despite this, the acquired images are a close representation of the heat flux of the beam, since the CFC material consists of a stacked arrangement of carbon fibres oriented in the same direction (in the target thickness): the heat conduction along the fibres is up to 20 times higher than perpendicularly to them, making the rear pictures a good representation of the front one.

The thermal images of the beamlet footprints permit the reconstruction of the beam shape, and through the proper perspective corrections, full grid images similar to Figure 2.2 are obtained.

In this figure, the single beamlets can be clearly identified, as well as the correction of the zig-zag deflection performed by the ADCMs installed in the top half of the grid. More details about the experimental analysis are included in chapter 5.

Nevertheless, this diagnostic is not free from systematic errors, which can be due to the camera (electronic noise, perspective correction, focus) or to the tile itself, such as inhomogeneities in the heat transfer, perpendicular heat conduction.

Besides, the tile has a limited thermal load that can sustain. In fact, despite the implicit high temperature resistance of the 1D-CFC material of the target, if it overcomes its operational limit of maximum allowable tensile stress, the carbon matrix in between the carbon fibres might crack [27]. Therefore, the beam-on time cannot be too long, in order to avoid excessive heat load on the CFC.

To realise longer beam pulses, the tile is retractable and can be removed from the path of the beam, so that it is not overheated.

It is through science that we prove, but through intuition that we discover.

Henri Poincaré

3

BATMAN Upgrade - MITICA-like Extraction

BATMAN-Upgrade (BUG) is approximately 1/8 of an ITER ion source, as already stated in chapter 1.4, and is provided with one RF driver. Its extraction and acceleration system is composed of 3 grids (PG, EG, GG) and the main operational parameters are reported in Table 3.1, while the core information about the technical details can be found in [11]. A scheme of the complete experimental apparatus is reported in Figure 3.1. As can be seen, BUG is composed of the ion source, the acceleration system and of several diagnostics, i.e. BES and two calorimeters.

Isotope	H, D
Extraction area	108 cm^2
Apertures	70, ∅14 mm
U_{tot}	$\leq$ 45kV
U_{ext}	$\leq$ 15kV
Total current	$\leq$ 15 A
RF power	150 kW, solid state gen.
Pulse length	10 s

Table 3.1: Main operational parameters of BUG. [11]

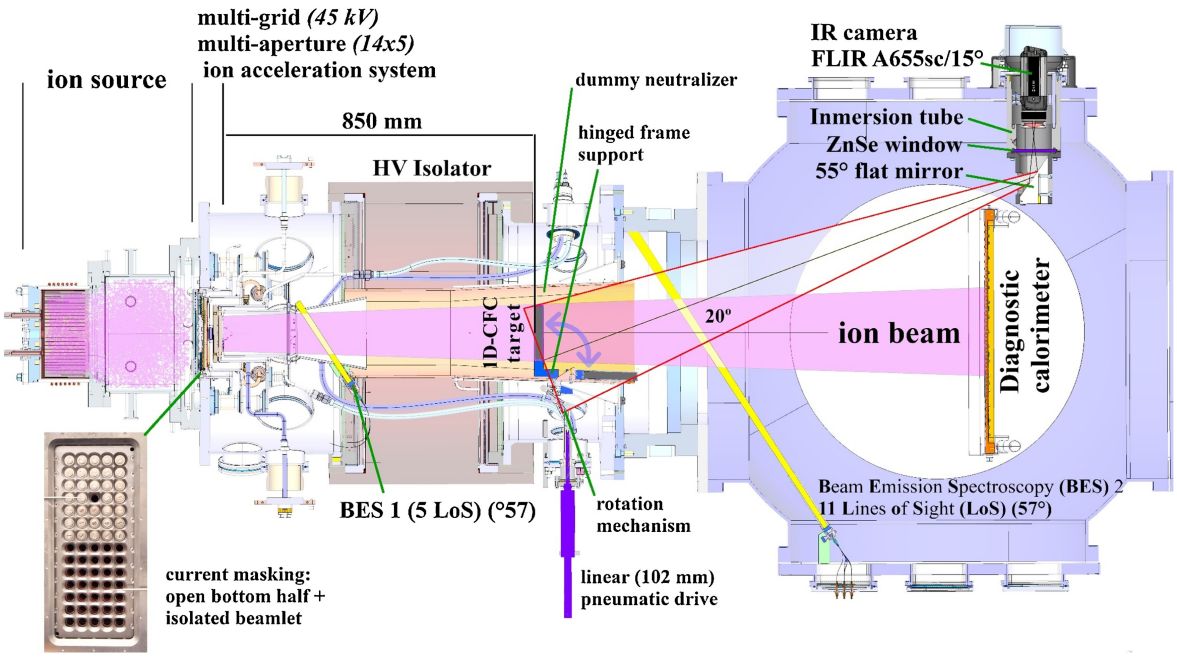

Figure 3.1: Horizontal cut-out view of the BUG, with its main components and beam diagnostic tools labelled [24].

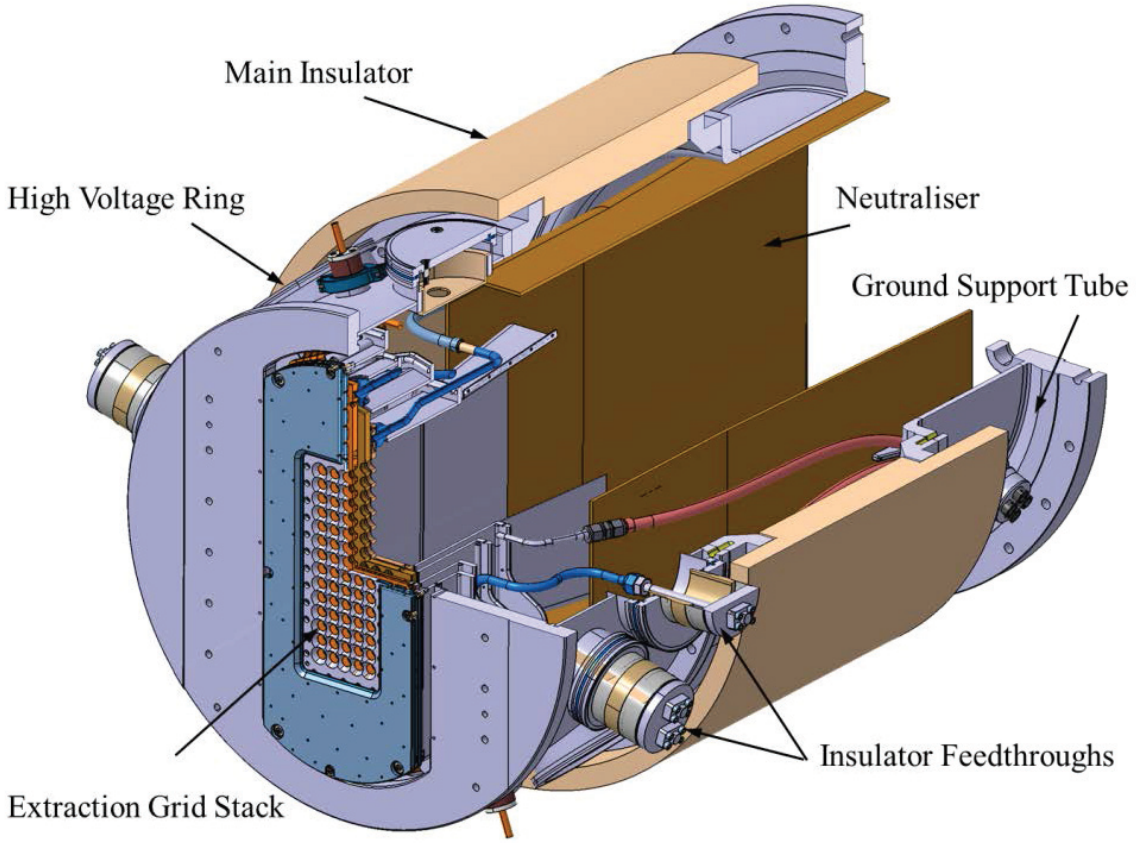

Figure 3.2: Extraction system of BUG [11].

The ion source is powered by a solid-state RF generator able to convey 150 kW of power. An alumina cylinder is mounted as the driver (plasma volume 8 L) on the back side of the source body (310 mm $\times$ 580 mm). The Faraday screen, made of copper and water-cooled, protects the driver from the plasma interaction. In order to reduce copper sputtering by the plasma, in particular self-sputtering of copper, this shield is additionally coated by a 3 µm molybdenum layer.

The extraction system is represented in Figure 3.2. It is provided with a ceramic main insulator (820 mm outer diameter, 555 mm length), which separates the high voltage potential of the source from the ground potential of the test facility.

On the source side, a high voltage ring forms an extension of the main insulator and allows radial access to the grid stack for all different water and current supplies on high potential thanks to the insulator feedthroughs, in the meantime providing mechanical support to the grid system itself.

In the following sections, the main aspects relevant to this thesis will be presented, more specifically section 3.1 describes some technical details about the grids, the permanent magnets embedded and the masking strategies, while in section 3.2 the diagnostic systems will be analysed.

3.1. The grid system

The BATMAN Upgrade with the ITER-HNB plasma grid and extraction grid will be referenced to as BUG MITICA-Like Extraction (BUG-MLE), as the experiment MITICA, the full scale negative ion source for ITER, is taken as the main reference in the design.

The BUG-MLE grid configuration has an aperture diameter equal to 14 mm, a distance between two apertures of 20 mm and an extraction gap of 6 mm, to reproduce the ITER-HNB distance, while the acceleration gap is chosen to be 12 mm. This distance is decided because it was adopted in a previously performed experimental campaign [17], thus the experimental data could be compared afterwards.

In contrast to [11], no repeller electrode is installed in BUG-MLE, as can also be seen from Figure 3.3. Another key difference is the size of the CESMs, whose section is changed from 6 mm $\times$ 5 mm to 6.8 mm $\times$ 3.4 mm.

The most important change is the addition of the ADCMs, also embedded in the top half of the EG in addition to the CESM: they are 2 mm $\times$ 16.2 mm $\times$ 4 mm (width $\times$ height $\times$ depth), and are added to correct the beamlet zig-zag deflection in the divergence optimum, as reported in [28].

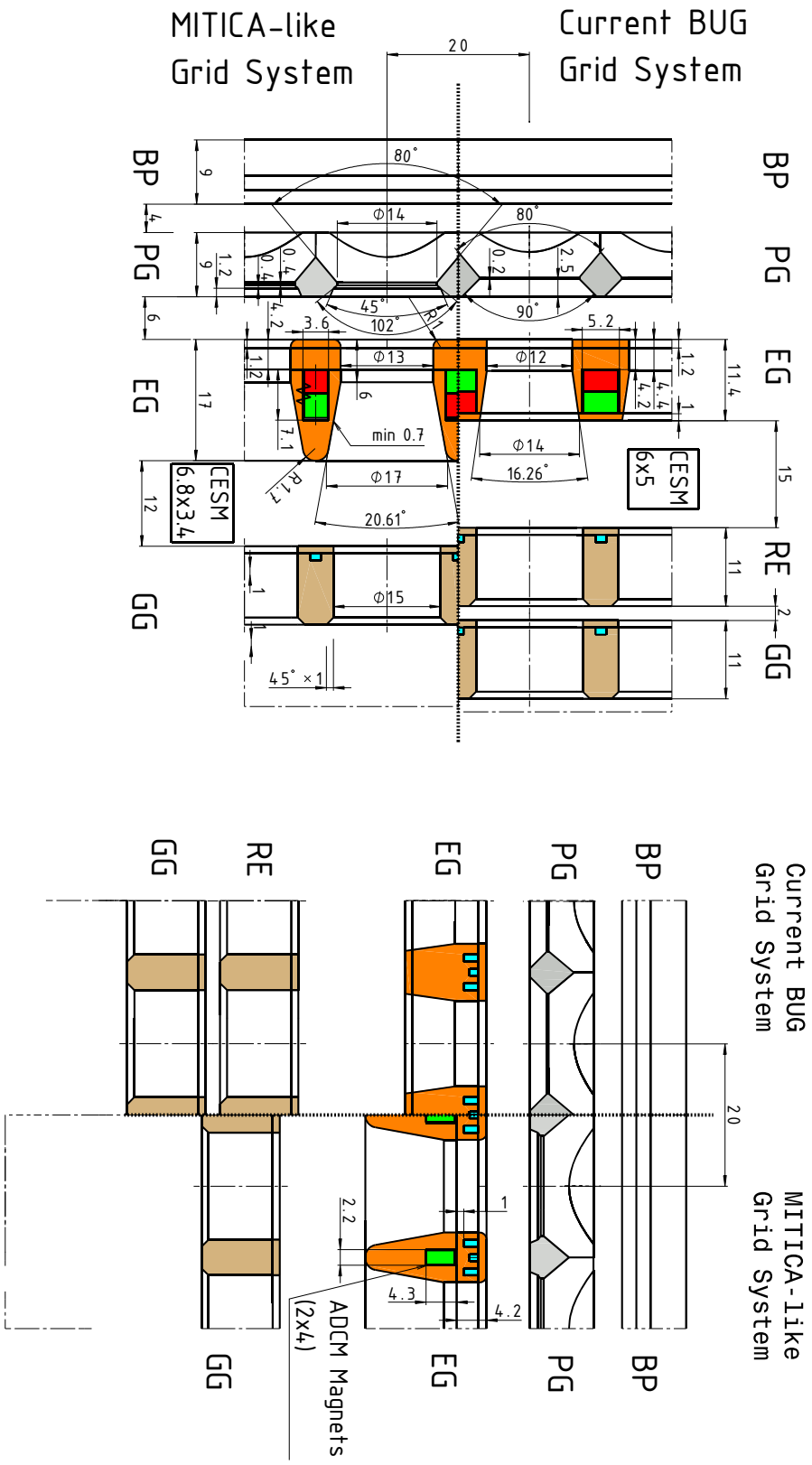

Figure 3.3: Technical drawing of the BUG geometry shown together with the BUG-MLE geometry, with ITER-HNB plasma grid and extraction grid [28].

The magnetic field configurations due to the permanent magnets of BUG and of BUG-MLE are reported in Table 3.2. In particular, the following absolute values, relative to the vertical component of the magnetic field, are given:

- $Max|B_z|$, maximum of the field.
- $|B_z(x = 0)|$, value of the field at the start of the PG.
- $x(B_z = 0)$, on-axis location where the field changes sign.
- $|B_z|$ peak ratio, ratio of the upstream and downstream peak.
- B_{CESM} and B_{ADCM}, magnet remanences.

where the x axis is the beam direction, with origin set at the PG.

Configuration	$Max\|B_z\|$ (mT)	$\|B_z(x=0)\|$ (mT)	$x(B_z=0)$ (mm)	$\|B_z\|$ peak ratio	B_{CESM} (T)	B_{ADCM} (T)
BUG	61.6	7.52	22.32	1.00	1.10	—
BUG-MLE	59.1	7.15	23.92	1.66	1.10	1.10

Table 3.2: Magnetic field design parameters at BUG and BUG-MLE compared [28].

As can be noticed, the addition of the ADCMs creates an asymmetry in the field configuration to actively correct the left/right shift of the beamlets, while keeping the other field parameters almost constant.

In this experimental campaign, the ADCMs are installed only in the top-half of the grid, as it can be seen in Figure 3.5. In this way, it is possible to observe the difference between the compensated half of the grid and the uncompensated one, by comparing the results of the different diagnostics.

Furthermore, the grid apertures can be masked in order to isolate single beamlets or to detect specific grid features. Two main maskings were adopted:

- **Two-halves** masking, in which the two central rows are blocked, represented in Figure 3.4.
- **Single beamlet** masking, like the one displayed in the bottom-left corner of fig. 3.1, in which one single compensated beamlet is isolated in the top-half (aperture 53), while the bottom part of the grid is left unmasked.

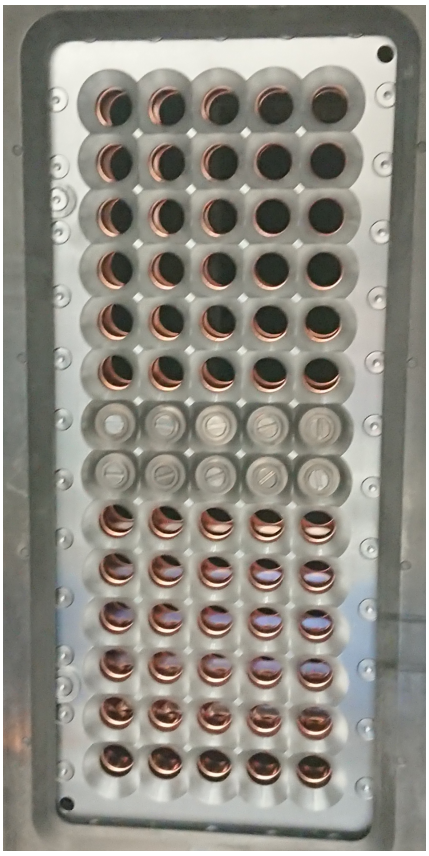

Figure 3.4: Picture of the masked grid: two-halves masking.

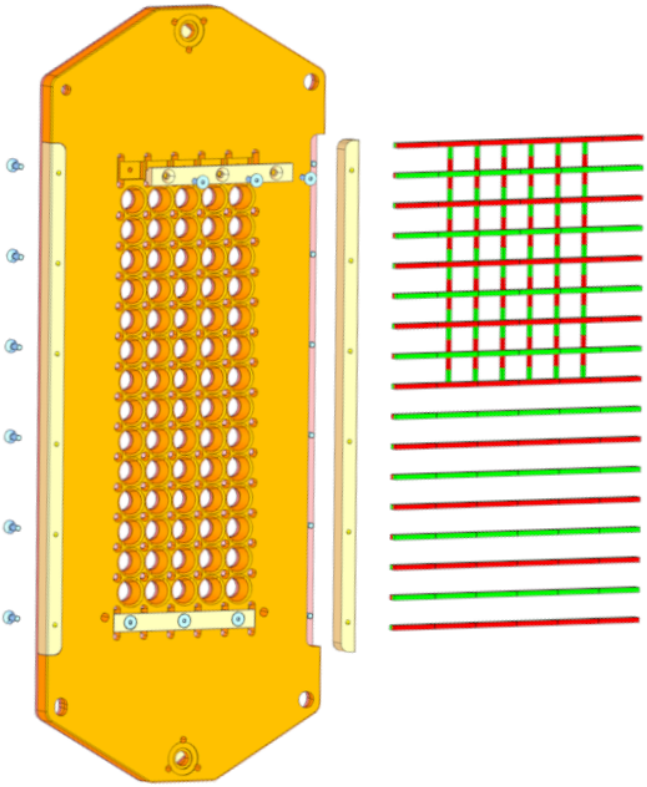

Figure 3.5: Magnets installation on the EG. The ADCMs are installed only on the top half of the grid.

3.2. Diagnostic systems

3.2.1. Beam Emission Spectroscopy on BATMAN-Upgrade

The BES system installed on BATMAN-Upgrade is composed of 16 optic heads looking at the beam. Each optic head is inserted in the vacuum vessel and is positioned at the same angle of 57° with respect to the undeflected beam direction (meaning that $\theta = 180° - 57° = 123°$, see Figure 3.6). The optic heads are distributed along the horizontal and vertical dimensions of the beam to characterize the beam itself with a certain spatial resolution. In particular, the first 5 (BES01) are positioned closer to the grids at 26 cm with respect to the other 11 (BES02) which are at 129 cm, arranged in the vertical direction, as it can be seen in Figure 3.6.

The light collected by each detector is carried by optical fibres to the spectrometer, and the spectrum is recorded through a camera, properly triggered by the electronic system.

The ends of many fibres are vertically piled in front of the entrance slit of the same spectrometer and are properly aligned and calibrated. The slit width (20µm) is chosen for obtaining a good resolution (the width of the input line cannot be zero for

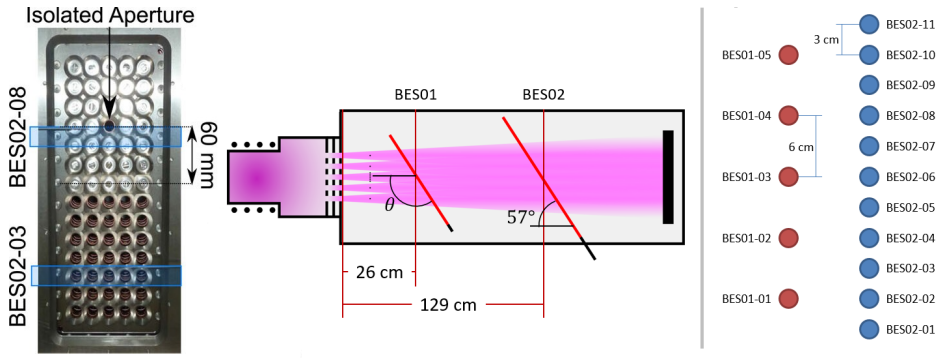

Figure 3.6: Schematics of the BES installation on BATMAN-Upgrade.

obvious reasons, but it also cannot be too wide due to the light broadening induced by diffraction) and a balance between linear diffusion losses and spectrum precision.

The system is calibrated with the Neon emission spectrum, setting the centre of the wavelengths' range at 653.288nm. In this way, it is possible to include both the unshifted peak and the Doppler-shifted one in the 12nm window provided by the experimental set-up.

Before acquiring the spectra, a shutter is used to cover the slits and a background-camera-noise scan is performed, in order to reduce the signal-to-noise ratio in further analysis. In fact, despite the cooling system which allow to reduce thermal noise, the electronic noise can affect significantly the spectra acquisition, hence, in order to avoid applying filters which could bias the data, this technique is preferred.

The analysis is performed through a series of MATLAB scripts which follows the guidelines of the previous chapter 2.2.1 to evaluate divergence and to plot and fit the peaks in the spectra, for each Line Of Sight (LOS).

3.2.2. CFC calorimeter

The 1D-CFC calorimeter installed on BUG-MLE is a $376 \times 142 \times 20\text{mm}^3$ tile composed of carbon fibers, aligned in a way that the tile has anisotropic thermal material properties, but linear mechanical properties for the whole temperature range [24].

The target is placed with its face perpendicular to the beam and centred with respect to the extraction grids at a distance of 866 mm from the beam acceleration system, so that it can intercept $\gtrapprox$ 90% of the beam power and spatially resolve individual beamlets.

The tile is inside a thin-walled copper conduit called dummy neutraliser and is sustained by a frame built out of two Cu-Oxygen Free Electronic (OFE) supports on top and bottom, connected on one side with a molybdenum strip.

The supports are connected to the rotation mechanism, which allows the tile movement in and out of the beam path, as signalled by the arrow in fig. 3.1. In this way, when it is not necessary, the target is protected from the beam and placed parallel to the inner wall of the dummy neutraliser. The supports of the frame are

also fundamental for the camera alignment: in fact, they are provided with some alignment patterns stencilled with graphite spray, that by direct observation allows the complete image focusing. As already mentioned, the data is collected via an external IR camera installed in a port on the side of the vacuum tank, with a resolution of 640×480 pixels for frame rates $\leq 50\,\mathrm{Hz}$.

A planar Cu-OFE mirror, inclined by 55°, permits the visualisation of the reflected infrared light from the back of the CFC, as drawn in fig. 3.1. A teleobjective (angle of view 15°) makes it possible to get the full target in frame over the 1.6 m distance. Thanks to the combination of camera, mirror and teleobjective, the system is able to produce high resolution images ($\leq 0.7\mathrm{mm/pixel}$ on the CFC).

The recorded pictures are then post processed via `MATLAB` routines, which correct the perspective, detect the beamlets' area of impact on the tile, perform the conversion from pixels to mm and produce 3D-plots of the temperature change as a function of the position.

The important thing in science is not so much to obtain new facts as to discover new ways of thinking about them.

William Lawrence Bragg

4 Simulations

After having outlined the theoretical (chapter 2) and experimental background (chapter 3), it is now possible to study in detail the action of the ADCMs on the BUG-MLE experiment in several different experimental conditions and thus to infer the range of parameters worth scanning during the experimental campaign, deducing beforehand eventual dependencies and interesting relationships.

In particular, this preliminary study follows a simulation approach, using two main particle tracking programs: IBSimu and BBCNI, whose details are displayed in section 4.1. In sections 4.3 and 4.4, the main results are presented, reporting graphs and some analysis of the simulations implemented respectively for the CFC and the BES.

4.1. Tools

As previously mentioned, the main software used for CFC calorimeter and BES simulations are IBSimu (Ion Beam Simulator) and BBCNI (Bavarian Beam Code for Negative Ions), presented in the following sections. IBSimu is employed because it is able not only to track particles, but to self-consistently calculate the electric field including the space charge. BBCNI, on the other hand, requires as inputs the field files, but can run forward simulations of the BES diagnostic to produce synthetic spectra and is used especially for this reason.

4.1.1. IBSimu

IBSimu [29] is a particle tracking program used to simulate the ion beam generation in the context of this thesis. This C++ based code allows simulation for charged particle optics with space charge with an iterative procedure.

In particular, it can solve electric fields in many different geometries: 1-dimensional, 2D with both planar of cylindrical symmetry, or full 3D space simulations. The simulation domain is a rectangular mesh with uniform step size.

IBSimu computes electrostatic potentials via finite difference methods that solve Poisson's equation:

$$\nabla^2 \phi = -\frac{\rho}{\epsilon_0} \tag{4.1}$$

also including the non-linear behaviour of plasma for ion extraction in ρ:

$$\rho = \rho_{\text{ion}} - \rho_{e0} \exp\left[\frac{\phi - \phi_P}{kT_e/e}\right] \tag{4.2}$$

where ϕ_P is the plasma potential, T_e the electron temperature, ρ_{ion} the ion charge density (calculated from beam current density) and ρ_{e0} the electron charge density (set to ρ_{ion} at plasma potential).

Given that both ϕ and ρ are initially unknown, IBSimu starts each simulations by solving eq 4.1 for a null space charge ρ (Laplace equation) and deriving ϕ: the *vacuum solution*. With this potential, the particle trajectories are computed. At this point, the space charge for this solution is found and used to solve the Poisson equation (4.1) for the next step. This process is repeated iteratively until convergence.

More in details, to derive particle trajectories, an adaptive Runge-Kutta method is employed. The algorithm integrates the equations of motion, derived from Lorentz force, and automatically adjusts the step-size for reaching the required trajectory accuracy.

By tracking which mesh units each particle cross, the code detects both collisions and space charge, by depositing charges on the corners of these mesh units (4 in 2D simulations, 8 for 3D ones).

To compute the electric fields, mandatory for inferring the particle trajectories, the algorithm relies on numerical differentiation and interpolation of potential, using for each mesh node its closest neighbours.

Boundary conditions and magnetic fields can be imported and adapted from other programs, making IBSimu also very flexible.

In this work, IBSimu is used for simulating the single-beamlet formation, creating aperture-wise simulations with 100000 particles each. The particle data is then analysed in order to obtain what is expected experimentally on the CFC calorimeter plane.

In particular, a series of `Python` routines are coded in order to process the IBSimu-produced particle trajectories, and hence to obtain a projection of the deposited power density at 0.9209 m from the GG, i.e. on the CFC calorimeter, in different experimental conditions. The power density spatial distribution is then represented in 3D plots to obtain pictures similar to the ones obtained by the infrared camera

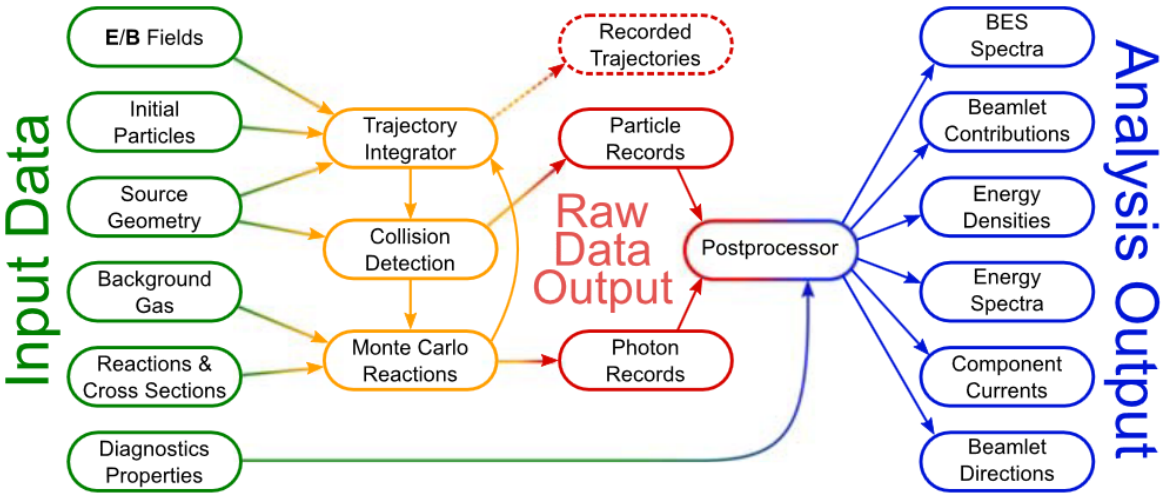

Figure 4.1: Overview of the structure of BBCNI. Input data is shown on the left, processing modules in the centre, and outputs on the right.[30]

pointed at the CFC calorimeter.

Moreover, each single-aperture power density distribution is fitted with a double-gaussian fit, from which a lot of information is inferred.

4.1.2. BBCNI

BBCNI [30] is a Fortran-based code whose main aim is to simulate beam diagnostics data, linking the single beamlet properties and interactions with the global, volume-averaged results collected by experimental tools. A graphical representation of the BBCNI functioning is reported as a flowchart in Figure 4.1, going from the main inputs (on the left) to the outputs (on the right).

In a BBCNI simulation negative ions (H^- or D^-) are initialised in the plasma close to the PG, with initial position sampled from a disk of a user-defined radius at a certain distance from the PG. In this work, the radius is the aperture radius 9.97 mm and the distance is set to 2.73 mm (edge of the PG).

Particles are accelerated through pre-supplied 3D electric and magnetic field maps. Fields are provided by importing them from other programs, for example IBSimu electrical fields can be read, improving the adaptability of BBCNI simulations. However, since the fields are aperture-specific, although beamlet formation is modelled accurately, beamlet-beamlet interaction is not considered.

The beamlet particles are then tracked and eventual collisions with physical objects like walls or grids are recorded. Following this, a Monte Carlo routine checks for collisions between particles and if a reaction with the background gas occurs, it proceeds to register it, re-computing again the new trajectories.

Then, by tracking the various reactions, it detects the photons emitted and associates to each of them a weight, interpreted as an intensity value, calculated from the

gas density at the particle location and the cross section of the relevant reaction.

Afterwards, records of generated photons are used to generate the synthetic diagnostic data by the post-processor, in particular the simulated BES spectra for each line of sight. From particle records it is also possible to derive information that otherwise will be unavailable in the experiment, such as beam neutralisation fraction and particle energy spectra and to simulate other diagnostics (e.g. the CFC calorimeter).

In this work, the main use of BBCNI is to simulate the expected experimental outcomes especially for the Beam Emission Spectroscopy. The experimental parameters in which to simulate the BES spectra are chosen depending on the results of IBSimu simulations, since the electrical fields adopted are generated by this code. More specifically, 11 full-grid simulations have been run, reproducing a total voltage scan (constant voltage ratio of 6.5) and a voltage ratio scan (constant total voltage of 37.5 kV) in a constant normalised perveance regime $\frac{P}{P_0} \approx 0.28$.

In the processing routine, at first, the data is fetched and the main system parameters (telescope acceptances, optic heads positions...) are imported, then the spectra are properly denoised by fitting the background with a polynomial function and the area around the peaks is detected and fitted with a gaussian function.

4.2. General simulation routine

4.2.1. Single aperture processing and analysis

Setting up the main simulation parameters is the first step of the analysis. Thanks to a `Python` script that writes the `C++` files required for IBSimu launch, the simulations are initialised by setting the following parameters:

- n_{apr}, the number of aperture considered, labelled from 1 to 70 starting from the bottom left to upper right of the grid;
- U_{ext}, extraction potential, in V;
- U_{acc}, acceleration potential, in V;
- J_{inj}, injected current density, in $\mathrm{A\,m^{-2}}$;
- I_{PG}, plasma grid current, in kA.

For each set of parameters, an aperture-wise IBSimu simulation with 100000 particles is run, with the provided magnetic fields (top-half of the grid with the ADCMs, bottom half without them).

Particles trajectories are recorded and graphs like the ones in Figure 4.2 are produced.

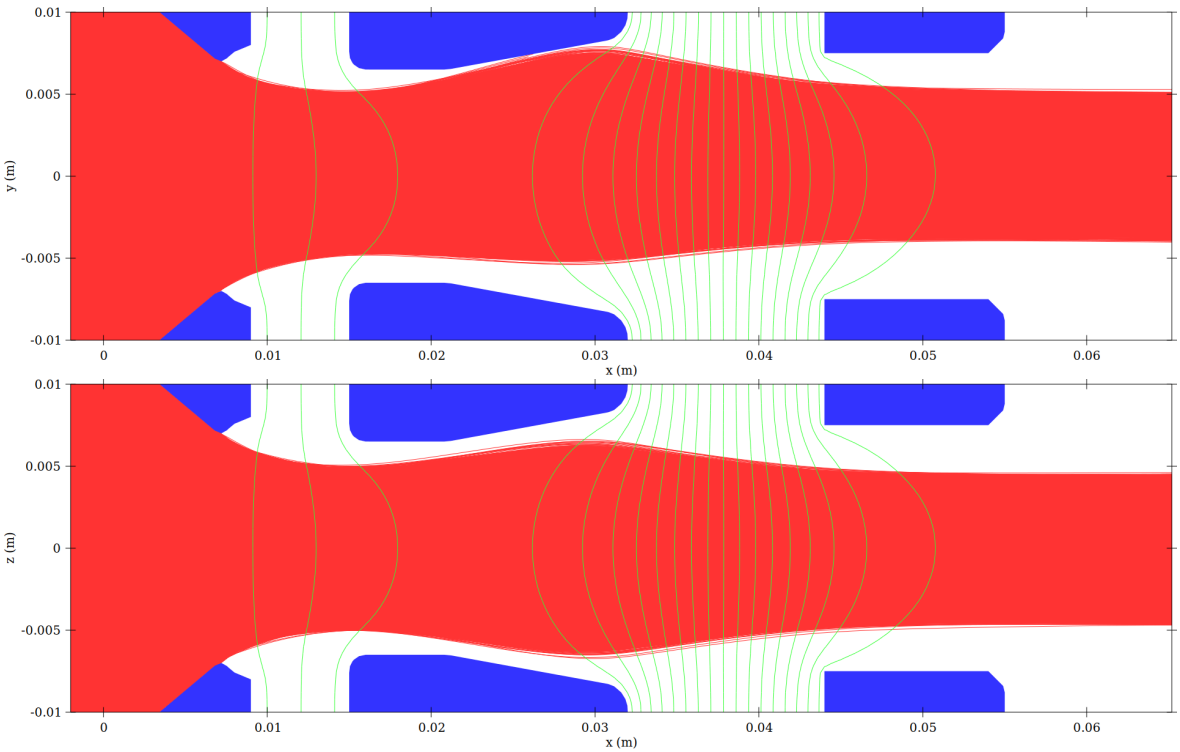

Figure 4.2: Particle trajectories computed via IBSimu, for aperture 53 with $U_{ext} = 5\,\mathrm{kV}$, $U_{acc} = 29\,\mathrm{kV}$, $J_{inj} = 150\,\mathrm{A\,m^{-2}}$, $I_{PG} = 1.5\,\mathrm{kA}$. The blue areas represent the grid profiles (from left to right: PG, EG, GG), the red strings are the trajectories. The plot on the top (bottom) represents horizontal (vertical) positions versus the beamlet axis. Green lines represent isocontours of the electrostatic potential.

It is then possible to analyse in a more detailed way the particle data. More specifically, from the simulated data the following quantities are inferred:

- the normalised perveance $\frac{P}{P_0}$, with $P = \frac{I_{ext}}{U_{ext}^{3/2}}$ and $P_0 = \frac{4}{9}\pi\epsilon_0\sqrt{\frac{2e}{m}}\left(\frac{R}{d_{grids}}\right)^2$, according to equations (2.6), (2.7);
- average particle position on the CFC calorimeter plane $\bar{x}, \bar{y}, \bar{z}$;
- beamlet divergence (both relative to y and z direction and total).

Afterwards, more detailed and advanced analysis are conducted. In particular, the angular distribution in the vertical and horizontal direction is derived from the particle velocities and plots similar to the one in Figure 4.3 are obtained. The y and z distributions are fitted independently with two gaussians, which are also represented in fig. 4.3.

Finally, particle data at the CFC calorimeter plane is read and examined. To do so, the power density in $\mathrm{W\,m^{-2}}$ is computed by multiplying the current conveyed by the particles times the particle kinetic energy, and dividing then for the area impacted by the particles[1]. This quantity can be fitted with a double gaussian distribution, sum of

[1]Dimensionally, the current is in $\mathrm{A} = \mathrm{C\,s^{-1}}$, the energy is computed in $\mathrm{eV} = \mathrm{J\,C^{-1}}$ making the final result correctly in $\mathrm{W\,m^{-2}}$.

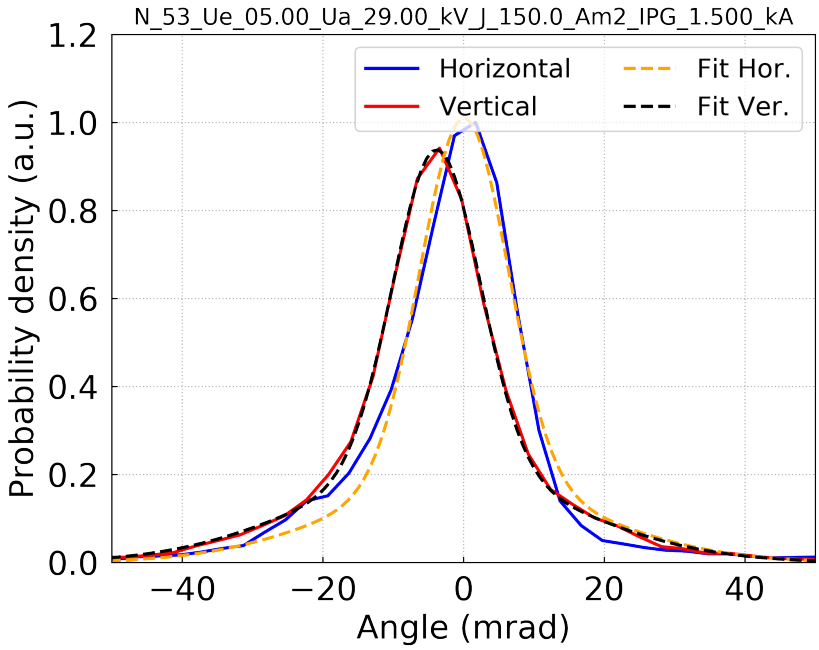

Figure 4.3: Particle angular distribution at the exit of the GG, with respective gaussian fits, for aperture 53 with $U_{ext} = 5\,\mathrm{kV}$, $U_{acc} = 29\,\mathrm{kV}$, $J_{inj} = 150\,\mathrm{A\,m^{-2}}$, $I_{PG} = 1.5\,\mathrm{kA}$.

two 2D gaussian contributions, each with the following expression:

$$g(y,z,\theta) = A \times \exp\left(-\left[\left(\frac{\cos^2\theta}{2\sigma_y^2} + \frac{\sin^2\theta}{2\sigma_z^2} \right)(y-y_0)^2 + \left(\frac{\sin^2\theta}{2\sigma_y^2} + \frac{\cos^2\theta}{2\sigma_z^2} \right)(z-z_0)^2 + \left(-\frac{\sin 2\theta}{2\sigma_y^2} + \frac{\sin 2\theta}{2\sigma_z^2} \right)(y-y_0)(z-z_0) \right] \right) \tag{4.3}$$

where A is the normalisation factor dependent on the total deposited power, θ is the axis rotation angle, (y_0, z_0) the gaussian centre coordinates, σ_y, σ_z the standard deviations in the y, z direction.

The fitting function is therefore:

$$G(y,z,\theta) = f_c \cdot g_{core}(y,z,\theta) + (1-f_c) \cdot g_{halo}(y,z,\theta) \tag{4.4}$$

The two gaussian contributions are labelled as *core* gaussian and *halo* gaussian, and their total area is normalised depending on a parameter $f_c \in (0,1)$ which quantifies the weight of the core gaussian with respect to the halo one. The core gaussian should be able to detect better the intensity peak position, while the halo one is implemented to describe better the asymmetric area around the beamlet centre. Thus, the fit results from the core gaussian are used as better estimate for the beamlet centre position.

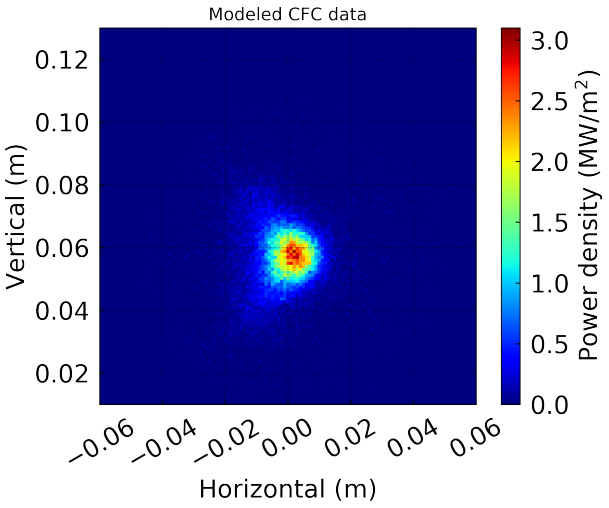

Figure 4.4: Power density map of the simulated particles, for aperture 53, $U_{ext} = 5\,\mathrm{kV}$, $U_{acc} = 29\,\mathrm{kV}$, $J_{inj} = 150\,\mathrm{A\,m^{-2}}$, $I_{PG} = 1.5\,\mathrm{kA}$.

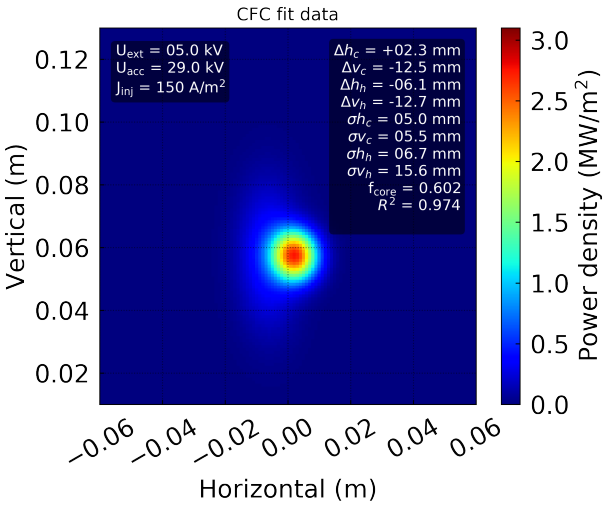

Figure 4.5: Fitted power density, for aperture 53, $U_{ext} = 5\,\mathrm{kV}$, $U_{acc} = 29\,\mathrm{kV}$, $J_{inj} = 150\,\mathrm{A\,m^{-2}}$, $I_{PG} = 1.5\,\mathrm{kA}$.

The fitting routine produced graphs similar to the ones in Figures 4.4, 4.5. In the picture on the left, the simulated IBSimu data is represents in a power density plot, showing the heat load on the calorimeter pertaining to the ions, for a single aperture (in this specific case, aperture 53), at $U_{ext} = 5\,\mathrm{kV}$, $U_{acc} = 29\,\mathrm{kV}$, $J_{inj} = 150\,\mathrm{A\,m^{-2}}$, $I_{PG} = 1.5\,\mathrm{kA}$. On the right, instead, the results of the fit of this data are displayed.

In both plots, the horizontal and vertical axis refer to the position of the aperture in the whole tile, while the position derived from the fit procedure are relative to the aperture centre.

In particular, in the top-right corner all the fit parameters are reported, namely:

- Δh_c, horizontal displacement of the core gaussian centre with respect to the aperture centre;
- Δv_c, vertical displacement of the core gaussian centre with respect to the aperture centre;
- Δh_h, horizontal displacement of the halo gaussian centre with respect to the aperture centre;
- Δv_h, vertical displacement of the halo gaussian centre with respect to the aperture centre;
- σh_c and σv_c, core gaussian horizontal and vertical width;
- σh_h and σv_h, halo gaussian horizontal and vertical width;
- f_{core}, fraction of the core gaussian area with respect to the halo one;
- R^2, evaluation of the goodness of fit.

All the data produced and the fit results are then stored so that they can be further analysed and to produce more advanced plots.

4.2.2. Full CFC tile simulations

After performing the already described single aperture analysis, the derived data is combined to obtain full-tile graphical representation.

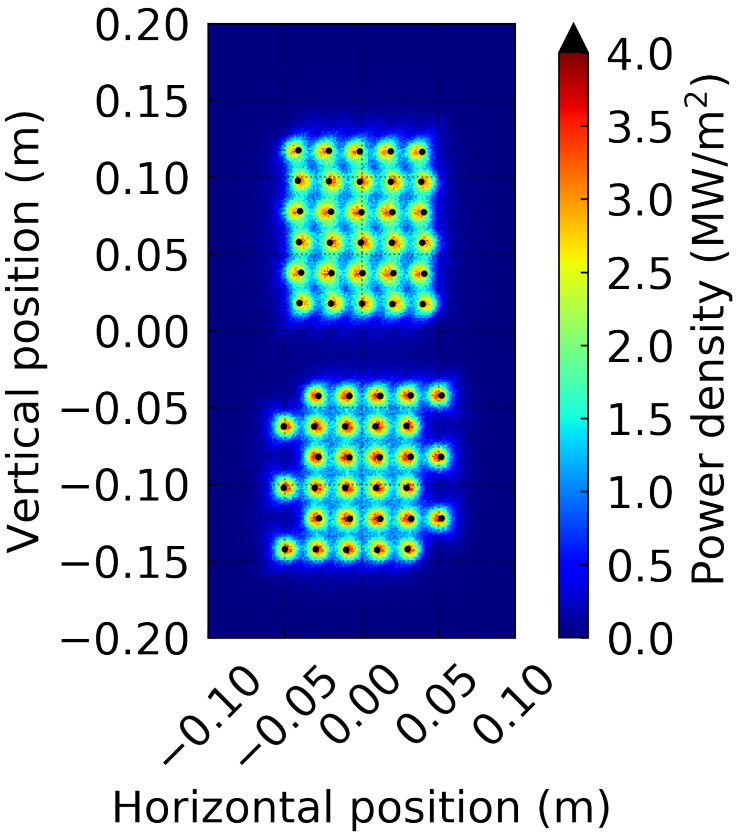

Figure 4.6: Full CFC tile power density plot, for $U_{ext} = 5\,\text{kV}$, $U_{acc} = 29\,\text{kV}$, $J_{inj} = 150\,\text{A}\,\text{m}^{-2}$, $I_{PG} = 1.5\,\text{kA}$, with estimate of beamlet centres (black dots).

The masking strategy adopted consist of blocking the middle two rows (apertures from 31 to 40), in order to have a clear division between top and bottom half of the grid. Remembering that the ADCMs are installed only on the top half, one should be able to observe the zig-zag deflection correction effect compared to the uncompensated half.
An example of a full tile representation is reported in Figure 4.6, which shows a full-grid simulation at $U_{ext} = 5\,\text{kV}$, $U_{acc} = 29\,\text{kV}$, $J_{inj} = 150\,\text{A}\,\text{m}^{-2}$, $I_{PG} = 1.5\,\text{kA}$. The black dots represent the average particle position, i.e. an estimate of the beamlet centres.

The action of the ADCMs is evident: the zig-zag deflection is almost perfectly compensated in the top half of the grid, while in the bottom half it is still clearly present. One can carefully notice that the average particle position seems to be slightly different from the intensity peak: this is an effect due to the non-gaussian shape of the beamlets.

4.3. CFC calorimeter simulation results and analysis

The standard analysis routine described above is applied several times to every set of simulation parameters, in order to obtain multiple simulations and to compare the different experimental conditions.

In particular, focusing on the zig-zag correction effect of the ADCMs on the horizontal direction y, the key quantities considered are the **average particle position** $\bar{y}$, and the **beamlet centre position**, estimated with the horizontal position of the core gaussian y_{core}. Another relevant variable is the **average horizontal angle** y_{angl}, measured 10mm after the GG, which was originally studied for the ADCMs design.

Their values are computed and compared for 2 different apertures: aperture 53, at the centre of the top-half of the grid, and 13, in the bottom half. These two apertures are chosen because they are both positioned on the central column of the grid, meaning that they are less subject to field edge effects at the boundaries of the system. Moreover, the magnetic field has the same polarity, hence the direction of the uncompensated field is the same and changes in the magnetic field configuration are, to first order, only a result of the ADCMs.

Give these premises, to predict the action of the ADCMs three different 2D scans are considered, for the two aforementioned apertures. In these scans, $\bar{y}$ and y_{core} are studied as a function of the injected current density J_{inj} and of a voltage-related quantity, which will be either the acceleration voltage U_{acc} at a fixed extraction voltage U_{ext}, or the voltage ratio $U_{ratio} = U_{acc}/U_{ext}$ at a constant total voltage $U_{tot} = U_{acc} + U_{ext}$, or the total voltage U_{tot} at a constant voltage ratio U_{ratio}. For the first scan, also the average horizontal angle is analysed.

The range of the parameters considered are reported in Table 4.1. Some simulations are beyond the capabilities of BUG-MLE, so they are not representative of physical results, however, their results are nevertheless reported to outline possible tendencies for stronger machines.

Scan type	U_{ext} [kV]	U_{acc} [kV]	U_{tot} [kV]	U_{ratio}	J_{inj} [A m^{-2}]	I_{PG} [kA]
$U_{acc} - J_{inj}$	5	[20; 40]	[25; 45]	[5; 8]	[100; 300]	1.5
$U_{ratio} - J_{inj}$	[3; 6.5]	[31; 34.5]	37.5	[4.8; 11.5]	[100; 250]	2.2
$U_{tot} - J_{inj}$	[3; 7]	[19.5; 45.5]	[22.5; 52.5]	6.5	[100; 250]	2.2

Table 4.1: Parameters range of the simulations performed, for apertures 53 and 13.

For each parameter investigated in each 2D scan, contour plots are produced, putting on the $x-$axis the injected current density, and on the $y-$axis the voltages. Generally speaking, in each graph a colour code is adopted, representing with red positive values of $\bar{y}$, y_{core} or y_{angl} and with blue negative ones.

Three black lines, representing the contours over which a certain fraction of beam current (signalled on the label) is scraped on the grids, are also displayed, in order to signal which data points are not "physical". In fact, they represent situations of over-perveance similar to fig. 2.4.(c), in which current is pushed into the PG apertures artificially by the simulation, while experimentally these results will never

be achieved.

Furthermore, in some cases the normalised perveance P/P_0 is used as horizontal axis, so as to have insight also on this physical quantity, strictly related to the optical properties of the beam ((2.6), (2.5)). In this case the points for which the scraped current is more than 10% of the beam current are neglected and excluded from the plot.

All this analysis is executed with the aim of outlining the optimum area for the correction effect of the ADCMs, i.e. the area in which the estimated horizontal position of beamlets is close to 0, and to evaluate which set of parameters are particularly relevant to be observed experimentally.

Besides, from the generated graphs a selection of parameters set will be chosen to create full-grid simulations with BBCNI, which will not only provide a comparison for the CFC data, but also the simulation of the BES. More specifically, those points will be represented in the figures as small crosses. They are selected by choosing U_{ext}, U_{acc}, J_{inj} so that P/P_0 is in the range $[0.26; 0.28]$. Given that P/P_0 is the similarity criterion for the beamlet optical properties, keeping this parameter constant allow proceeding with a more coherent and consistent comparison.

4.3.1. $U_{acc} - J_{inj}$ scan

Average horizontal angle y_{angl} and particle position $\bar{y}$

In Figures 4.7, 4.8 the 3D contour plots of J_{inj} vs U_{acc} vs y_{angl} are displayed, similar to the ones reported in [28]. In these plots, the uncompensated aperture (13, fig. 4.7) produces a beamlet with a net negative angle in the $[-26; -5]$ mrad interval, with a decreasing tendency as the acceleration potential and the injected current density increase, of course ignoring the area of the graph over the 0.5 line, which represents points not possible to obtain experimentally.

On the other hand, the action of the ADCMs on aperture 53 (fig. 4.8), while preserving this trend, has the evident effect of shifting the deviation average more towards 0: in fact, the average horizontal angle varies in the $[-9; +7]$ mrad interval, but a clear belt of points with values very close to 0 can be outlined.

Equivalent trends are present also in Figures 4.9, 4.10, which represent the average particle position at the CFC plane for the same U_{acc}, J_{inj} already described.

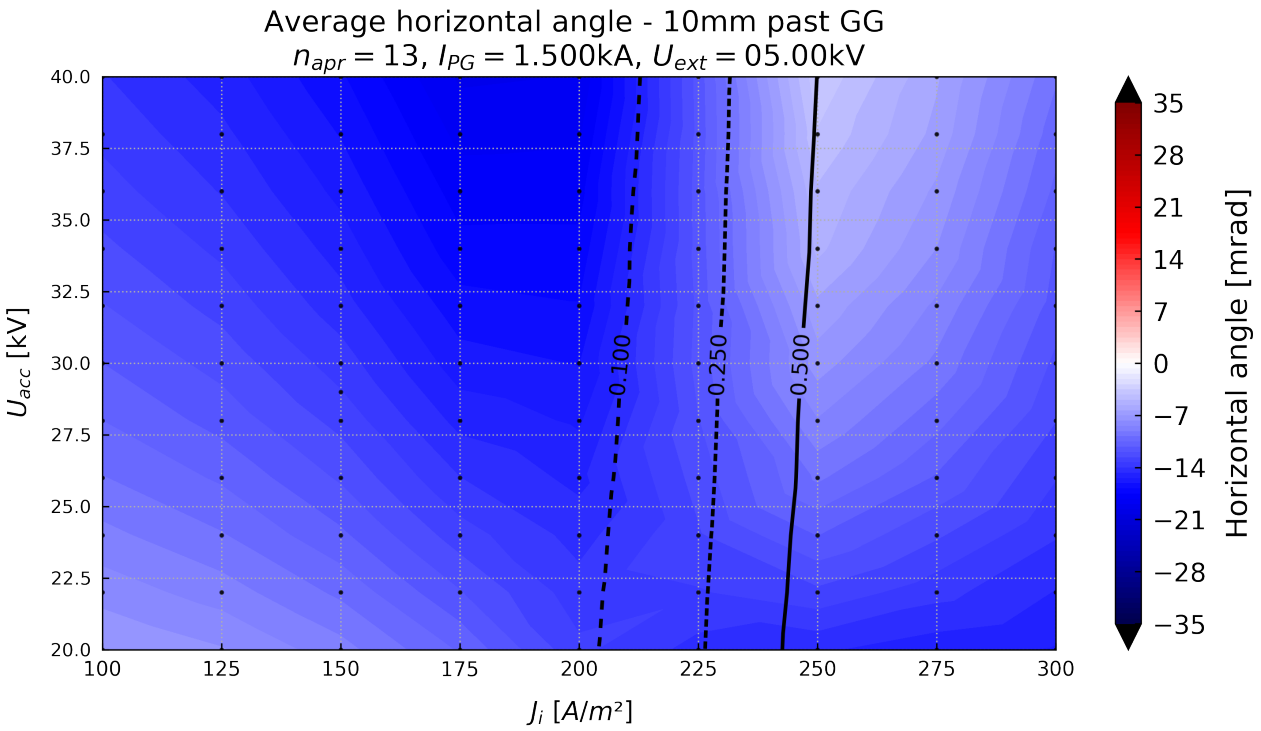

Figure 4.7: Average horizontal angle for aperture 13, measured 10 mm past the Grounded Grid, as a function of both J_{inj} and U_{acc}, $I_{PG} = 1.5\,\mathrm{kA}$, $U_{ext} = 5\,\mathrm{kV}$.

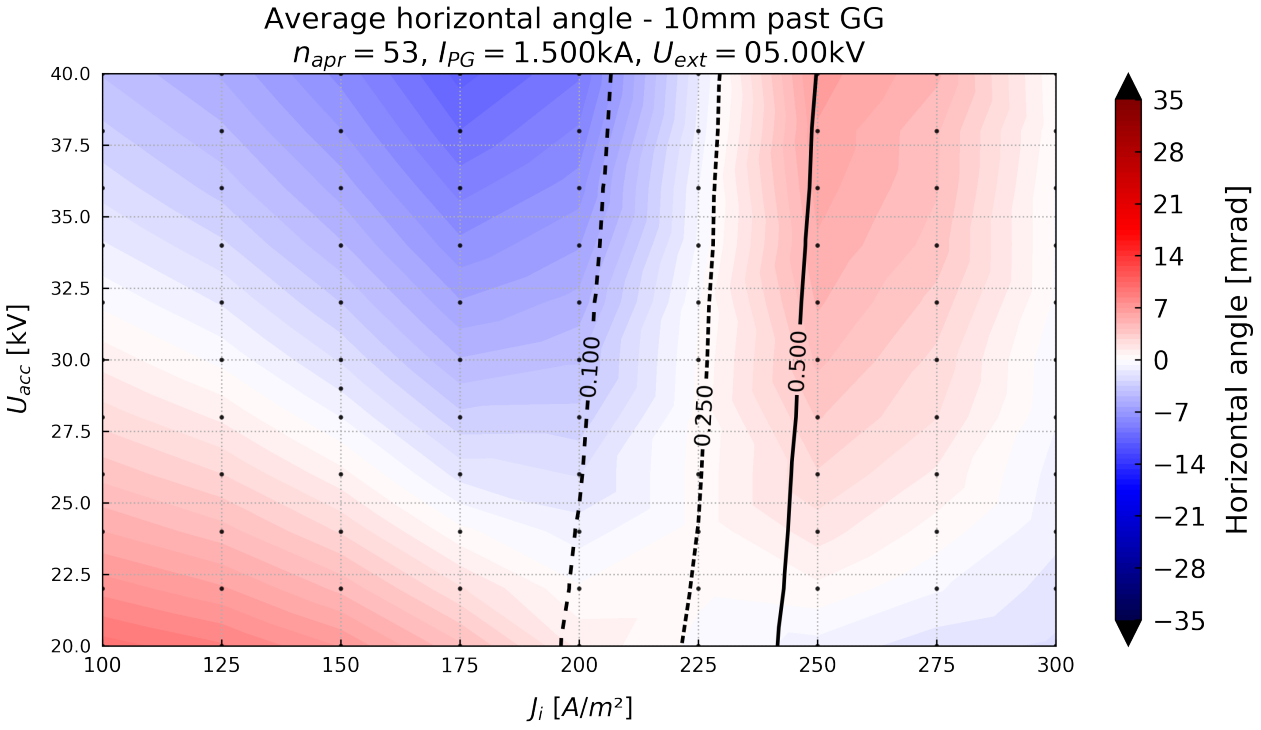

Figure 4.8: Average horizontal angle for aperture 53, measured 10 mm past the Grounded Grid, as a function of both J_{inj} and U_{acc}, $I_{PG} = 1.5\,\mathrm{kA}$, $U_{ext} = 5\,\mathrm{kV}$.

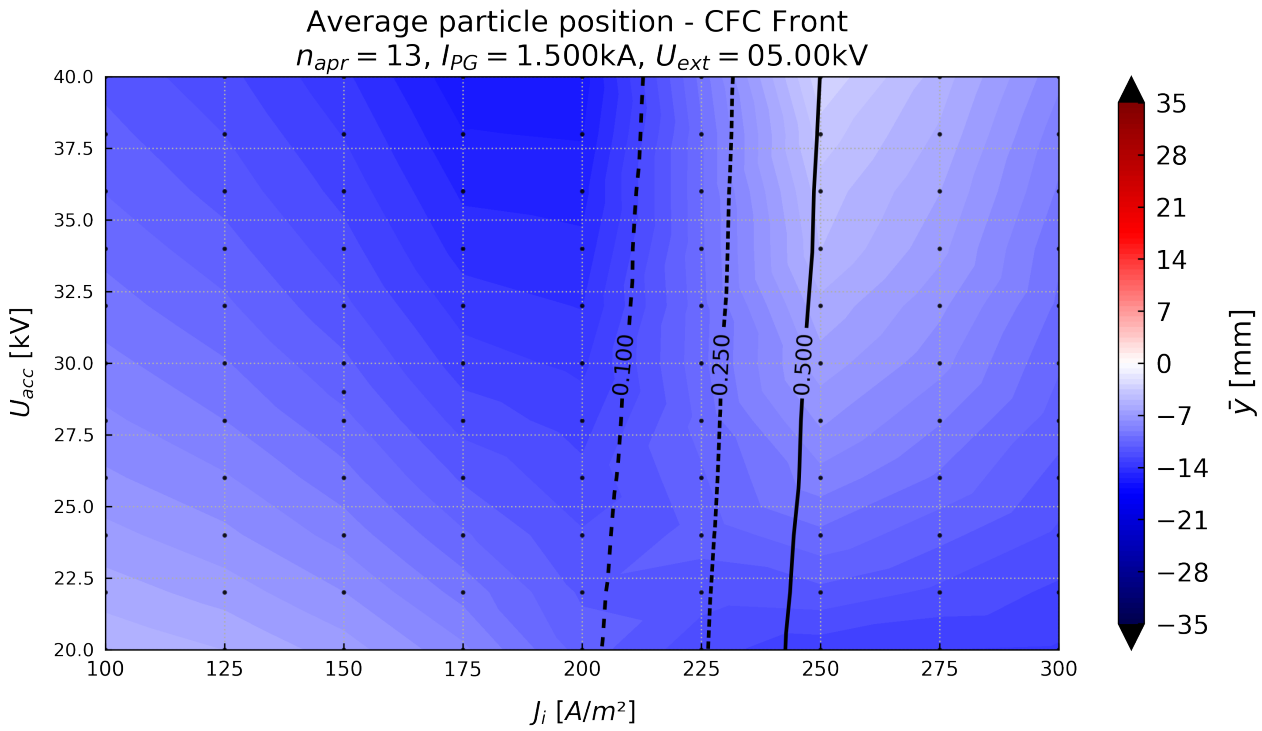

Figure 4.9: Average particle position at the CFC plane for aperture 13, as a function of both J_{inj} and U_{acc}, $I_{PG} = 1.5\,\mathrm{kA}$, $U_{ext} = 5\,\mathrm{kV}$.

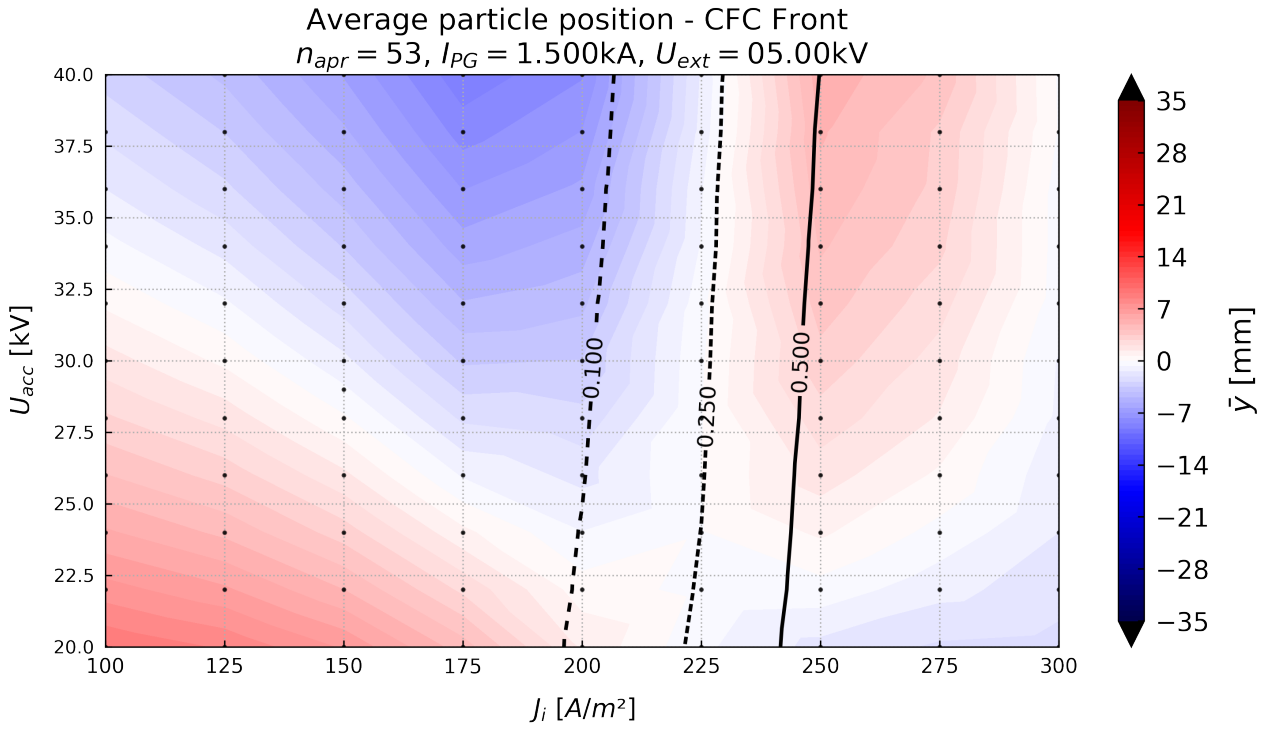

Figure 4.10: Average particle position at the CFC plane for aperture 53, as a function of both J_{inj} and U_{acc}, $I_{PG} = 1.5\,\mathrm{kA}$, $U_{ext} = 5\,\mathrm{kV}$.

This equivalence is due to the relationship between the two quantities: in fact, the magnetic field downstream of the grid has almost no vertical component, and after the grids no change in angle is expected. Moreover, the displacement of the beamlet at the end of the GG is in the range of a few mm, and thus the average beamlet position at the CFC is mostly determined by the angular distribution.

Hence, given the similarity of the behaviour of y_{angl} and $\bar{y}$, for further analysis only the latter is considered, especially because the data is fetched exactly at the calorimeter plane and represents better the physical quantity under examination, i.e. the horizontal beamlet deflection.

Fitted horizontal core location y_{core}

The fit results are much more fluctuating with respect to the raw data simulated with IBSimu, as it can be seen from the following Figures 4.11, 4.12: the fit procedure is more sensitive to the shape of the distribution compared to simply taking the average, and therefore there are more variations in the fitted position.

First of all, it is important to state that the non-uniformities present in both graphs in the bottom-right corner are a consequence of the over-perveant regime, therefore that area is excluded from the analysis.

However, despite the presence of several irregularities and of a behaviour that is not particularly smooth (for example, in the area around the $(175, 26)$ point, for both figures), also in this case the action of the ADCMs is visible. Both graphs show a steep growth of the fitted core location for particularly high and low U_{acc} values, with a central, smooth valley of lower values. The magnitude of the changes remains approximately the same (a range of ≈ 35 mm), but it is shifted towards more positive values by the influence of the ADCMs, which thus acts in correcting the deflection.

It is worth noticing that the area of the aforementioned valley is in the same parameters range as the area of "0 shift" highlighted in the previous paragraph for the compensated aperture. For the uncompensated one, instead, there is a discrepancy between fig. 4.9 (showing the average particle position) and fig. 4.11 (with the fitted core position): there is a region in which $y_{core} \approx 0$mm, whereas the average position and angle are not 0. This is due to the presence of the halo, that biases the average particle position towards negative values, while the fitting procedure focus only on the core, as it can be seen from Figures 4.13 (simulated data) and 4.14 (double gaussian fit). The fact that this behaviour is not present for aperture 53 could mean that the ADCMs also help in focusing better the beamlets, having hence also an impact in improving the fitting procedure.

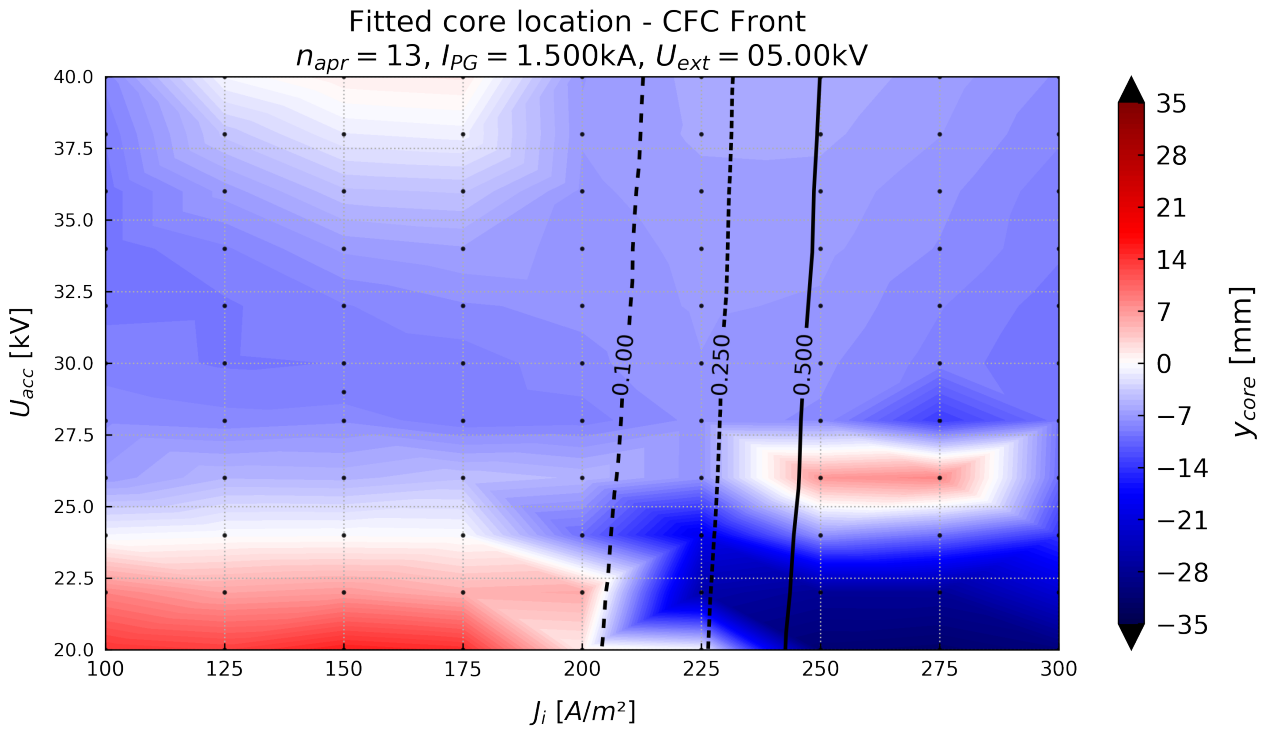

Figure 4.11: Fitted core gaussian horizontal position for aperture 13, as a function of both J_{inj} and U_{acc}, $I_{PG} = 1.5\,\mathrm{kA}$, $U_{ext} = 5\,\mathrm{kV}$.

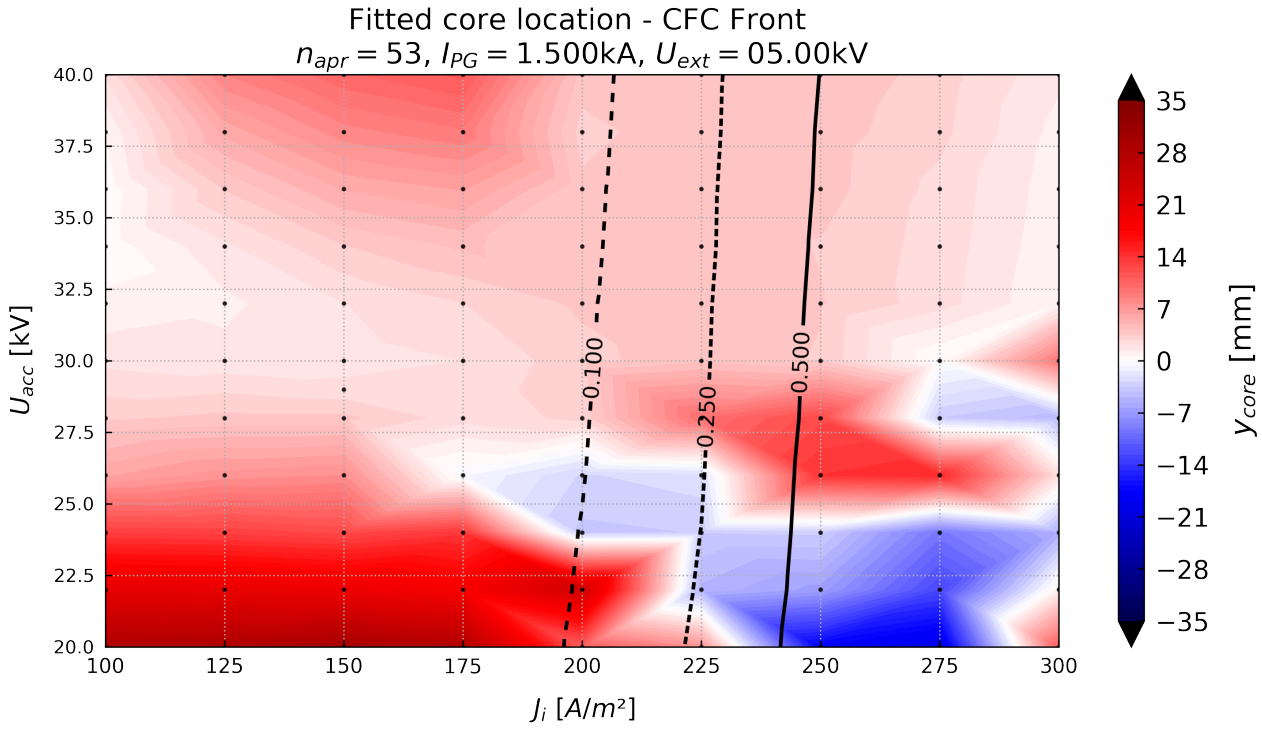

Figure 4.12: Fitted core gaussian horizontal position for aperture 53, as a function of both J_{inj} and U_{acc}, $I_{PG} = 1.5\,\mathrm{kA}$, $U_{ext} = 5\,\mathrm{kV}$.

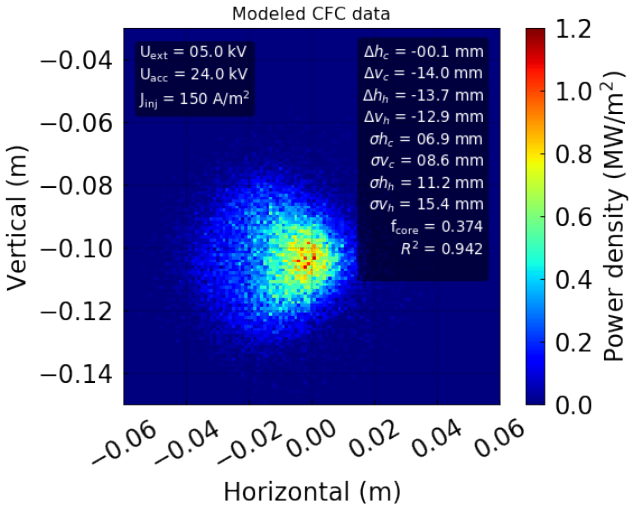

Figure 4.13: Power density map of the simulated particles, for aperture 13, $U_{ext} = 5\,\text{kV}$, $U_{acc} = 24\,\text{kV}$, $J_{inj} = 150\,\text{A}\,\text{m}^{-2}$, $I_{PG} = 1.5\,\text{kA}$.

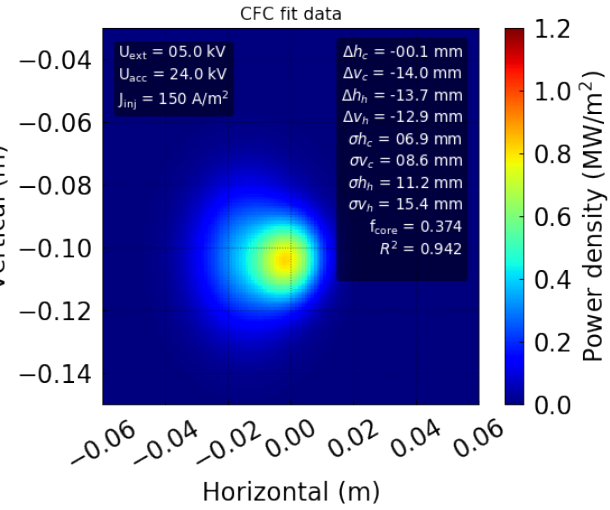

Figure 4.14: Fitted power density at the calorimeter, derived for aperture 13, $U_{ext} = 5\,\text{kV}$, $U_{acc} = 24\,\text{kV}$, $J_{inj} = 150\,\text{A}\,\text{m}^{-2}$, $I_{PG} = 1.5\,\text{kA}$.

4.3.2. $U_{ratio} - J_{inj}$ scan

The next set of parameters considered is a scan in both the injected current density and the ratio between acceleration and extraction potential $U_{ratio} = U_{acc}/U_{ext}$, with the total voltage U_{tot} kept constant and fixed to 37.5 kV.

The plasma grid current is changed to 2.2kA in order to match better the future experimental conditions.

The range in which the voltage ratio is changed is $[4.8; 11.5]$. The points are taken by picking U_{ext} in the interval $[3, 6.5]$ (as reported in 4.1) divided by points in geometric progression, and then deriving $U_{acc} = U_{tot} - U_{ext}$. In this way, the whole U_{ratio} range will be evenly sampled and the intervals between two consecutive points will be almost constant.

Concerning the injected current densities, in this case the range considered is smaller than the one analysed in the previous section: this is done to exclude the over-perveant tendency for higher J_{inj}, hence focusing the analysis on a more relevant area from the experimental point of view of the parameter space.

Average horizontal particle position $\bar{y}$

The 3D-plots for the average particle position are reported in Figure 4.15 for aperture 13 and in Figure 4.16 for aperture 53.

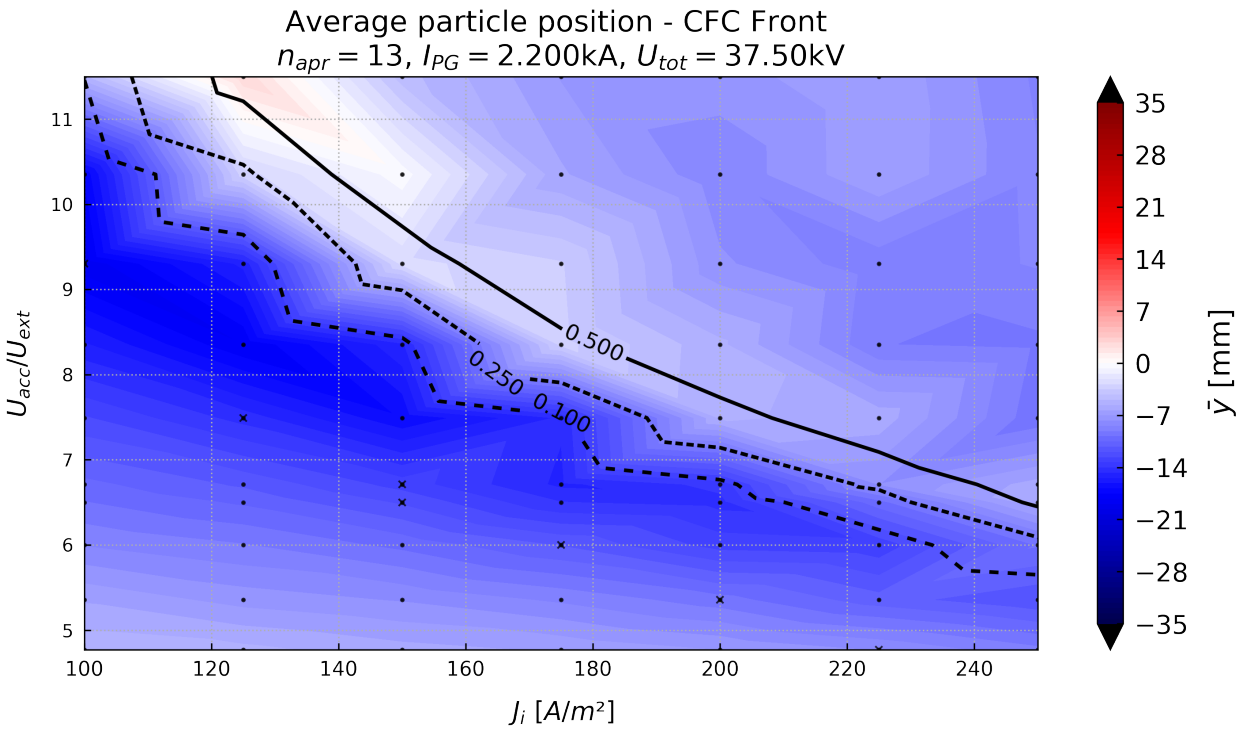

Figure 4.15: Average particle position at the CFC plane for aperture 13, as a function of both J_{inj} and $U_{ratio} = U_{acc}/U_{ext}$, $I_{PG} = 2.2\,\mathrm{kA}$, $U_{tot} = U_{ext} + U_{acc} = 37.5\,\mathrm{kV}$.

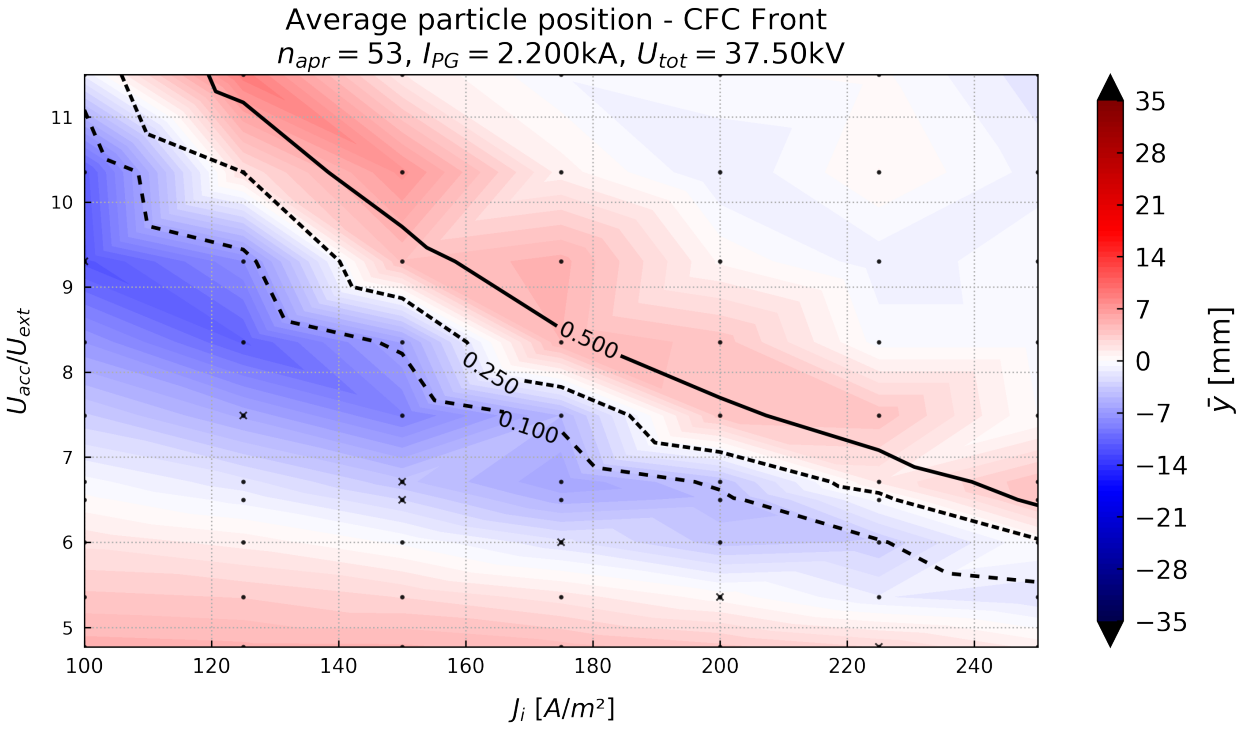

Figure 4.16: Average particle position at the CFC plane for aperture 53, as a function of both J_{inj} and $U_{ratio} = U_{acc}/U_{ext}$, $I_{PG} = 2.2\,\mathrm{kA}$, $U_{tot} = U_{ext} + U_{acc} = 37.5\,\mathrm{kV}$.

To begin with, it is interesting to notice that for aperture 53 there is a belt of values for which the average particle horizontal position is within $\pm$2mm, corresponding to ratios between 5.4 and 6.7. It is expected then that in this region the zig-zag compensation will be optimal, also according to its design [28], moreover the comparison between compensated and uncompensated halves of the grid is expected to show a shift in horizontal position of $\approx$ 1.3cm.

For both graphs, the region for high J_{inj}, U_{ratio} is in over-perveance. In fact, higher ratios mean smaller extraction voltages, and as a consequence higher normalised perveance (at the same J_{inj}), according to eq. (2.6). These regions will not be taken into account for further analysis since the current scraped on the grid system is more than the 50% of the beam current.

In the area of interest, located below the dashed 0.100 line, one can notice a decreasing trend in the average particle position as the voltage ratio lowers. In particular, for aperture 13, $\bar{y}$ changes regularly from -18mm ($J_{inj} = 100\,\mathrm{A\,m^{-2}}$, $U_{ratio} > 9$) to -4mm ($J_{inj} = 100\,\mathrm{A\,m^{-2}}$, $U_{ratio} = 4.8$), with a very little dependence (yet not negligible) on the injected current density and a much more significant one on the voltage ratio.

This is a consequence of the magnetic field structure (Figure 2.3). For aperture 13 (red line in Figure 2.3), the CESM field pulls the beamlet towards the positive side upstream of the EG, and then after the EG the beamlet is pushed to the negative side, because the field changes sign inside the EG. Besides, the electrostatic lens pushes the beamlet back, also towards the negative side. This because when U_{ratio} is high, the extraction voltage is generally low, and thus the beamlet will be more displaced by the upstream CESM field. The same tendency can also be observed for aperture 53, but again, similarly to what stated before, the ADCMs' influence adds a positive shift to the $\bar{y}$ values, changing their range to $[-7; +6]$mm.

This fact is particularly evident if the on-axis horizontal average position is plotted, as in Figures 4.17 (aperture 13) and 4.18 (aperture 53). Already 10 mm past the grids (i.e. on the right hand side of the figures), it is clear how the magnetic field impacts on the trajectories, and why higher ratios corresponds to lower $\bar{y}$ values. In fact, in both graphs the final positions are arranged in the same order (on top the lowest ratios), but end in significantly different absolute values, due to the bending of their trajectories done by the ADCM interaction, particularly visible between the EG and the GG.

To gain even more insight, Figures 4.19, 4.20 are reported, in which the abscissa axis is the normalised perveance, excluding overperveant points, which are defined as the ones for which the current lost on the EG is greater than 10% of the beam current ($J_{EG}/J_{inj} > 0.1$). Both pictures show seem to be only half-filled: this because other than the overperveant points, also the ones with very low current density (which are nevertheless not relevant to this analysis) are excluded from the plot.

In these pictures, a tendency in both P/P_0 and in U_{ratio} is present, given the slope of the contour lines. Points in the top-right part of the graph tend to have more negative values of $\bar{y}$, and again a smooth and steady decreasing behaviour can be outlined, that follows the bottom-left to top-right diagonal. The optimum area for the ADCMs correction is the one with $5 < U_{ratio} < 7$, in which $\bar{y} \approx 0$, according to their design.

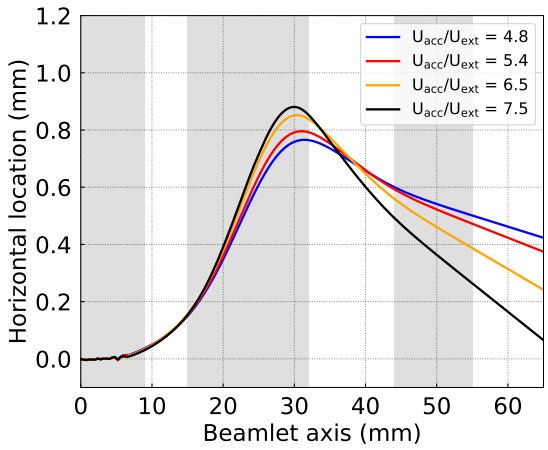

Figure 4.17: Aperture 13, $\bar{y}$ as a function of the beamlet axis through the grid system for different U_{ratio}, for $J_{inj} = 150\,\mathrm{A\,m^{-2}}$, $I_{PG} = 2.2\,\mathrm{kA}$.

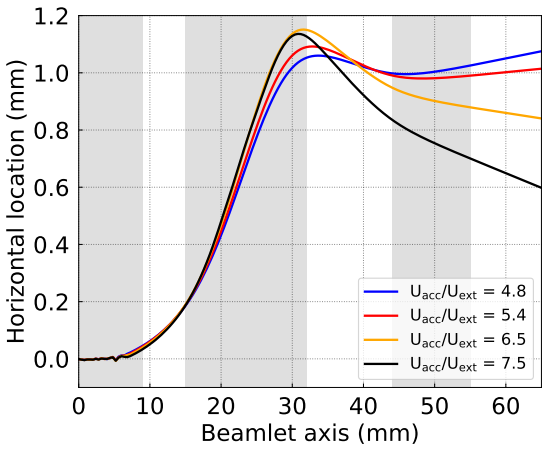

Figure 4.18: Aperture 53, $\bar{y}$ as a function of the beamlet axis through the grid system for different U_{ratio}, for $J_{inj} = 150\,\mathrm{A\,m^{-2}}$, $I_{PG} = 2.2\,\mathrm{kA}$.

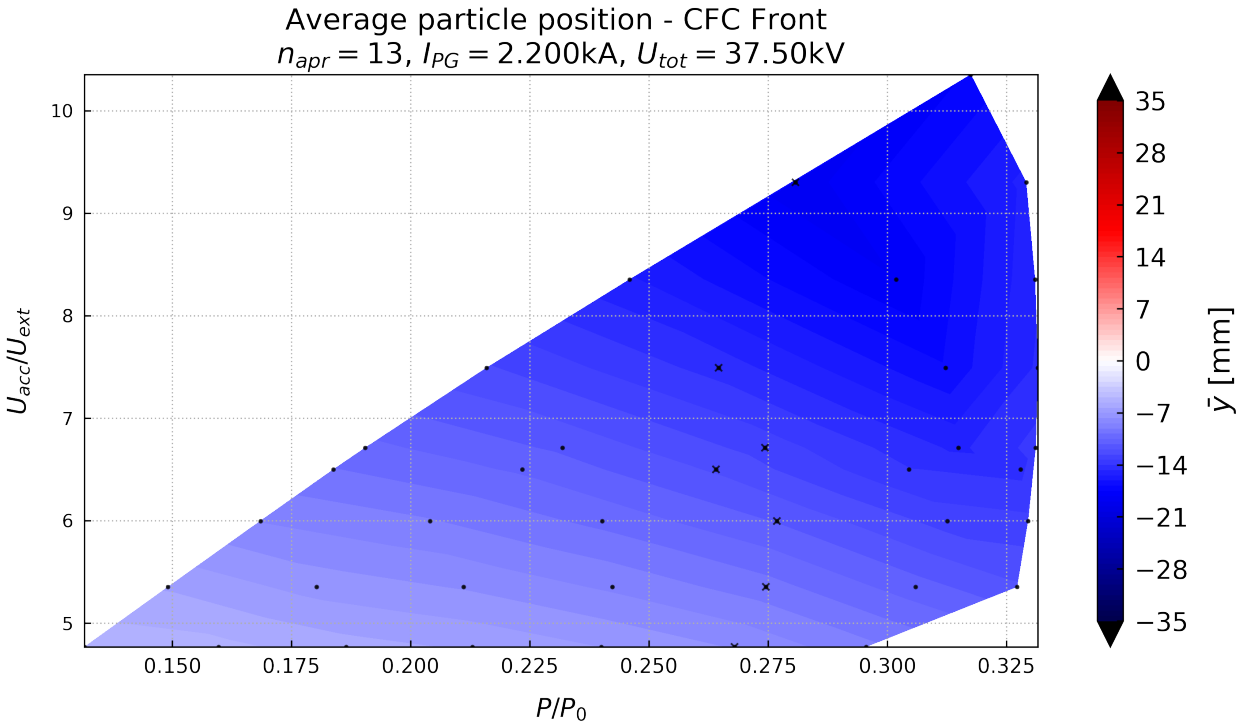

Figure 4.19: Average particle position at the CFC plane for aperture 13, as a function of both P/P_0 and $U_{ratio} = U_{acc}/U_{ext}$, $I_{PG} = 2.2\,\mathrm{kA}$, $U_{tot} = U_{ext} + U_{acc} = 37.5\,\mathrm{kV}$.

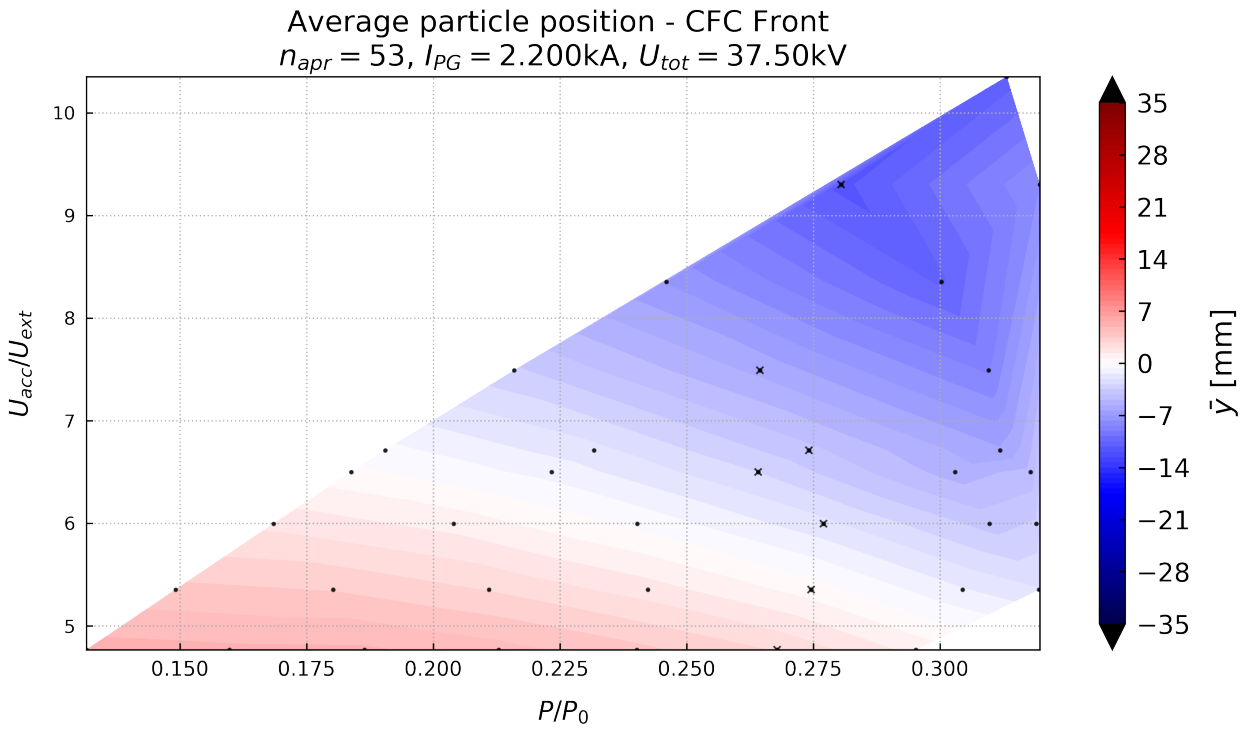

Figure 4.20: Average particle position at the CFC plane for aperture 53, as a function of both P/P_0 and $U_{ratio} = U_{acc}/U_{ext}$, $I_{PG} = 2.2\,\text{kA}$, $U_{tot} = U_{ext} + U_{acc} = 37.5\,\text{kV}$.

Fitted horizontal core location y_{core}

Finally, also for this scan the fitted core horizontal location is studied in Figures 4.21, 4.22. In addition to the previously made considerations about the effect of the ADCMs, in Figures 4.21, 4.22, representing the fitted core position as a function of J_{inj}, U_{ratio} respectively for apertures 13, 53, another feature is shown. For $U_{ratio} \in [5.4; 7.4]$ (hence excluding the irregular area at higher voltage ratios), conversely to what happened in the previous U_{acc} scan, the tendency on J_{inj} has practically disappeared for the lower ratios, meaning that the fitting procedure is not particularly affected by this variable.

However, in the upper part of both graphs, the trend outlined is particularly irregular. Observing the corresponding single aperture plots, one can find that these irregularities are due to a poor fitting procedure, with $R^2 < 0.6$. In fact, in these conditions the extracted particles are spread on a wide area, making the task to detect the intensity peak particularly difficult, as it can be seen from the comparison of two examples for aperture 53 (Figures 4.23, 4.24). In this region the beam is very close to be overperveant and generally has a diverging behaviour.

Nevertheless, the correction effect of the ADCMs is once again visible in the area with voltage ratios between 5 and 7, in which the fitted core position is around 0 mm and where the fitting routine provides reasonable results.

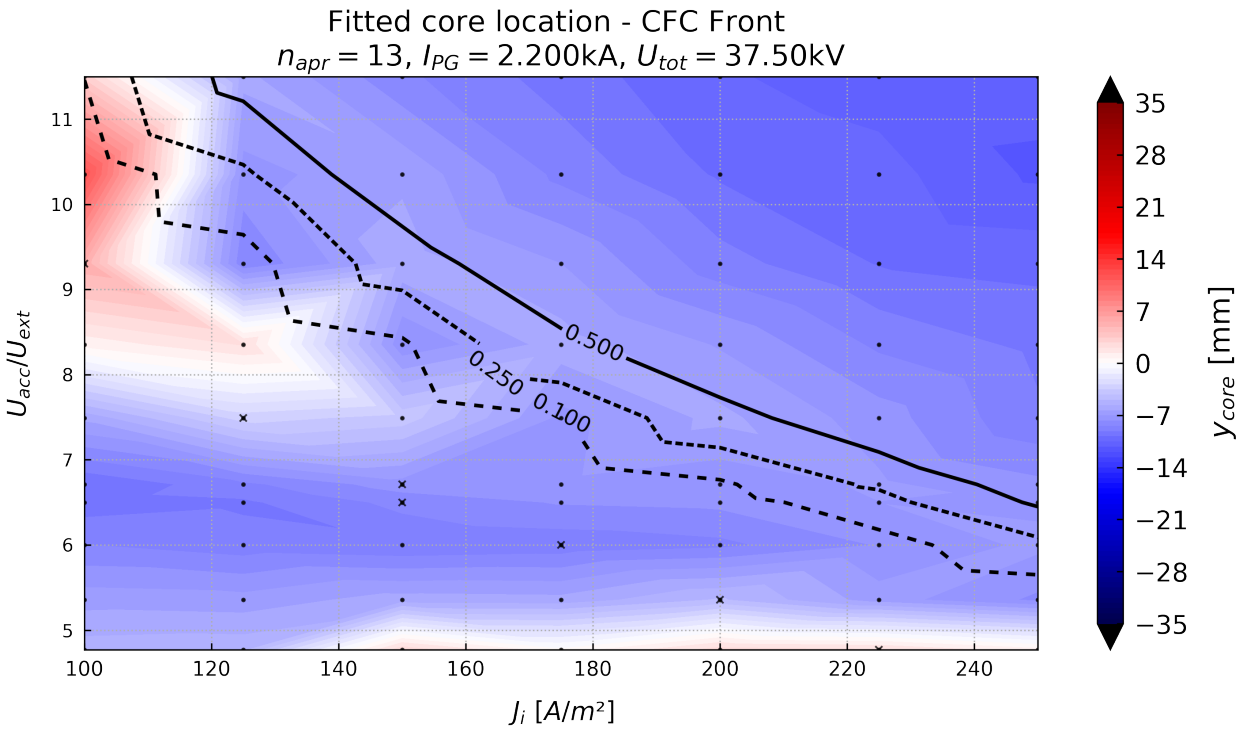

Figure 4.21: Fitted core horizontal position for aperture 13, as a function of both J_{inj} and $U_{ratio} = U_{acc}/U_{ext}$, $I_{PG} = 2.2\,\mathrm{kA}$, $U_{tot} = U_{ext} + U_{acc} = 37.5\,\mathrm{kV}$.

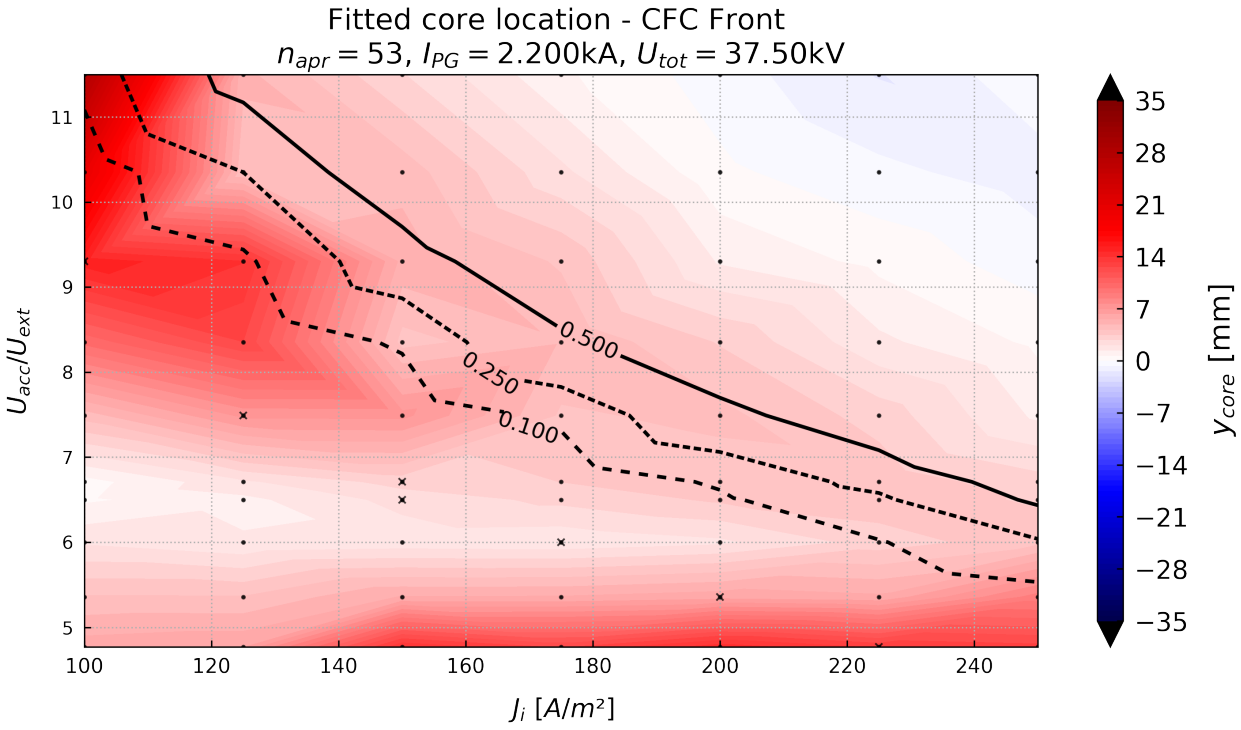

Figure 4.22: Fitted core horizontal position for aperture 53, as a function of both J_{inj} and $U_{ratio} = U_{acc}/U_{ext}$, $I_{PG} = 2.2\,\mathrm{kA}$, $U_{tot} = U_{ext} + U_{acc} = 37.5\,\mathrm{kV}$.

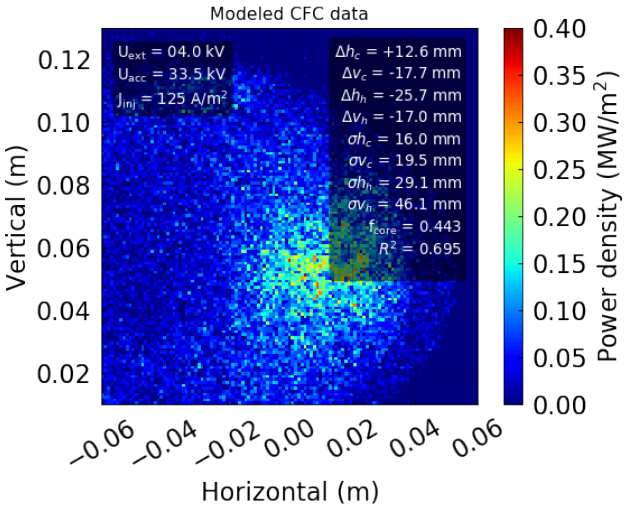

Figure 4.23: Power density map of the simulated particles, for aperture 53, $U_{ext} = 4.01\,\mathrm{kV}$, $U_{acc} = 33.49\,\mathrm{kV}$, $J_{inj} = 125\,\mathrm{A\,m^{-2}}$, $I_{PG} = 2.2\,\mathrm{kA}$.

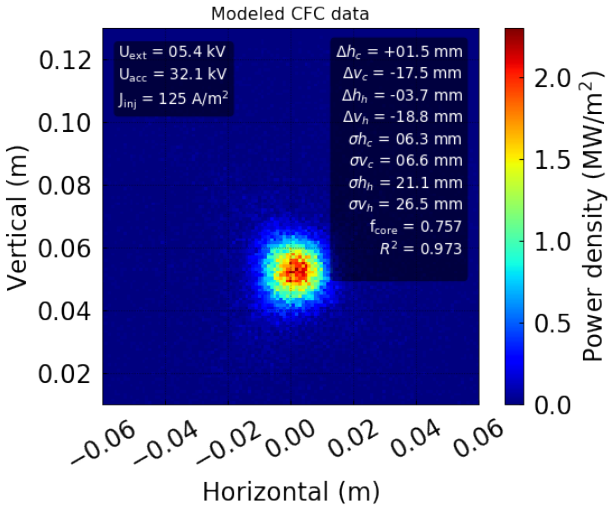

Figure 4.24: Power density map of the simulated particles, for aperture 53, $U_{ext} = 5.36\,\mathrm{kV}$, $U_{acc} = 32.14\,\mathrm{kV}$, $J_{inj} = 125\,\mathrm{A\,m^{-2}}$, $I_{PG} = 2.2\,\mathrm{kA}$.

4.3.3. $U_{tot} - J_{inj}$ scan

In this section, the analysis of the zig-zag deflection correction for apertures 53 and 13 will be presented as a function of the total voltage U_{tot} and the injected current density J_{inj}, at a fixed $U_{ratio} = 6.5$ and $I_{PG} = 2.2\,\mathrm{kA}$.

Average horizontal particle position $\bar{y}$

Concerning $\bar{y}$, comparing Figure 4.25 (for aperture 13) and 4.26 (aperture 53), makes evident what is the action of the ADCMs. The magnets eliminate almost completely the dependence on both J_{inj} and U_{tot}: the great majority of the graph 4.26 is very light coloured (i.e. $\bar{y} \approx 0$mm), with a slight decrease in its values (magnitude of less than 10mm) as we approach the over-perveant region (bottom-right corner of the graph).

On the other hand, fig. 4.25 shows a clear trend with gradient in the top-left direction, and all the values shown in the graph are strictly negative. This is due to the magnetic field configuration [28]. With ADCM, there is only a very weak U_{tot} dependence at fixed perveance, whereas there is a stronger dependence without ADCM. This behaviour is also reflected if we use the P/P_0 as horizontal axis (Figures 4.27, 4.28). In fact, for aperture 53 (fig. 4.28) the range in which the deflection varies is particularly narrow (less than 5mm) and only a light trend in P/P_0 can be seen in the rightmost part of the picture. Conversely, for aperture 13 (fig. 4.27), values are significantly more far from 0mm and a distinct trend can be observed in both U_{tot} and P/P_0, with $\bar{y}$ decreasing along the top-left to bottom-right diagonal. This means that the addition of the ADCMs should make $\bar{y}$ significantly less dependent on the total voltage, effectively correcting the zig-zag deflection.

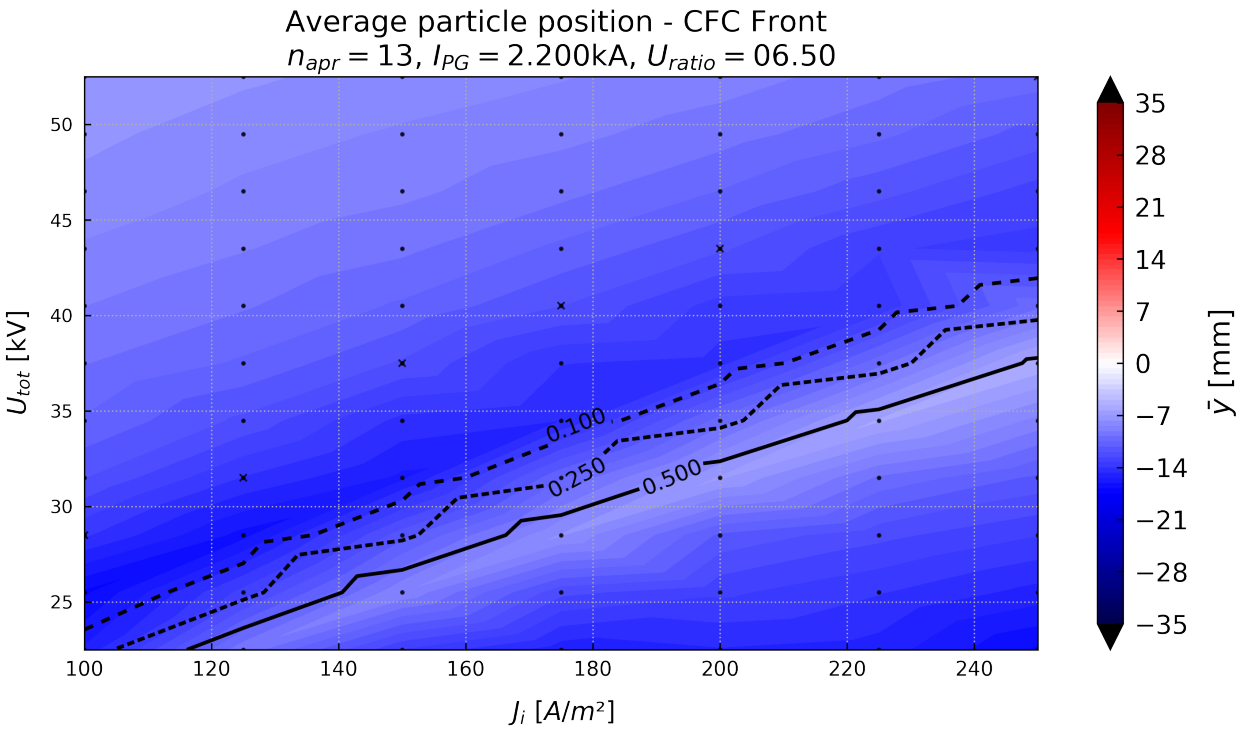

Figure 4.25: Fitted core horizontal position for aperture 13, as a function of both J_{inj} and $U_{tot} = U_{ext} + U_{acc}$, $I_{PG} = 2.2\,\text{kA}$, $U_{ratio} = U_{acc}/U_{ext} = 6.5$.

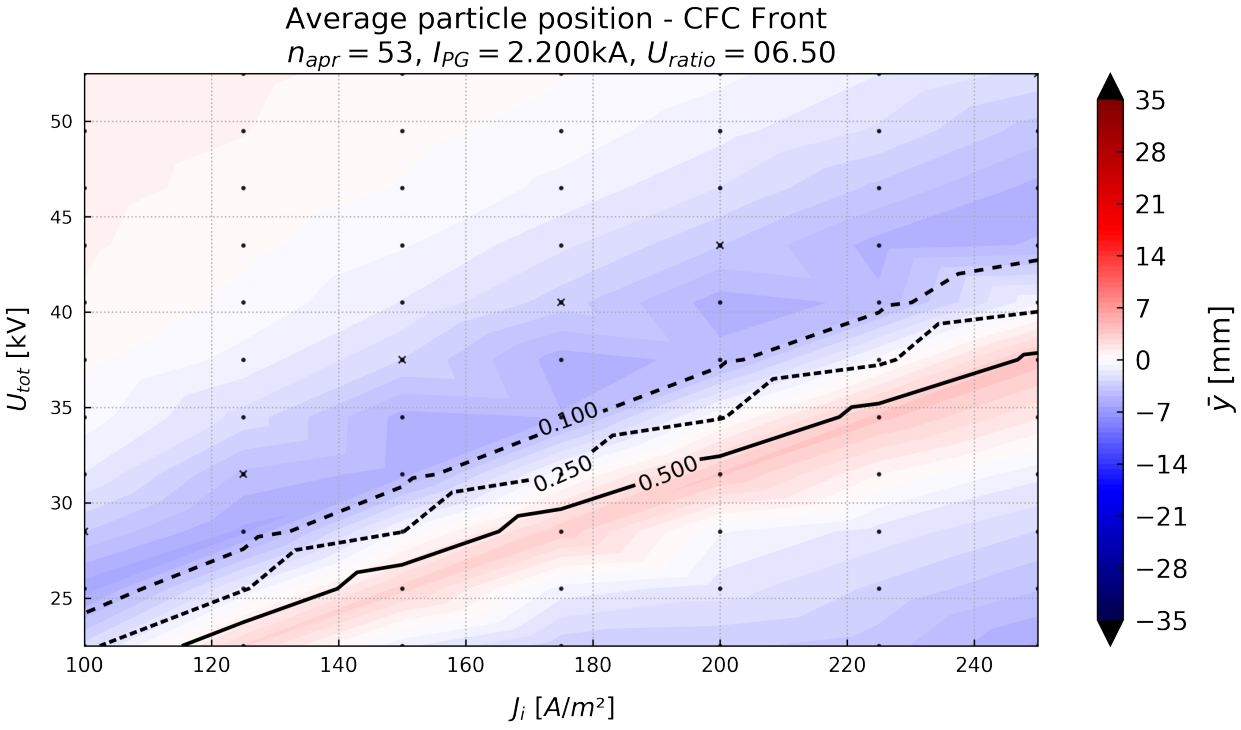

Figure 4.26: Fitted core horizontal position for aperture 53, as a function of both J_{inj} and $U_{tot} = U_{ext} + U_{acc}$, $I_{PG} = 2.2\,\text{kA}$, $U_{ratio} = U_{acc}/U_{ext} = 6.5$.

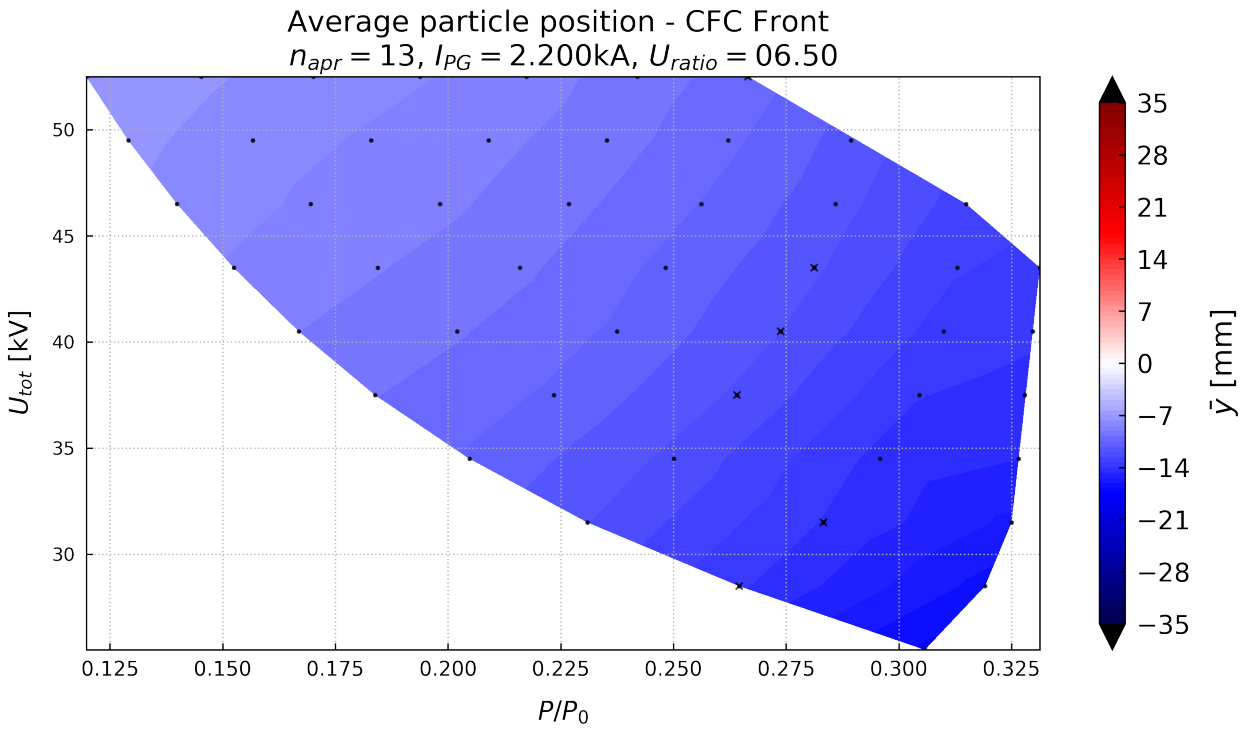

Figure 4.27: Fitted core horizontal position for aperture 13, as a function of both P/P_0 and $U_{tot} = U_{ext} + U_{acc}$, $I_{PG} = 2.2\,\text{kA}$, $U_{ratio} = U_{acc}/U_{ext} = 6.5$.

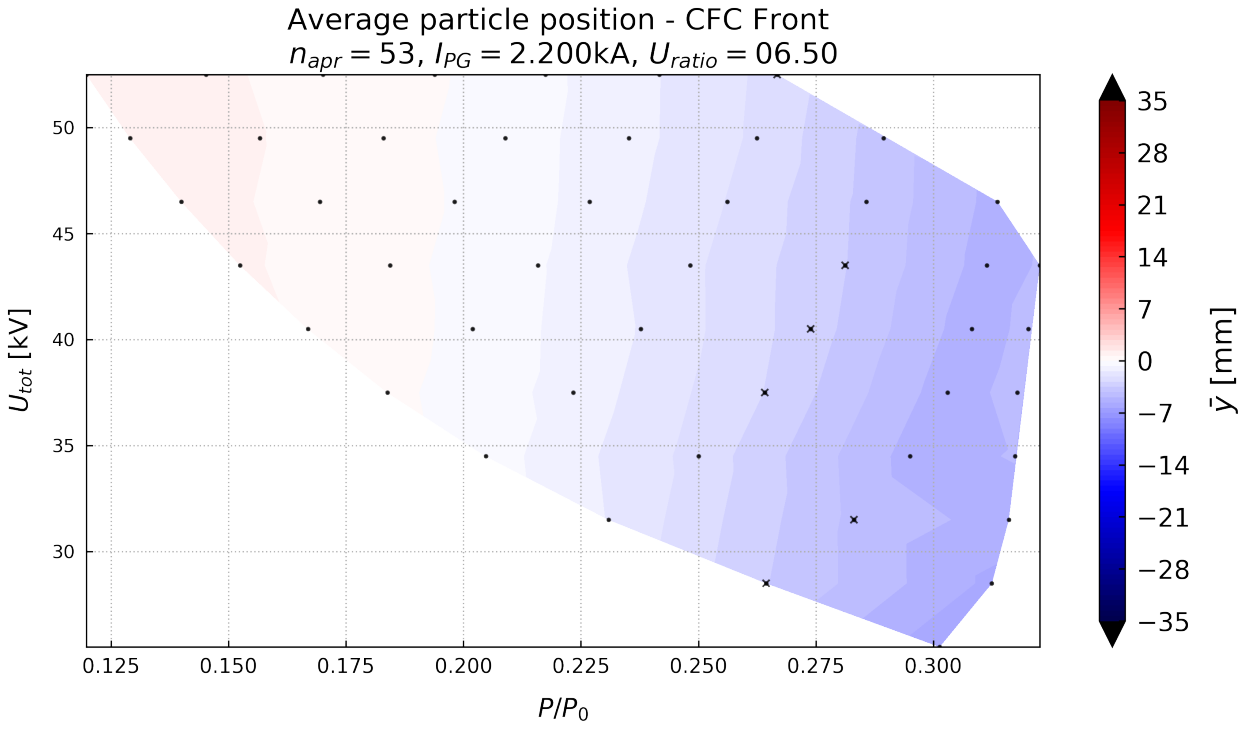

Figure 4.28: Fitted core horizontal position for aperture 53, as a function of both P/P_0 and $U_{tot} = U_{ext} + U_{acc}$, $I_{PG} = 2.2\,\text{kA}$, $U_{ratio} = U_{acc}/U_{ext} = 6.5$.

Fitted horizontal core location y_{core}

Regarding the fitting results, the plots for aperture 13 and 53 (Figures 4.30, 4.31 respectively) are different between each other and from figs. 4.25, 4.26, which show the average particle positions.

As a matter of fact, Figure 4.30 shows a totally different trend: in this case, the horizontal positions decreases following a line almost parallel to the over-perveant boundaries (the three black lines), while in 4.25 the descent was in the orthogonal direction. However, looking at the magnitude of these changes, it can be noticed that y_{core} varies from -3mm to -8mm, which is significantly less with respect to the 15mm of figure 4.25.

Concerning aperture 53, instead, it can be seen that the trend is analogous of the one in figure 4.26, but shifted towards slightly more positive values. Observing the single aperture fits (e.g. Figure 4.29), the reason for this is clear: broadly speaking, in many situations the halo gaussian is not able to capture every single particle, because the beamlet is not particularly focused. Thus, while the average particle position considers also the particles scattered away from the beamlet centre, the fitting procedure focuses on the intensity peak and therefore produces this bias. The goodness of all the fits is generally good ($R^2 > 0.85$, $R^2 > 0.95$ in many cases), meaning that this behaviour is significant.

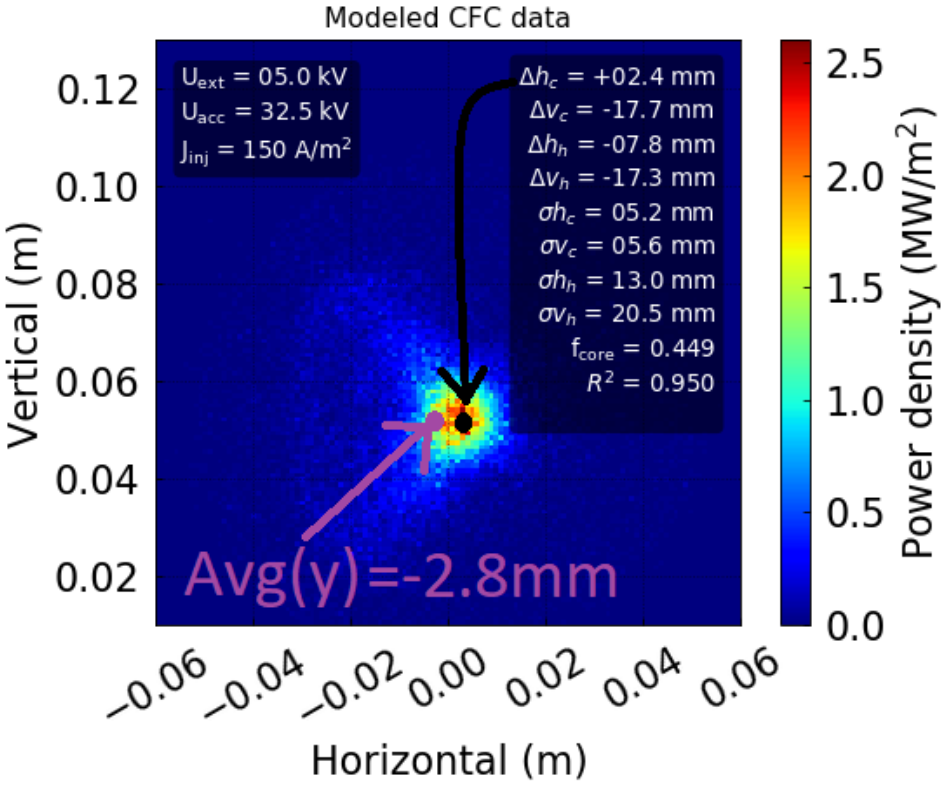

Figure 4.29: Power density plot, aperture 53, $U_{ext} = 5\,\mathrm{kV}$, $U_{acc} = 32.5\,\mathrm{kV}$, $J_{inj} = 150\,\mathrm{A\,m^{-2}}$, $I_{PG} = 2.2\,\mathrm{kA}$. Both $\bar{y}$ (Avg(y), in purple) and y_{core} (black arrow) are outlined.

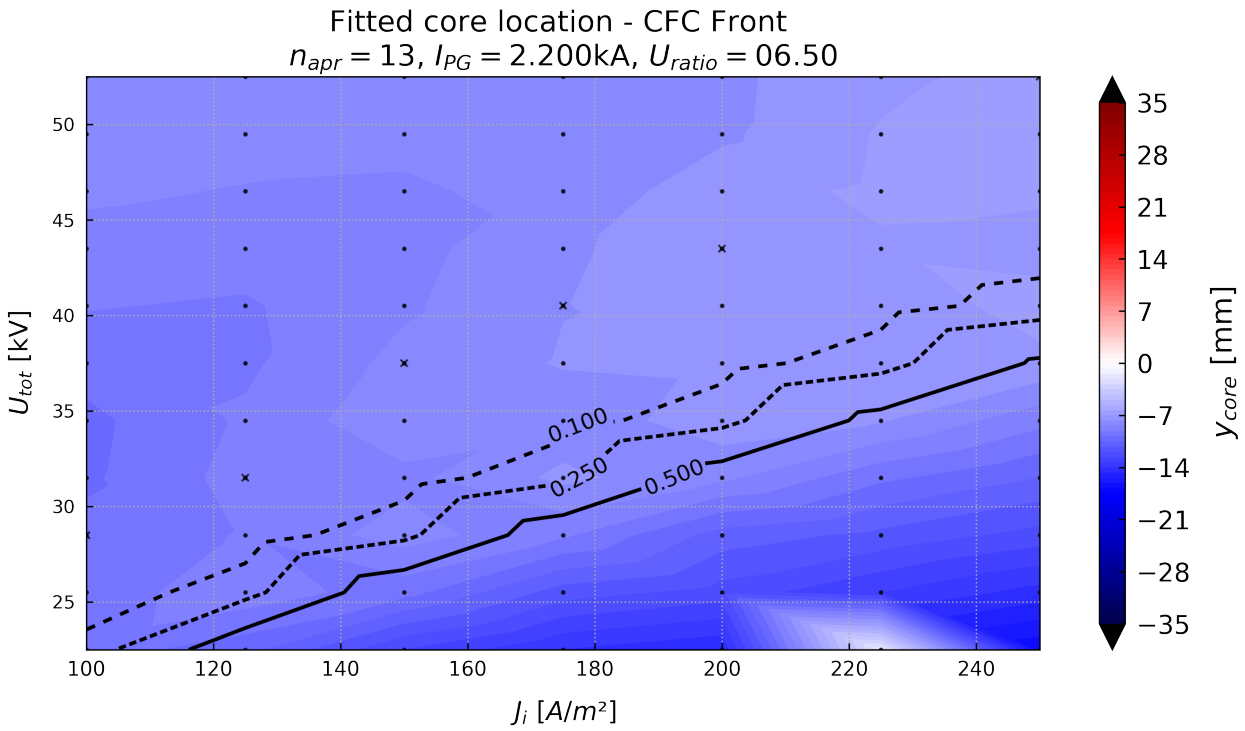

Figure 4.30: Fitted core horizontal position for aperture 13, as a function of both J_{inj} and $U_{tot} = U_{acc} + U_{ext}$, $I_{PG} = 2.2\,\text{kA}$, $U_{ratio} = U_{acc}/U_{ext} = 6.5$.

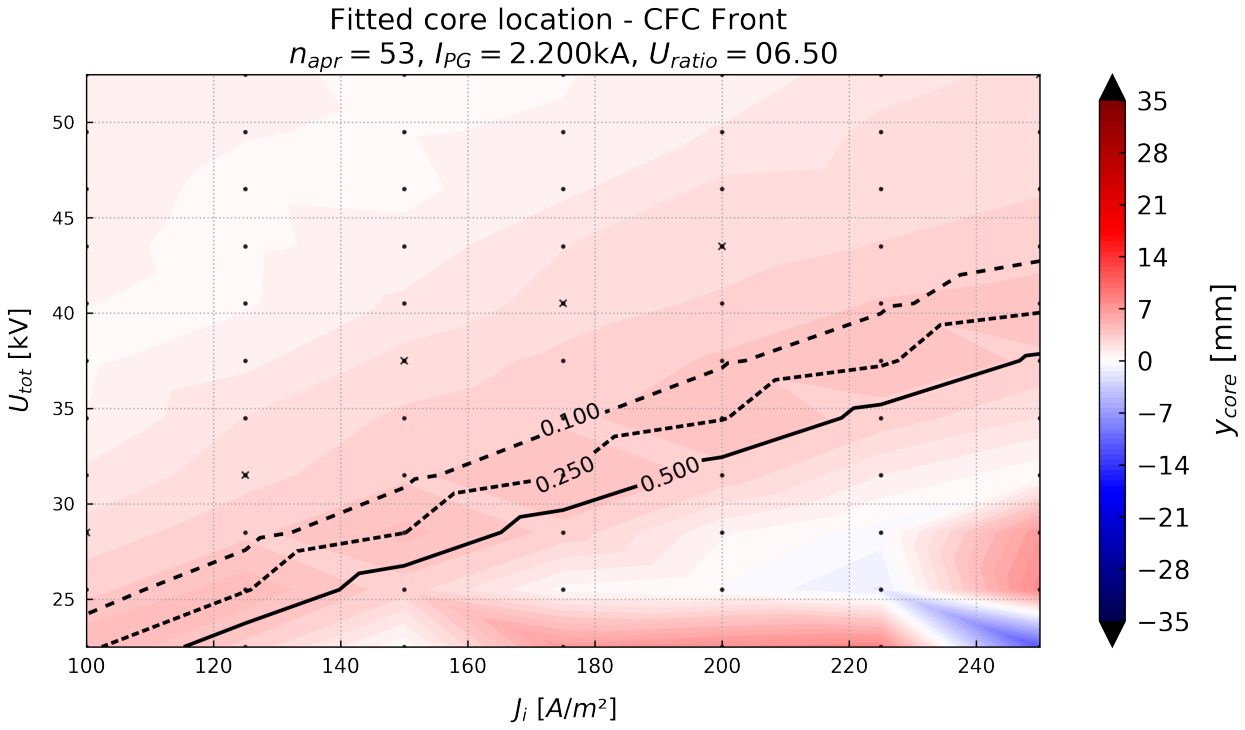

Figure 4.31: Fitted core horizontal position for aperture 53, as a function of both J_{inj} and $U_{tot} = U_{acc} + U_{ext}$, $I_{PG} = 2.2\,\text{kA}$, $U_{ratio} = U_{acc}/U_{ext} = 6.5$.

4.3.4. Conclusions

In conclusion, IBSimu simulations show that:

- for fixed U_{tot} in the divergence optimum, a shift of $\approx$ 13 mm to the left is expected to be observed for aperture 13, but not for aperture 53.
- For fixed voltage ratio, changing U_{tot} in experimental range should not influence the beamlet position for aperture 53, while inducing a shift of $\lesssim$ 10 mm for aperture 13.
- Changing P/P_0 should not impact on the fit results at fixed U_{tot}, while for fixed voltage ratio should impact visibly only aperture 13 ($\approx$ 15 mm), and much less significantly aperture 53 ($\approx$ 5 mm).
- Some irregularities due to the fitting procedure are to be expected.

Therefore, the ADCMs compensation is expected to effectively correct the zig-zag deflection for the optimum voltage ratio, and not to be dependent on U_{tot}.

4.4. BES synthetic data

Using the previous analysis as a basis, it is possible to select a parameter set whose normalised perveance belongs in the interval $[0.26, 0.28]$. For these parameter combinations, full-grid simulations are run with IBSimu in order to derive the necessary electric fields, which are then given as input to BBCNI, in order to produce simulations also for the BES data.

In particular, two scans at constant normalised perveance are selected: one in the total voltage U_{tot} at a constant $U_{ratio} = 6.5$, the other in U_{ratio} at a constant $U_{tot} = 37.5$ kV. The parameters selected are reported respectively in Tables 4.2, 4.3.

U_{ext} [kV]	U_{acc} [kV]	U_{tot} [kV]	U_{ratio}	J_{inj} [A m^{-2}]	P/P_0
3.8	24.7	28.5	6.5	100	0.264
4.2	27.3	31.5	6.5	125	0.283
5	32.5	37.5	6.5	150	0.264
5.4	35.1	40.5	6.5	175	0.274
5.8	37.7	43.5	6.5	200	0.281

Table 4.2: Parameters for the U_{tot} scan at a constant $U_{ratio} = 6.5$ and normalised perveance.

U_{ext} [kV]	U_{acc} [kV]	U_{tot} [kV]	U_{ratio}	J_{inj} [A m^{-2}]	P/P_0
3.64	33.86	37.5	9.3	100	0.280
4.42	33.08	37.5	7.4	125	0.264
4.86	32.64	37.5	6.7	150	0.274
5	32.5	37.5	6.5	150	0.264
5.36	32.14	37.5	6.0	175	0.277
5.9	31.6	37.5	5.4	200	0.275
6.5	31	37.5	4.8	225	0.268

Table 4.3: Parameters for the U_{ratio} scan at a constant $U_{tot} = 37.5\,\text{kV}$ and normalised perveance.

For each spectra acquired, both the unshifted and the Doppler-shifted peak are fitted peak with a gaussian function, which is exploited to estimate the peak position and its width, from which it is then possible to derive the divergence (chapter 2.2.1).

Given the positions of the optical heads, the detectors will collect different amounts of light, therefore, the analysis procedure will not plot any spectra if the intensity registered is not enough. In particular, this will often happen for BES01-03, which is at a vertical position where the rows are masked and therefore is often not sufficiently illuminated. The analysis routine proceeds to compute the estimated beam divergence with the formula 2.8, taking into account various width broadening effects.

Finally, a plot similar to the one in Figure 4.32 is generated, in which 3 graphs are displayed:

- on the left, a plot of all the acquired spectra per line of sight. The blue lines represents BES01, the orange ones BES02. The lines of sight are numbered from the bottom to the top.

- on the top-right, the estimated divergence is plotted as a function of the detector's position. Since the LOS are labelled from bottom to the top in ascending order, the points in this graph will represent from left to right the various LOS, in orange for BES02 and in blue for BES01.

- in the bottom right corner, the area of the Doppler peak is reported, again as a function of the position of the LOS.

In particular, Figure 4.32 is the result of the BES analysis for $U_{ext} = 5\,\text{kV}$, $U_{acc} = 32.5\,\text{kV}$, $J_{inj} = 150\,\text{A m}^{-2}$, $I_{PG} = 2.2\,\text{kA}$, but it has some general features that are present in all the simulated spectra.

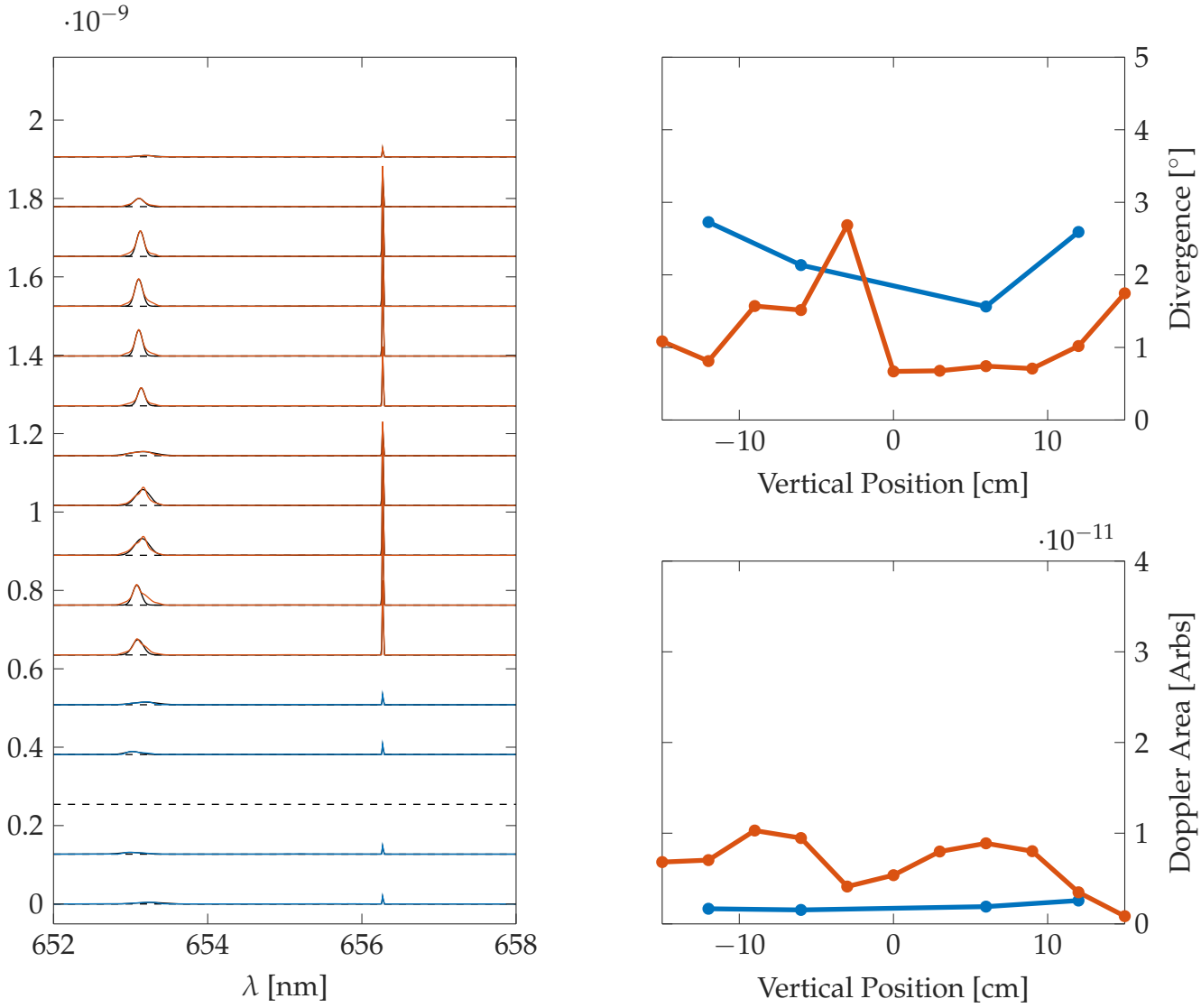

Figure 4.32: BES spectra per line of sight, divergence and Doppler peak area, simulated with BBCNI, for $U_{ext} = 5\,\text{kV}$, $U_{acc} = 32.5\,\text{kV}$, $J_{inj} = 150\,\text{A}\,\text{m}^{-2}$, $I_{PG} = 2.2\,\text{kA}$.

For instance, it clearly shows the "perfectness" of the unshifted peak, that indeed has the a Dirac delta-like shape due to the fact that the usual systematic errors created by the acquisition system are of course not present in the simulation. Besides, the slow particles which would impact on the width of the distribution are not represented because of they are below the resolution of the spectrum binning. On the other hand, an issue with the telescope acceptance file for BES01 returns values which are much lower in intensity with respect to BES02, which is an effect that will not be observed in the experimental results. Due to these facts, the Doppler area graph will generally show very low results for BES02, and practically null ones for BES01, if the graphs are scaled to show the full height of the unshifted line.

Furthermore, another common feature of the plots is the behaviour of the divergence. In fact, one can notice that BES02 LOS positioned at a vertical position < 0cm

will generally show a growing tendency and values of the divergence higher than 1° ($\approx$ 17 mrad). After BES02-05 (vertical position $= -3$cm), a significant drop is recorded and then the divergence behaviour stabilise around 0.8° ($\approx$ 13 mrad).

Observing the spectra, it is immediately clear why this happens: in the lower part of the graph, the LOS acquires data from the uncompensated beamlets, and therefore, observing the shape of the Doppler peaks, it can be noticed that often it is not gaussian and presents more than one maximum. This is because the different rows, which have different trajectories, provide contributions with a slightly different Doppler shifted peak, which are nevertheless detected by the same optic head. On the contrary, the double peak structure is not present in the spectra acquired from the compensated half of the grid, in which the gaussian fit provides better results and hence lower values for the divergence: as a matter of fact, correcting the zig-zag deflection improves the estimate of the divergence and helps in evaluating it correctly.

Both the uncompensated and compensated halves show that the gaussian fit is just an approximation of the real photon distribution: large wings are more or less always present in all the Doppler shifted peaks, with a slight unbalance towards the right part of the distribution. This will be also observed experimentally and could be due to the fact that velocity distribution is not perfectly Maxwellian, as it is assumed in the BES analysis (chapter 2, eq. (2.13)): in principle, if the signal to noise ratio is high enough, one could fit a double Gaussian to the spectra, outlining the halo and the core component of the distribution.

4.4.1. U_{tot} scan, $U_{ratio} = 6.5$

After having outlined the main common features of all the synthetic BES data, it is interesting to quantify the most important traits of the analysed spectra. In particular, the focus will be on the divergence and the difference in position between the Doppler shifted peak and the unshifted one $\Delta\lambda$.

Concerning the latter, the results are presented in Figure 4.33. In this picture, $\Delta\lambda$ is plotted against the total voltage for 4 different lines of sight. Two of them (BES02-08, BES01-04) collect light coming mainly from the compensated half of the grid, while BES01-01 and BES02-03 detect signals from rows in the lower half. It is worth noticing how the distance between the unshifted and the Doppler shifted peak increase with increasing total voltage, due to the fact that (as seen in formula (2.11)) the shift is linearly dependent on the particle's velocity, which depends on the acceleration voltage. This graph shows that the simulations correctly depict the physics of the Doppler shift.

Another interesting feature is that, while BES02 data are very close to each other, BES01 lines are separated more evidently (by about 0.2 nm). This could be due to the fact that BES01 optic heads are closer to the grids and hence detect better

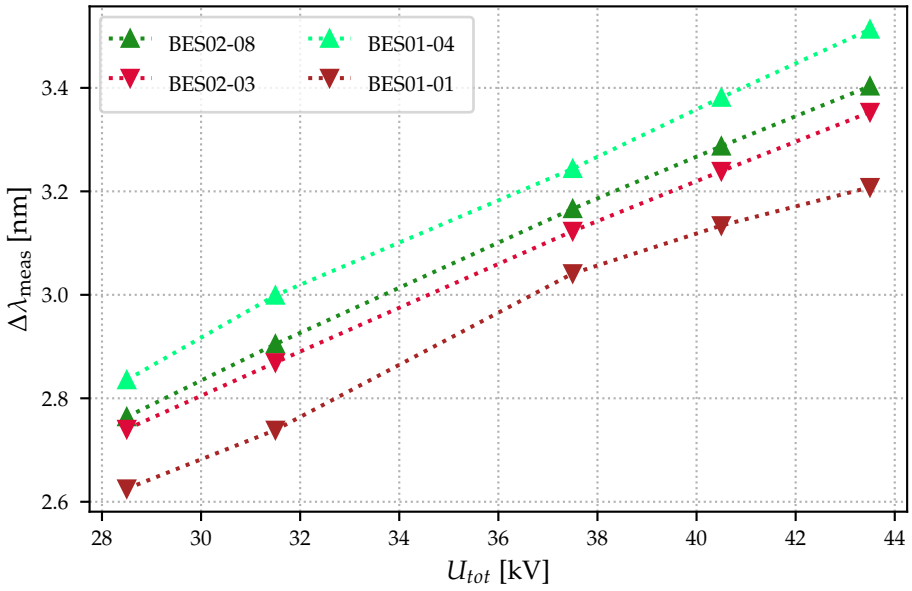

Figure 4.33: Difference between the Doppler peak position and the unshifted one $\Delta\lambda$ vs the total voltage U_{tot} for BBCNI BES synthetic data. Data represented with a triangle facing up refers to the upper part of the grid, the ones facing down are instead on the lower half.

single row contributions. Given that the difference between the un-shifted and the Doppler shifted peak depends only on the position of the Doppler peak (since λ_0 is a constant), this discrepancy can be due only to differences between the lines of sight and therefore could be a sign for the zig-zag effect presence in the lower part of the grid.

Concerning the divergence, given the issue in the analysis script for BES01, only BES02 will be examined. The comparison between BES02-08 (compensated) and BES02-03 (uncompensated) is reported in Figure 4.34. It is immediately clear that BES02-08 detects lower divergence values, that are approximately constant around $0.8° \approx 14$mrad for each value of U_{tot}. Conversely, the uncompensated divergence is generally twice the compensated one and show a moderate descent with higher values of U_{tot}. Thus, one could expect that the fitting procedure will give better results and hence lower values of the divergence for the region in which the ADCMs act.

4.4.2. U_{ratio} scan, $U_{tot} = 37.5\,\text{kV}$

Also in this case the main quantity studied is the divergence, for BES02-03 and BES02-08. Figure 4.35 represents them as a function of the voltage ratio $U_{ratio} = U_{acc}/U_{ext}$. Observing the graph, it can be noticed that for ratios $U_{ratio} < 7.4$, the compensated beamlets have lower divergence, with a minimum value for $U_{ratio} = 6$, with respect to the uncompensated ones, which also show a more fluctuating behaviour. For

bigger ratios, instead, the divergence values of both the datasets steeply increase: this happens because the situation is similar to the one reported in Figure 4.23, in which the electrostatic lenses do not focus the beamlets optimally.

It is worth noticing that the minimum of the divergence is different from the one computed with IBSimu CFC simulations ($U_{ratio} = 5.2$ [28]) and it will be different also from the experimental data. This effect might be related to how the divergence is computed and how the average of eq. (2.8) is derived by each simulation code and more specifically by the systematic contributions.

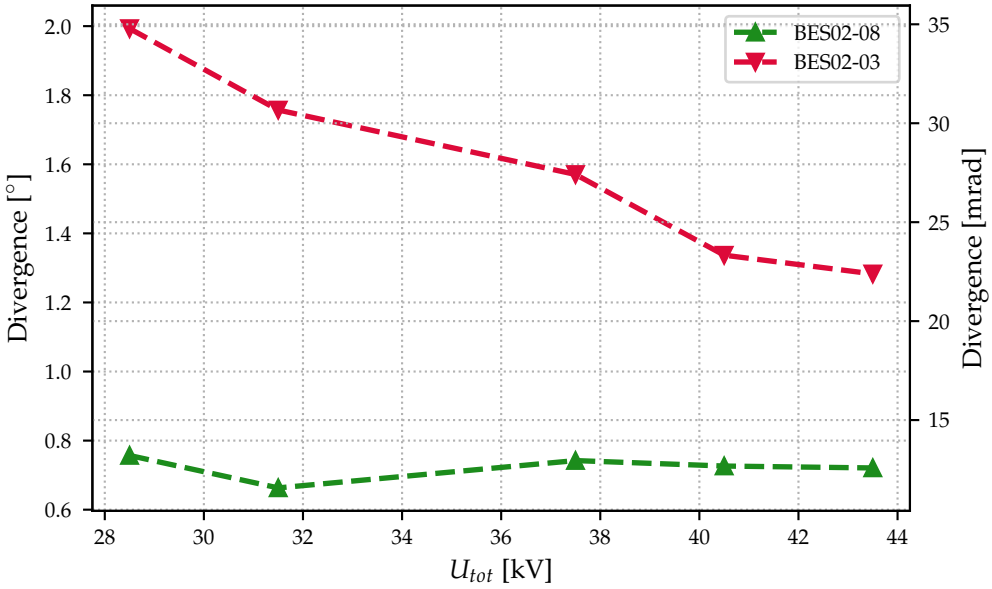

Figure 4.34: Divergence in both mrad and ° as a function of U_{tot}, for BES02-08 and BES02-03.

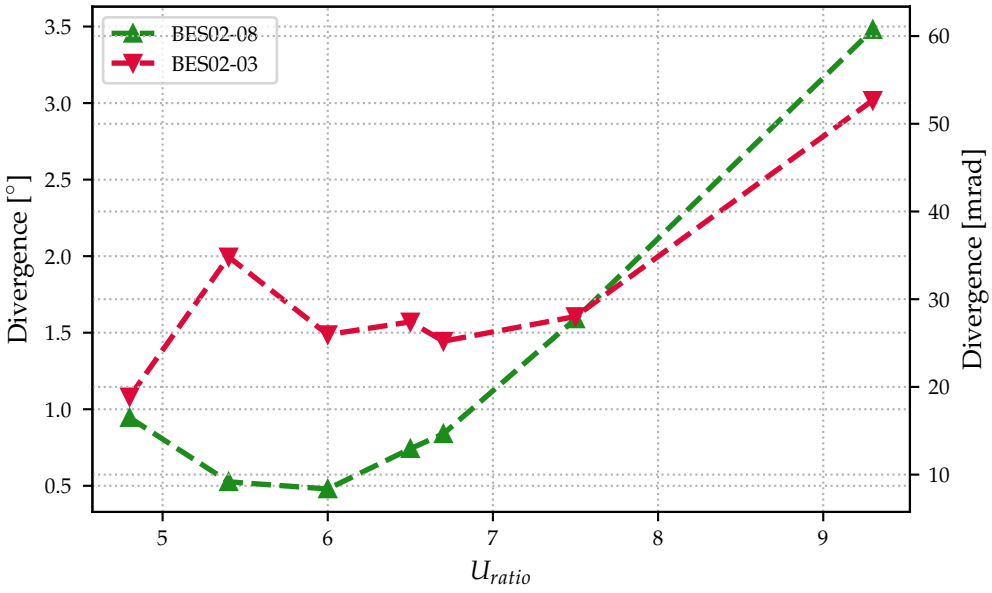

Figure 4.35: Divergence in both mrad and ° as a function of U_{ratio}, for BES02-08 and BES02-03.

4.4.3. Conclusions

In conclusion, BBCNI simulations show that:

- a clear difference of approximately a factor 2 should be observed between the divergence of the compensated half and the uncompensated half, when keeping the voltage ratio in its optimum ≈ 6.
- for fixed U_{tot}, the divergence of the compensated half of the grid should have a minimum between $U_{ratio} \in [5;7]$, in which it is significantly different from the uncompensated divergence.

The most exciting phrase to hear in science, the one that heralds new discoveries, is not "Eureka!" but "That's funny..."

Isaac Asimov

5 Experimental activity

After depicting the main theoretical aspects and the preliminary simulations, the experimental campaign results can be presented. The general plan of the performed scans and measurements can be found in 5.1, followed by a presentation of data and main results in 5.2.1 for the CFC, in 5.2.2 for the BES.

5.1. Planning and general overview

The experimental campaign has two main goals. First of all, investigating the zig-zag deflection compensation applied by the addition of the ADCMs. Secondly, determine the impact of the magnets on the measured beamlet divergence. The first issue can be studied by analysing the CFC recorded images with the two-halves masking. The second one, instead, can be examined with the BES, but the masking strategy needs to be changed to use the CFC, by isolating a single aperture on the top-half.

In this work, only the two-halves masking data are presented and analysed, but the experimental campaign also planned changing the masking to have a complete overview of the collected data. Several scans are planned, focusing on the following parameters:

- extraction voltage U_{ext};
- acceleration voltage U_{acc};
- total voltage U_{tot};
- voltage ratio U_{ratio};
- plasma grid current I_{PG};
- bias current I_{bias};
- radio-frequency power P_{RF};
- filling pressure p_{fill}.

Experimental scans can be one or two dimensional, depending on the number of parameters varied during the same scan. Generally, a scan consists of a certain number of data points, for each of which 2 shots are taken: the first one is a short beam pulse (beam-on time 1 s), in which the CFC footprints are collected; the second one is longer (4.5 s), with the CFC tile removed from the beam path, used to collect enough light to have sufficient signal-to-noise ratio for the BES. Each shot is identified with an ID number in increasing order.

If not differently specified, the standard values of the experimental parameters for each scan are the ones reported in Table 5.1.

In Table 5.2, instead, the full experimental plan is displayed, for the two-halves masking. Concerning the single-beamlet masking, the same plan is followed after changing which apertures are open. For each scheduled scan, the following information is indicated:

- the shot ID numbers;
- the scan type (1D or 2D);
- the parameter(s) scanned;
- the range in which the parameter(s) is (are) scanned;
- the step of which parameter(s) is (are) changed;
- special conditions: parameter(s) kept constant during the scan, filter field orientation.

5.2. Data analysis and results

In this section, data and results are presented. Concerning the CFC, the data is represented via the processed IR camera pictures: after the perspective correction, the rates of change of temperature of the tile, calculated at a time of 0.5 s after the start of the beam, are plotted as a function of the position. A qualitative analysis of the main dependencies is provided, especially focusing on the resolution of single beamlets and on the qualitative evaluation of the compensation effect of the ADCMs. Concerning the BES, instead, a more quantitative analysis is performed, in which the divergence and/or the magnitude of the Doppler shift is evaluated as a function of the varied parameter(s).

U_{ext}	U_{acc}	U_{tot}	U_{ratio}	I_{PG}	I_{bias}	P_{RF}	p_{fill}
5.0 kV	32.5 kV	37.5 kV	6.5	2.2 kA	5 A	60 kW	0.6 Pa

Table 5.1: Standard experimental scan parameters.

Shot numbers	Type	Parameter	Range	Step	Condition(s)
$132806 - 132825$	1D	U_{acc}	$[20;40]$kV	2.5 kV	Standard FF
$132826 - 132856$	1D	P_{RF}	$[20;80]$kW	5 kW	Standard FF
$132871 - 132941$	2D	U_{ext} P_{RF}	$[3;6]$kV $[25;80]$kW	0.5 kV 5 kW	$U_{tot} = 37.5$ kV, Standard FF
$132960 - 133017$	2D	U_{ext} P_{RF}	$[4.5;5.5]$kV $[35;80]$kW	0.5 kV 5 kW	$U_{ratio} = 6.5$, Standard FF
$133021 - 133030$	1D	I_{bias}	$[1;16]$A	4 A*	$P/P_0 \approx 0.32$, Standard FF
$133045 - 133060$	1D	p_{fill}	$[0.3;0.7]$Pa	≈ 0.05 Pa	$P/P_0 \approx 0.31$, $I_{PG} = 2.75$ kA, Standard FF
$133064 - 133123$	2D	I_{PG} P_{RF}	$[1.25;3.00]$kA $[40;80]$kW	0.25 kA 10 kW	Standard FF
$133152 - 133168$	1D	p_{fill}	$[0.3;0.7]$Pa	≈ 0.05 Pa	$P/P_0 \approx 0.31$, $I_{PG} = 2.75$ kA, Reversed FF
$133172 - 133185$	1D	P_{RF}	$[20;80]$kW	10 kW	Reversed FF
$133186 - 133200$	1D	I_{bias}	$[1;16]$A	4 A*	$P/P_0 \approx 0.32$, Reversed FF
$133208 - 133256$	2D	I_{PG} P_{RF}	$[1.25;3.00]$kA $[40;80]$kW	0.25 kA 10 kW	Reversed FF

Table 5.2: Full plan of all the experimental scans for the two-halves masking. * : the parameter range is not equally sampled, the first 3 points are $1, 3, 8$A.

5.2.1. CFC

U_{acc} *1D scan*

In these experimental conditions, single beamlets could be resolved and the effect of the ADCMs can be seen only in the datasets close to the optimum U_{ratio}: in fact, this happens only for values of $U_{acc} = 30, 32.5, 35$ kV, which correspond respectively to values of voltage ratios of $U_{ratio} = 6, 6.5, 7$ and of the normalised perveance of $0.3305, 0.3256, 0.3222$. In these conditions, one can definitely notice the zig-zag effect shifting the beamlets by ≈ 20 mm on the bottom half, while the top half is compensated and the beamlets are correctly arranged in a rectangle shape (Figure 5.1, shot ID 132813). In the other plots, given the over or under-perveant regime,

the two halves of the beam can still be seen, but the effect of the ADCM is harder to determine, as the beam footprints look like uniform stains, in which it is impossible to resolve the single beamlets or to evaluate the zig-zag compensation (Figure 5.2, shot ID 132821).

This behaviour is coherent with the one expected from the simulation: the shots in which the beamlets are detectable coincide with the zero-shift area in both fig. 4.12 (fitted core position vs. J_{inj} vs. U_{acc}) and fig. 4.22 (fitted core position vs. J_{inj} vs. U_{ratio}) as the voltage ratios are respectively $U_{ratio} = 6, 6.5, 7$. The perveance values, instead, do not correspond with the simulations, and are generally higher: in the design report [28] and in the simulations of chapter 4, the optimum correction effect happens for perveance values in the range $[0.25; 0.28]$, while in the experiment the same condition is reached for $P/P_0 \in [0.31; 0.33]$. The real reason for this effect is unknown, but a possible explanation could be related to an underestimation of the extracted current.

Moreover, an unexpected feature showed up: it seems that, in addition to the zig-zag deflection, a non-uniform vertical beamlet displacement is also present. This phenomenon was not predicted by the simulations, but was also observed experimentally in the QST campaign [17]. This effect is clearly visible in the perveance optimum and will be referred as the **hanging rows** from this point on.

Further analysis, performed after the data taking sessions, proved that the hanging rows effect was due to a technical issue: in fact, the electrical contact between the PG frame and PG insert was not proper, resulting in a different filter field geometry. Therefore, the inconsistency between experiment and simulations is explained by the difference between the magnetic fields [31].

P_{RF} *1D scan*

Also in this scan, the compensation of the ADCM acts as expected, correcting the zig-zag deflection in the top-half, given that the voltages were set to be in the design optimum, as it can be seen in Figure 5.3.

Single beamlets, however, can be resolved clearly only for $P_{RF} > 45$: it can be noticed that for lower powers not only the CFC tiles look very smeared, but the normally present intensity asymmetry between the top and bottom half of the grid, caused by the filter field drift, is enhanced (see Figure 5.4). This is a sign of a plasma asymmetry, induced by the magnetic field. It can be said that lower P_{RF} values probably are not enough to provide uniform power, generating this phenomenon. Besides, the hanging rows are still present at all P_{RF} values, meaning that this effect is not power dependent.

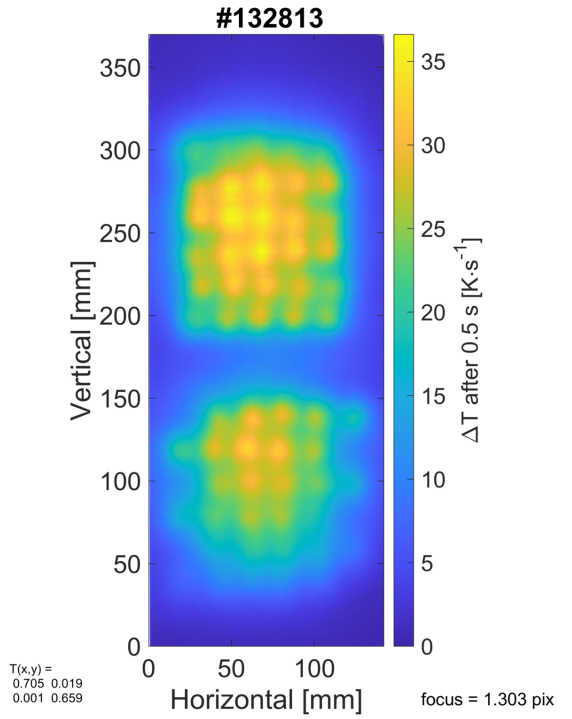

Figure 5.1: CFC tile: $U_{acc} = 32.5\,\mathrm{kV}$, $P/P_0 = 0.3256$ and standard parameters.

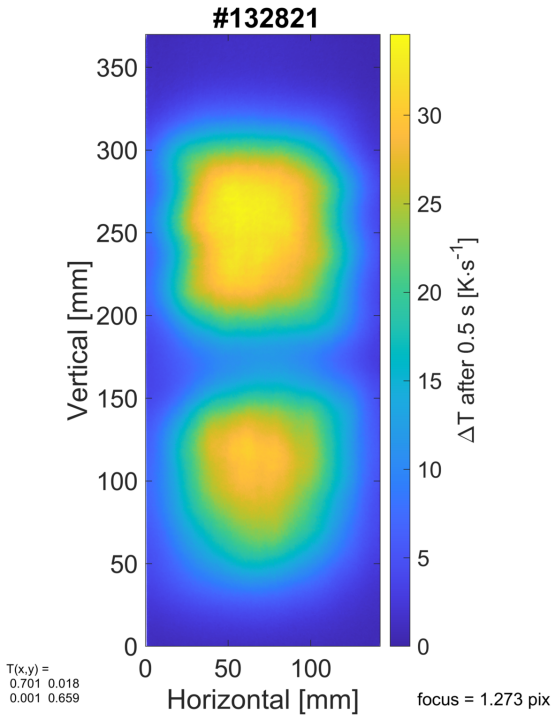

Figure 5.2: CFC tile: $U_{acc} = 22.5\,\mathrm{kV}$, $P/P_0 = 0.3053$ and standard parameters.

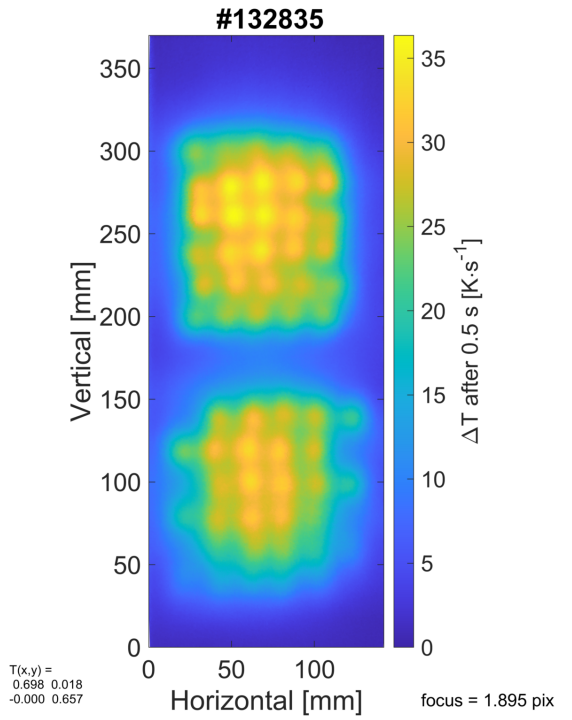

Figure 5.3: CFC tile: $P_{RF} = 80\,\mathrm{kW}$, $P/P_0 = 0.3593$ and standard parameters.

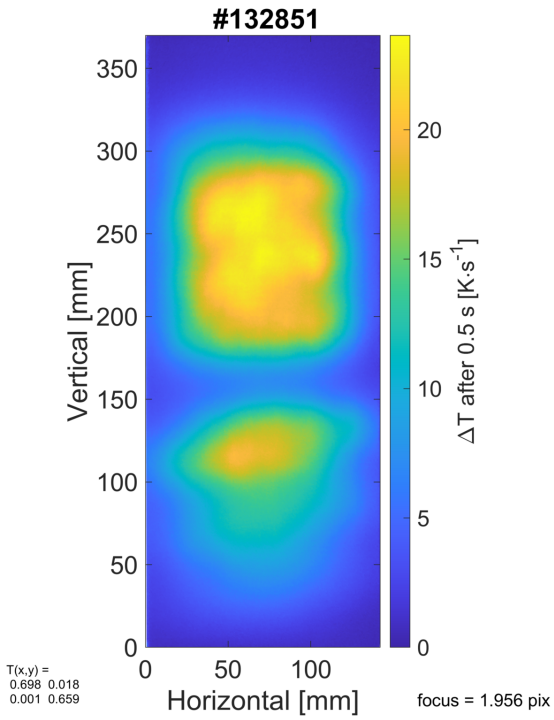

Figure 5.4: CFC tile: $P_{RF} = 25\,\mathrm{kW}$, $P/P_0 = 0.1563$ and standard parameters.

$U_{ext} - P_{RF}$ 2D scan at constant total voltage

This experimental scan is correspondent to the U_{ratio} scan analysed beforehand in chapter 4.3.2, with total voltage kept constant at 37.5 kV. The relevant aspect of this 2D scan is that changing the voltage ratio impacts on the compensation also on the top part: if the parameter exits the optimum ratio for which the ADCMs are designed, the compensation effect is not as good as it should be, meaning that the beamlet centres are not vertically aligned (hence not respecting the misalignment requirements of Table 1.2).

An example of this can be seen by comparing Figure 5.5 ($U_{ext} = 6\,\text{kV}$, $U_{acc} = 31.5\,\text{kV}$, $U_{ratio} = 5.25$, $P/P_0 = 0.2202$) and 5.6 ($U_{ext} = 4.5\,\text{kV}$, $U_{acc} = 33\,\text{kV}$, $U_{ratio} = 7.33$, $P/P_0 = 0.3701$). In the figure on the left, despite the under-perveance which makes the single beamlets not fully resolved, it can still be seen that they are arranged in a regular rectangular shape in the upper half of the CFC, definitely different from the lowest half, in which the zig-zag deflection can be observed. On the right, conversely, the beamlets can be resolved neatly, but the ADCM correction on the top half is not so effective and a slight zig-zag deflection of about $\approx 5 - 7$mm can be observed. The simulations of Figure 4.20 are consistent with this observed shift: in the rightmost part of the graph, i.e. for the highest values of P/P_0, the average particle position is approximately of 7 mm for the observed ratio of 6.5. It can be concluded that the deflection correction is dependent on the voltage ratio significantly: this fact was also observed from the simulations of section 4.3.2. Finally, also in this case, similarly to what just stated for the P_{RF} scan, at lower powers the tile illumination is significantly asymmetric.

$U_{ext} - P_{RF}$ 2D scan at constant voltage ratio

This experimental scan is correspondent to the U_{tot} scan analysed beforehand in chapter 4.3.3, with voltage ratio fixed to 6.5. It can be noticed that the compensation of the ADCMs is always present, given that the ratio chosen is located in the design optimum. The main difference between different CFC tiles is that at higher voltages the single beamlet resolution slightly increases, as it can be seen comparing Figure 5.7 ($U_{ext} = 3\,\text{kV}$, $U_{acc} = 19.5\,\text{kV}$, $U_{tot} = 22.5\,\text{kV}$, $P/P_0 = 0.3148$) and 5.8 ($U_{ext} = 5.5\,\text{kV}$, $U_{acc} = 35.75\,\text{kV}$, $U_{tot} = 41.25\,\text{kV}$, $P/P_0 = 0.3352$).

This is coherent with the simulations, that showed that the deflection correction should be only slightly dependent on the total voltage (Figures 4.26, 4.28), and with the theory. In fact, keeping the same voltage ratio should keep the shape of the electrostatic lens constant. If also the meniscus shape, regulated by U_{ext} and the plasma parameters (p_{fill}, P_{RF}), is the same, then beams will have the same optics: this can also be seen by comparing the normalised perveances, as in Table 5.3.

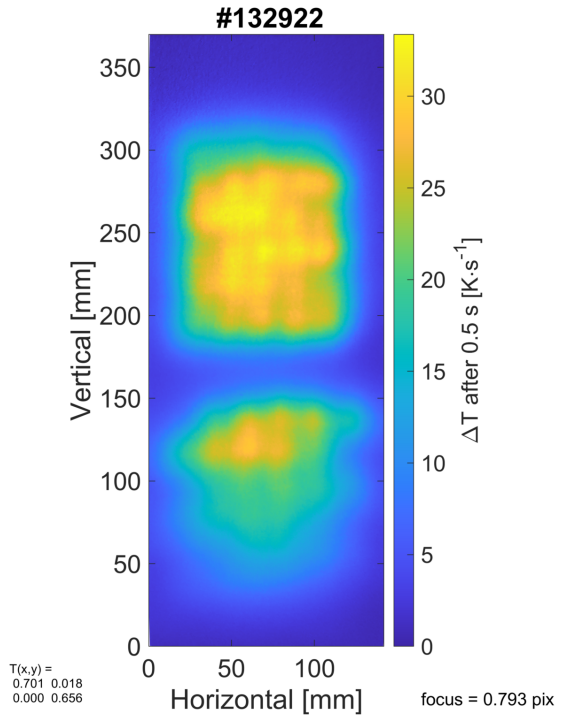

Figure 5.5: CFC tile: $P_{RF} = 80\,\text{kW}$, $P/P_0 = 0.3593$ and standard parameters.

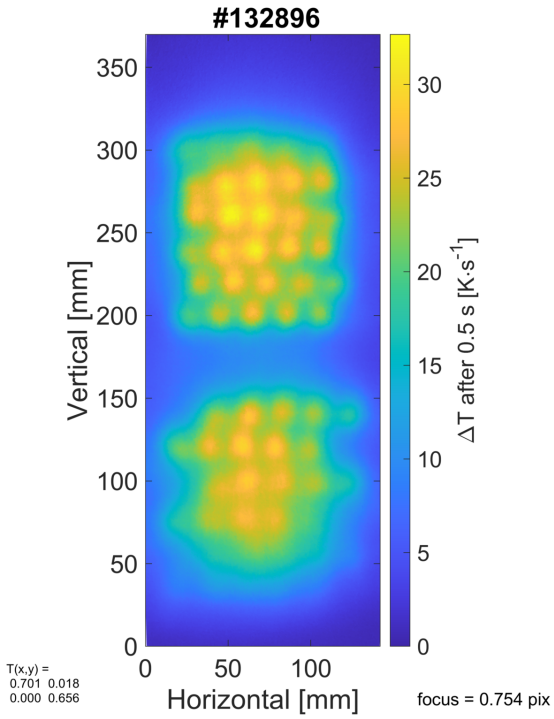

Figure 5.6: CFC tile: $P_{RF} = 25\,\text{kW}$, $P/P_0 = 0.1563$ and standard parameters.

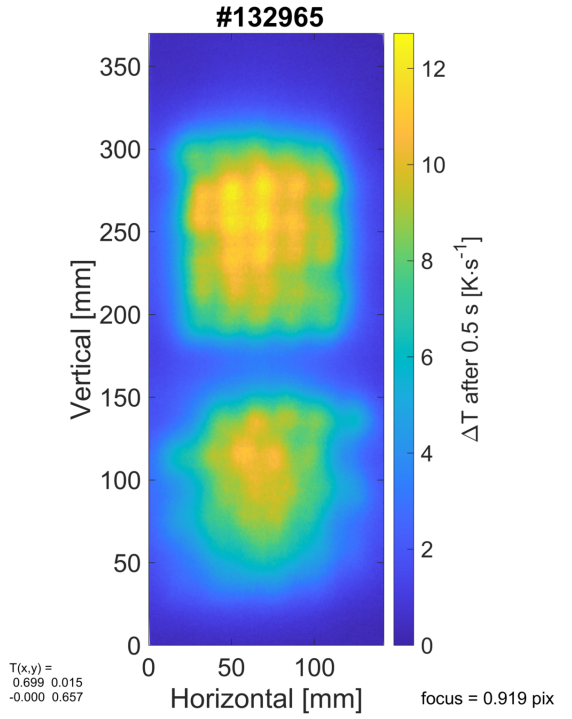

Figure 5.7: CFC tile: $U_{tot} = 22.50\,\text{kV}$, $P_{RF} = 35\,\text{kW}$, $P/P_0 = 0.3148$ and standard parameters.

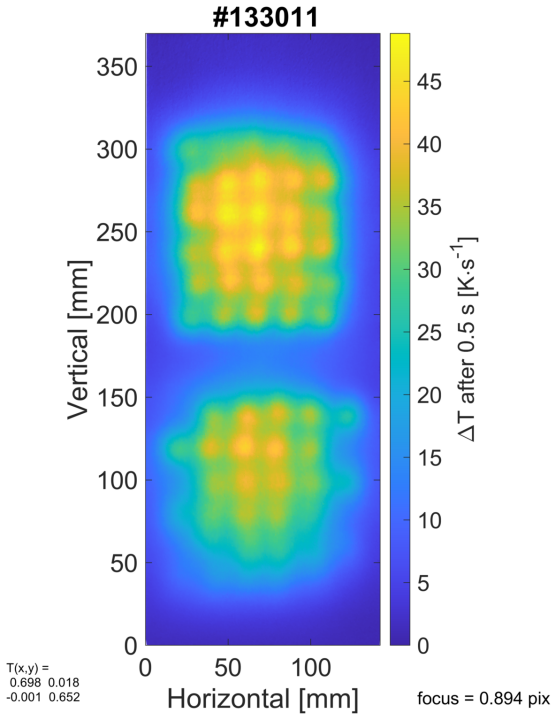

Figure 5.8: CFC tile: $U_{tot} = 41.25\,\text{kV}$, $P_{RF} = 70\,\text{kW}$, $P/P_0 = 0.3352$ and standard parameters.

#	U_{ext}[kV]	U_{acc}[kV]	U_{ratio}	U_{tot}[kV]	P_{RF}[kW]	P/P_0
132965	3	19.50	6.5	22.50	35	0.3148
132971	3.5	22.75	6.5	26.25	45	0.3273
132982	4	26.00	6.5	30.00	45	0.3179
132990	4.5	29.25	6.5	33.75	55	0.3302
133005	5	32.5	6.5	37.50	60	0.3282
133011	5.5	35.75	6.5	41.25	70	0.3352

Table 5.3: Comparison between experimental shots at the same $U_{ratio} = 6.5$ with different total voltages U_{tot}.

I_{bias} *1D scan at constant perveance*

The bias current seems to have little influence on the ADCM compensation, however, if it is increased too much the resolution of the beamlets is impacted, as shown in Figures 5.9 ($I_{bias} = 1$ A), 5.10 ($I_{bias} = 16$ A). This fact is surprising, since the data were take by keeping P/P_0 constant around 0.32 (close to the optimum): the expected outcome would be to have similar optics in all the pictures, while experimentally it is observed that the divergence seems to increase with I_{bias}. However, considering that by varying I_{bias} the potential upstream of the PG is changed, this tendency might be due to a change in the velocity distribution of the ions at the meniscus, which reasonably would impact on the beamlet divergence.

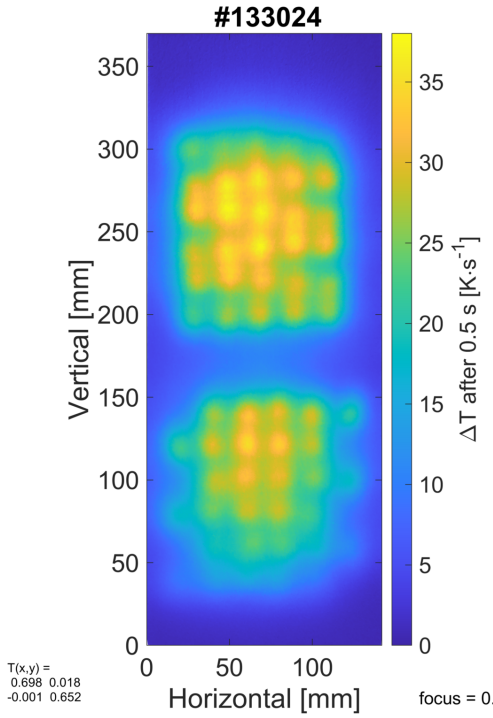

Figure 5.9: CFC tile: $I_{bias} = 1$ A, $P_{RF} = 53$ kW, $P/P_0 = 0.3201$ and standard parameters.

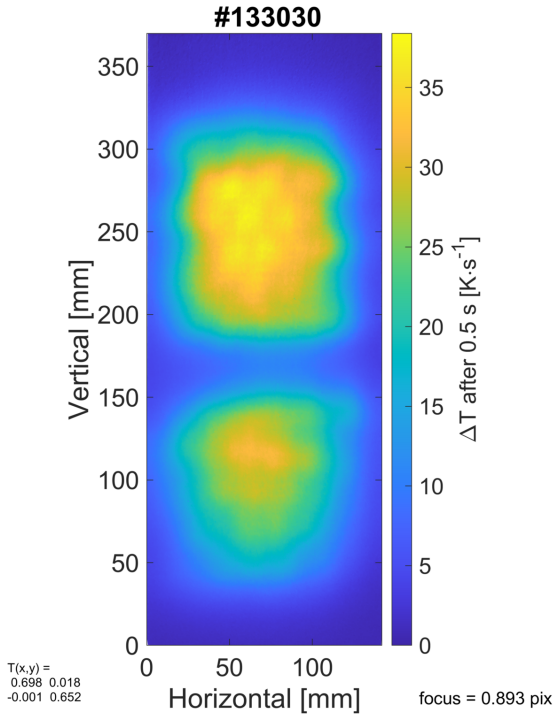

Figure 5.10: CFC tile: $I_{bias} = 16$ A, $P_{RF} = 75$ kW, $P/P_0 = 0.3223$ and standard parameters.

p_{fill} *1D scan at constant perveance*

The pressure, as expected, does not influence on the ADCM effect, but it has an impact on the beamlet detection: at lower pressure the beamlets cannot be resolved spatially. This is also the reason why the standard p_{fill} value is chosen to be 0.6 Pa and not the ITER-required 0.3 Pa, as it is clearly displayed by comparing Figures 5.11 ($p_{fill} = 0.307$ Pa) and 5.12 ($p_{fill} = 0.652$ Pa).

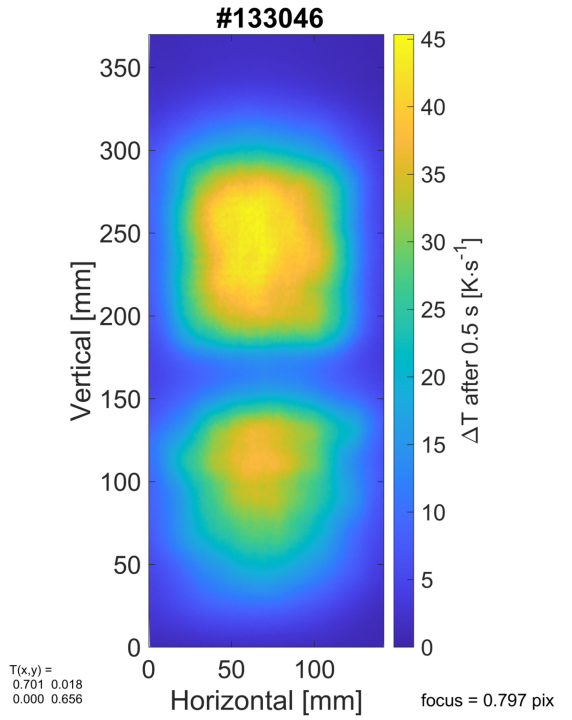

Figure 5.11: CFC tile: $p_{fill} = 0.307$ Pa, $P_{RF} = 80$ kW, $I_{PG} = 2.75$ kA, $P/P_0 = 0.3279$ and standard parameters.

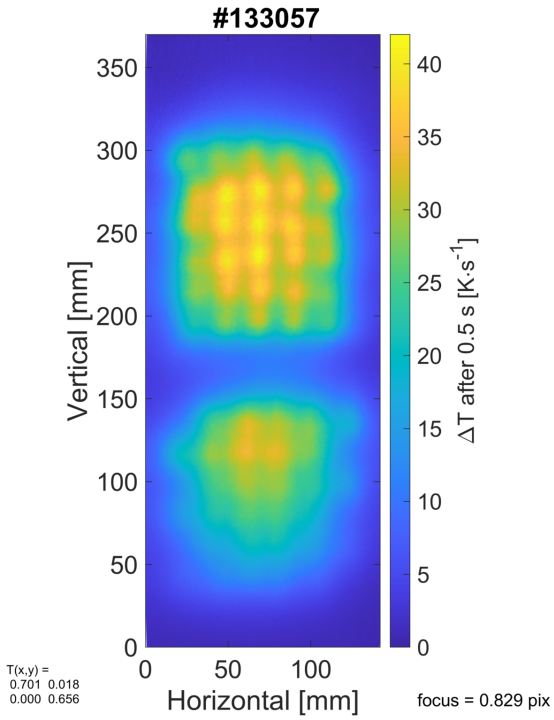

Figure 5.12: CFC tile: $p_{fill} = 0.652$ Pa, $P_{RF} = 80$ kW, $I_{PG} = 2.75$ kA, $P/P_0 = 0.3109$ and standard parameters.

$I_{PG} - P_{RF}$ *2D scan*

The beamlet resolution is not affected by the plasma grid current, while it is by the RF power, which changes the normalised perveance values. CFC shots collected in the same perveance regime will produce pictures with very similar feature, both in terms of the ADCM compensation and of beamlet resolution, as expected.

Yet, increasing I_{PG} produces a shift downwards of the beamlets: this can be seen by comparing their position in Figure 5.13 ($I_{PG} = 3$ kA) and 5.14 ($I_{PG} = 1.5$ kA). Since the plasma grid current generates the magnetic filter field, this effect is completely understandable: the bigger the current, the bigger the magnitude of the horizontal magnetic field, which hence deflects vertically and more particles.

The ADCM compensation, nevertheless, is not influenced by these changes, while in the uncompensated half, it seems that the zig-zag deflection gets worse with

decreasing I_{PG}, changing from $\approx 15\,\text{mm}$ to $\approx 20\,\text{mm}$. Thus, it could be assumed that the ADCMs help also in stabilising the beamlet trajectories even with different filter field magnitudes. However, given the lack of quantitative proof for this[1], this claim remains just an assumption.

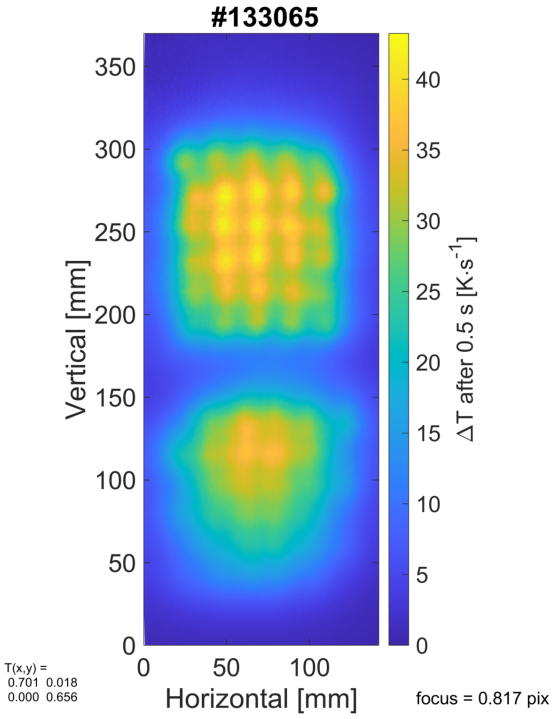

Figure 5.13: CFC tile: $I_{PG} = 3\,\text{kA}$, $P_{RF} = 80\,\text{kW}$, $P/P_0 = 0.3360$ and standard parameters.

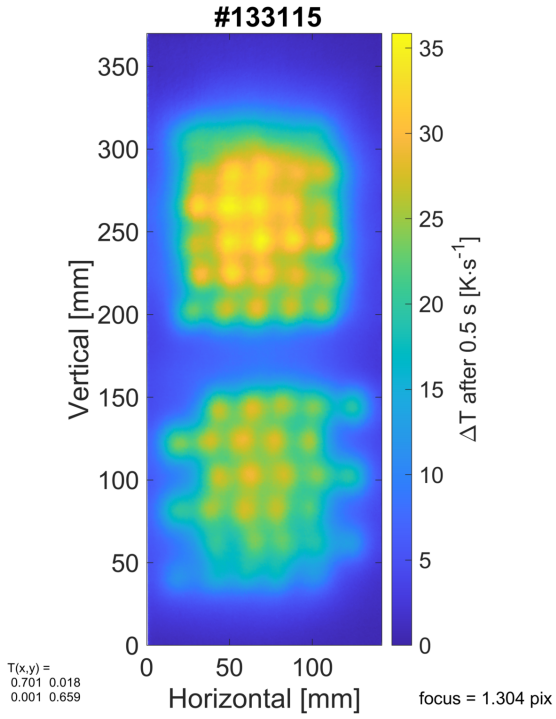

Figure 5.14: CFC tile: $I_{PG} = 1.5\,\text{kA}$, $P_{RF} = 60\,\text{kW}$, $P/P_0 = 0.3592$ and standard parameters.

1D scans with reversed filter field

In all the one dimensional scans with reversed filter field, the same dependencies analysed previously can be observed, with the only core difference in the asymmetries in deposited power being reversed: the plasma is moved by the magnetic filter field in the opposite direction, so all the previously inferred relationships are still present, but with more particle extracted from the bottom half of the grid with respect to the top half. This also leads to local perveance changes due to the inhomogeneous plasma.

$I_{PG} - P_{RF}$ 2D scan with reversed filter field

This last scan, unlike the others with reversed filter field, produced some unexpected results. In fact, it can be observed that it seems that in this case I_{PG} has an impact on the ADCMs efficiency, for currents under 2 kA. This effect was not present in the

[1]Not due to lack of data, but to the impossibility of detecting precisely the beamlet locations with this masking.

analogous scan with the standard filter field orientation, in which the magnitude of the current did not have any impact on the ADCMs compensation.

In addition to the inhomogeneous tile illumination, which causes a different plasma drift and hence a shift in the vertical position of the beamlets, a change in the beamlets horizontal position of the compensated half of the grid is observed by comparing Figures 5.15 and 5.16. We see how the top half of the latter is not as well compensated as the former, despite all the parameters having the same values. This phenomenon is unpredicted by the simulations and appears only for the reversed FF configuration, being more evident for the lowest currents.

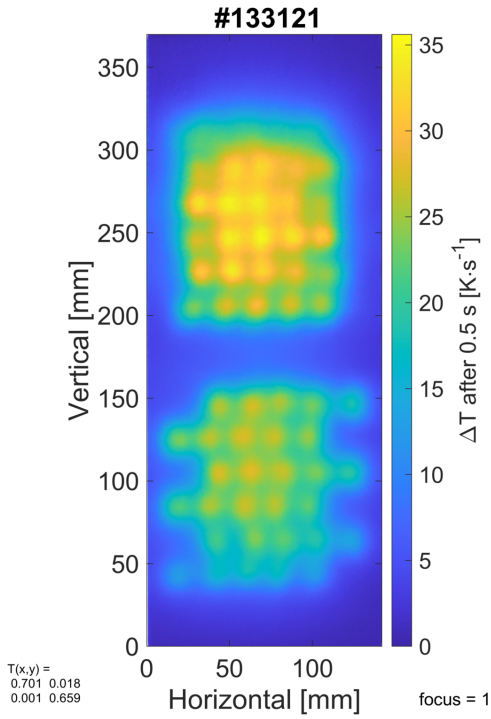

Figure 5.15: CFC tile: standard $I_{PG} = 1.25\,\text{kA}$, $P/P_0 = 0.3608$ and standard parameters.

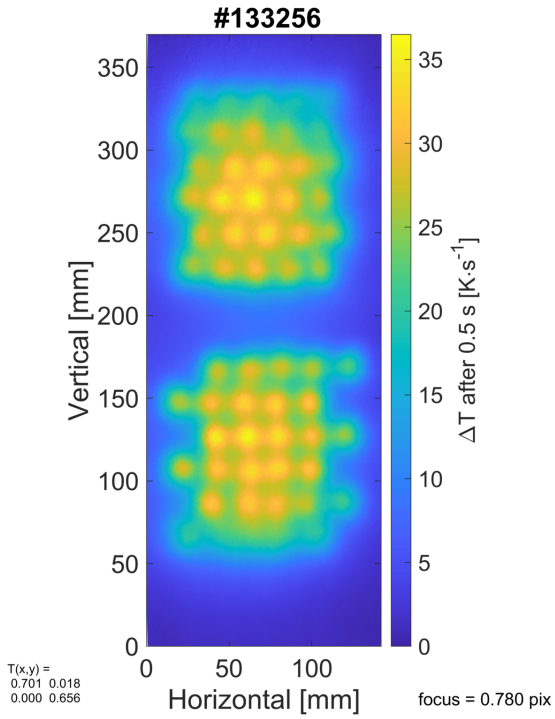

Figure 5.16: CFC tile: reversed $I_{PG} = 1.25\,\text{kA}$, $P/P_0 = 0.376$ and standard parameters.

5.2.2. BES

In this section, the analysis of the BES spectra is reported. As explained before for the simulation analysis in 4.4, for each shot a graph similar to Figure 5.17 is produced during the data-taking session. From the gaussian fitting, as mentioned in 2.2.1, it is possible to derive the beam divergence and the extra deflection α. These two quantities and their dependencies on the experimental parameters are the object of the data analysis reported below.

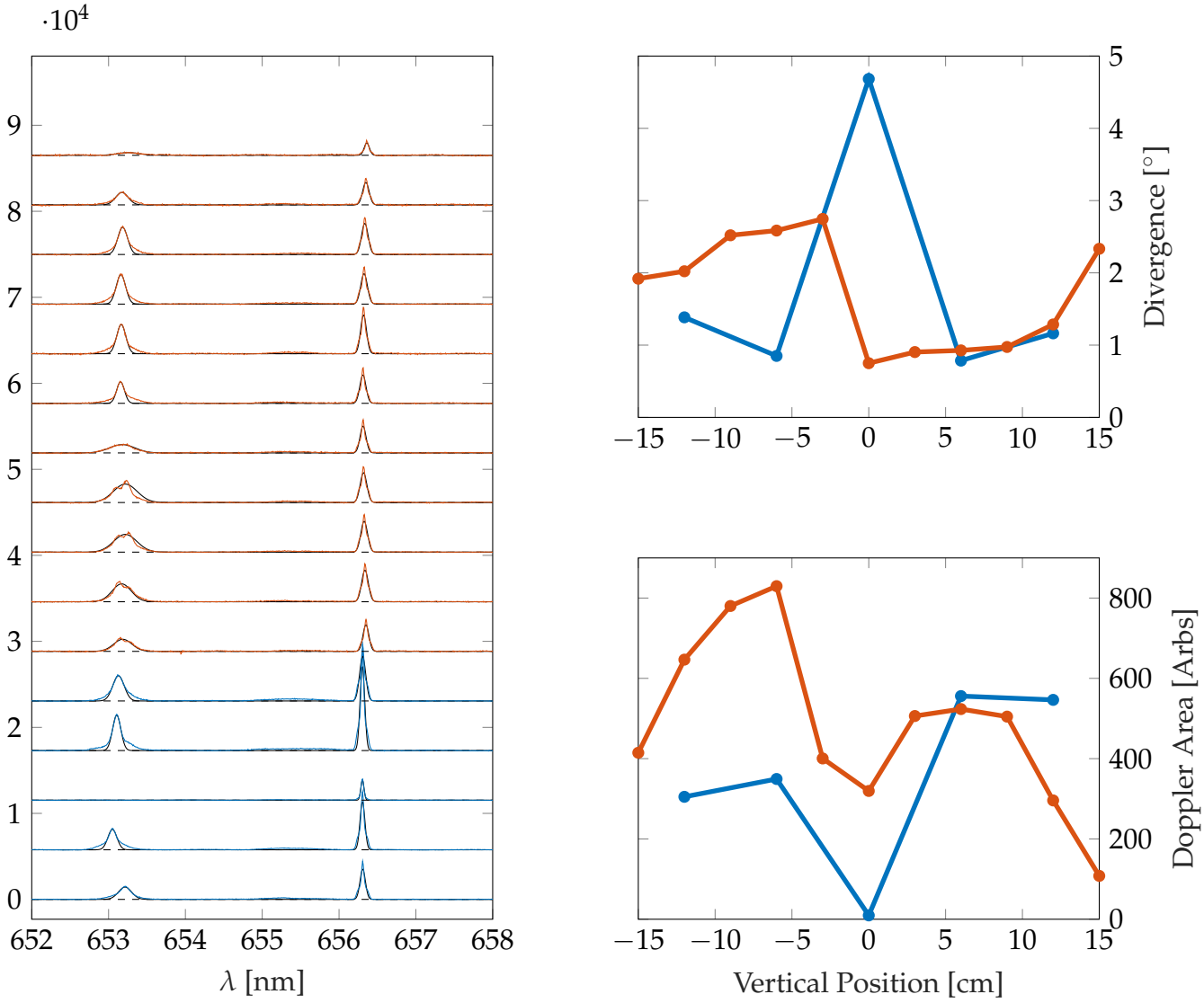

Figure 5.17: BES spectra per line of sight, divergence and Doppler peak area, shot ID 132812 (see table 5.2 for the other parameters).

U_{acc} *1D scan*

In this one dimensional scan, the most important result achieved is displayed in Figure 5.18, in which the divergence is studied as a function of U_{acc}. In the area close to the optimum voltage ratio ($U_{acc} \in [27;32.5] \implies U_{ratio} \in [5;7]$), the BES02-08 green curve clearly shows a minimum of the divergence, while BES02-03, collecting light from the uncompensated half of the grid, exhibits a totally different behaviour, with the divergence increasing with the acceleration voltage.

This difference is caused by two main phenomena, that both worsen the estimation of the divergence for the uncompensated half of the grid. First, the appearance of double peaks due to the contribution to the spectra of different beamlet rows. Secondly, by an increasing relevance of the wings (especially the right one) in the

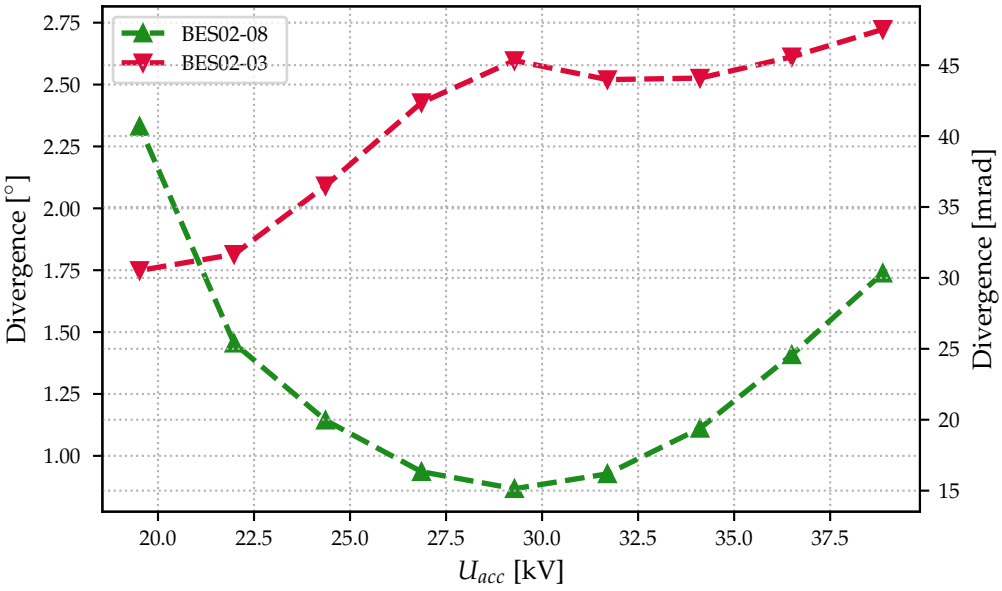

Figure 5.18: Divergence in both mrad and ° as a function of U_{acc}, for BES02-08 and BES02-03.

Doppler shifted peak, which causes the single gaussian fit not to be suitable for this distribution. These effects are corrected by the action of the ADCMs, which, by straightening the beamlet paths, can limit the magnitude of these errors.

P_{RF} *1D scans*

Analysing the BES spectra in the P_{RF} scan gives a quantitative evaluation of what observed with the CFC in 5.2.1. Indeed, the fact that the single beamlets were resolved only for $P_{RF} > 45$ can be clearly seen by looking at Figure 5.19: the divergence values estimated from BES02-08 (compensated half of the grid) are significantly lower with respect to the ones from BES02-03. Furthermore, a decreasing tendency can be outlined for the green line: the divergence gradually lowers from ≈ 30 mrad to less than 15 mrad. This was seen also from the CFC analysis, according to which the beamlets were better detectable for higher P_{RF} values. It seems that, on the other hand, the uncompensated half divergence is not affected by changes in P_{RF}: the trend is approximately constant, with divergence values in the range $[40; 45]$mrad.

A similar behaviour can be observed if the plasma grid current and hence the direction of the filter field is reversed (Figure 5.20): also in this graph, the divergence of the beamlets in the ADCM compensated part of the grid is considerably lower with respect to the uncompensated half. However, the difference between BES02-03 and BES02-08 is noticeably less marked, mainly due to the values detected by BES02-03, which are in the $[30; 35]$mrad range, 10 mrad lower than fig. 5.19.

This is consistent with the expected behaviour due to the change of FF polarity: in fact, the plasma asymmetry assessed with the CFC analysis reflects into the top or the

bottom part of the grid being more illuminated. As a consequence, when the plasma is moved downwards (reversed I_{PG}), more uniform beamlets will be produced in the uncompensated half, thus they will be at a lower divergence with respect to the ones generated in the same conditions but with the standard I_{PG} configuration, because the plasma parameters (and more specifically the temperature) will be less subject to fluctuations and heterogeneity.

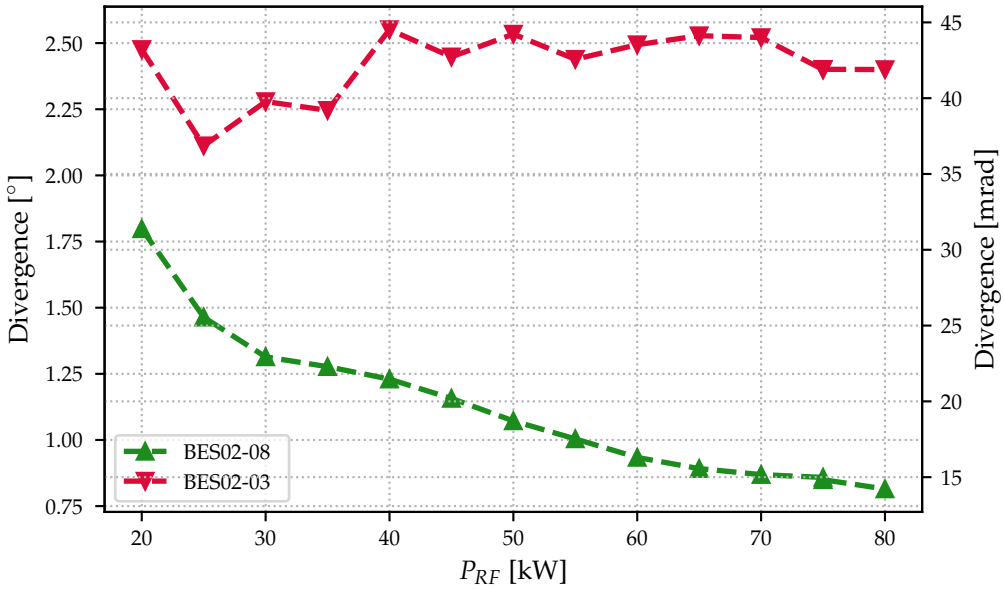

Figure 5.19: Divergence in both mrad and ° as a function of P_{RF}, for BES02-08 and BES02-03.

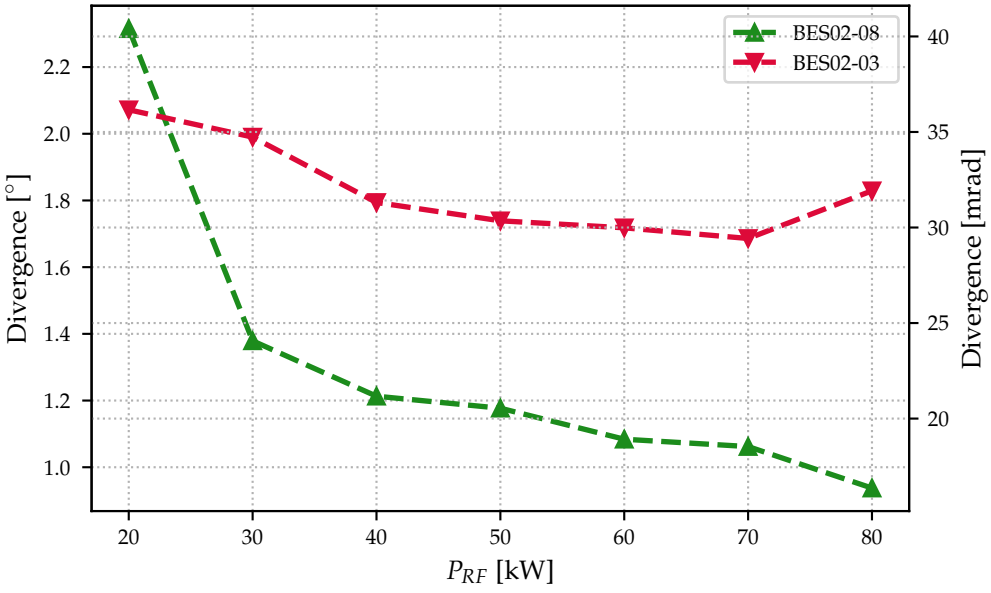

Figure 5.20: Divergence in both mrad and ° as a function of P_{RF}, for BES02-08 and BES02-03. I_{PG} is reversed.

This inhomogeneity will reflect also on the value of the normalised perveance, which will be different between the two halves of the grid: more specifically, its for the top half will decrease when changing from the standard FF configuration to the reversed one. This variation between a regime of higher perveance to a lower one causes the difference between the two graphs 5.19 and 5.20.

$U_{ext} - P_{RF}$ *2D scan at constant total voltage*

The $U_{ratio} - PRF$ 2D scan results are presented in Figure 5.21, in which the estimated divergence is plotted against the RF power values, for each different voltage ratio considered. Data collected with BES02-03 (bottom half of the grid, uncompensated) are depicted with dotted lines and a triangle facing down, while values derived from BES02-08 (compensated, top-half of the grid) with dashed lines and a pointing-up triangle. Different voltage ratios correspond to different colours.

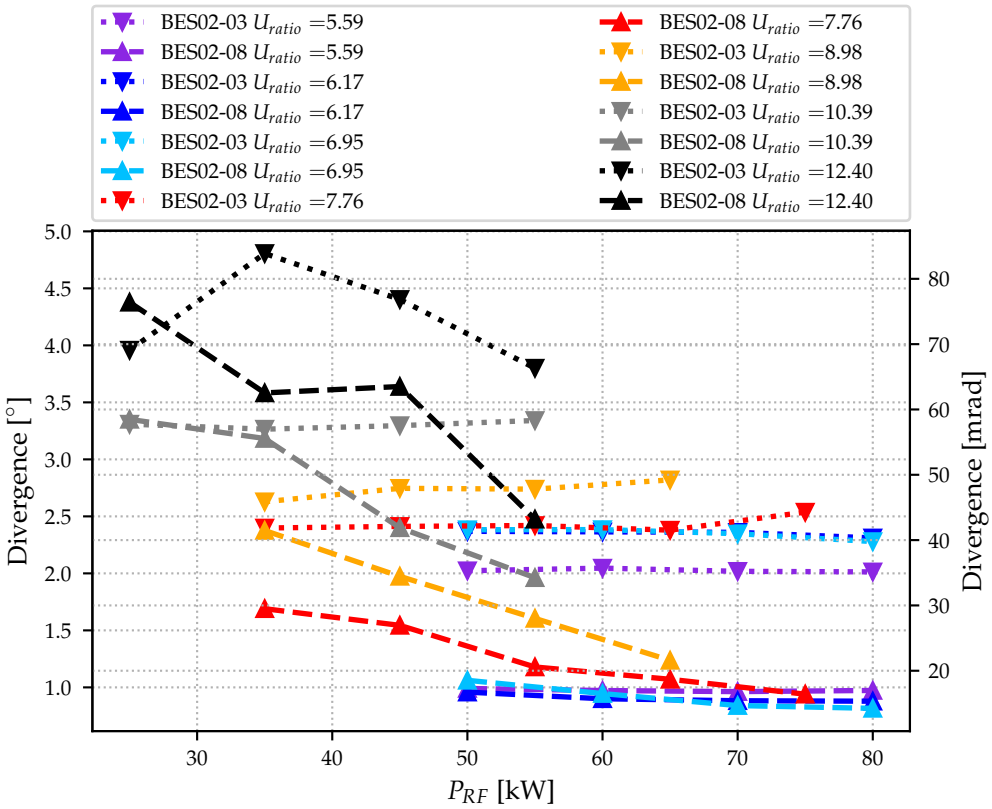

Figure 5.21: Divergence in both mrad and ° as a function of P_{RF}, for BES02-08 and BES02-03, for all the voltage ratios U_{ratio} considered.

It can be noticed that, in general, the effect of P_{RF} is smaller than that of the changing ratio on the evaluation of the divergence: in fact, in Figure 5.21, the lines representing shots with $U_{ratio} < 8$ are almost flat and do not show any relevant trend, while for the highest voltage ratios a more irregular tendency is exhibited.

The most important feature of this graph is, nevertheless, that for all the points represented except one ($P_{RF} = 25\,\text{kW}$, $U_{ratio} = 12.4$) the divergence from BES02-08 is lower with respect to BES02-03. This is due to the fact that, in the uncompensated half, the presence of multi-row contributions to the BES spectra leads to a larger divergence estimate, caused by a more spread distribution and the appearance of double peaks.

Another trait worth noticing is that, for the voltage ratios close to the design optimum ($5 < U_{ratio} < 7$), the difference between the divergence values of BES02-03 and BES02-08 is constant ($\approx 20\,\text{mrad}$). Moving away from the optimum makes a decreasing tendency in the divergence appear with increasing values of P_{RF} and generally leads to more irregular behaviour. This trend is observed only for BES02-08, while BES02-03 maintain the same behaviour of approximately constant divergence in P_{RF}. A reason for this phenomenon can be found if the experimental spectra are inspected: the Doppler shifted peak, for the highest ratios, has a particularly wide shape, due to the effect that the electrostatic lenses have on the velocity distribution. In these conditions, no particular differences are observed between the spectra of the compensated and uncompensated half, hence the behaviour displayed in the graph.

To further inspect the voltage ratio optimum properties, Figure 5.22 is realised. In this picture, the data is divided into classes (or clusters) according to the normalised perveance value, to make a consistent comparison. More specifically, in a 2D scan, 4 different values of P_{RF} are collected per voltage ratio[2]: hence, we could infer that, since the plasma parameters are expected to change 4 times (for each different P_{RF} value), approximately 4 different perveance regimes will be present. Divergence values are plotted against U_{ratio}, selecting the most relevant P/P_0 classes, similarly to Figure 4.35, in which the BBCNI-simulated values were represented. The trend outlines a minimum of the divergence for U_{ratio} around 7 for BES02-08. Divergence then increase steeply for higher voltage ratios: in these conditions, the extraction voltage is too low and this lead to a situation similar to the one reported in Figure 2.4.(a), in which the beamlet focal point is very close to the PG.

The uncompensated half of the grid, on the other hand, shows divergence values that are almost doubled with respect to the compensated one for voltage ratios < 8, which then increase less decisively compared to the BES02-08 ones. This could be due to the inability of the plotting routine to perceive the changes in the spectra due to different perveance regimes, consistently with what stated before.

It is worth observing that the clustering procedure did not include any high-ratio point for the $P/P_0 = 0.327$ cluster. This can be explained by considering that for $U_{ratio} > 12$, the RF scanned values produced did not produce normalised perveances that fall into the middle cluster. A more thin scan in the low RF values could have filled the gap in the light-blue dataset.

[2]or for any other variable in the other scans.

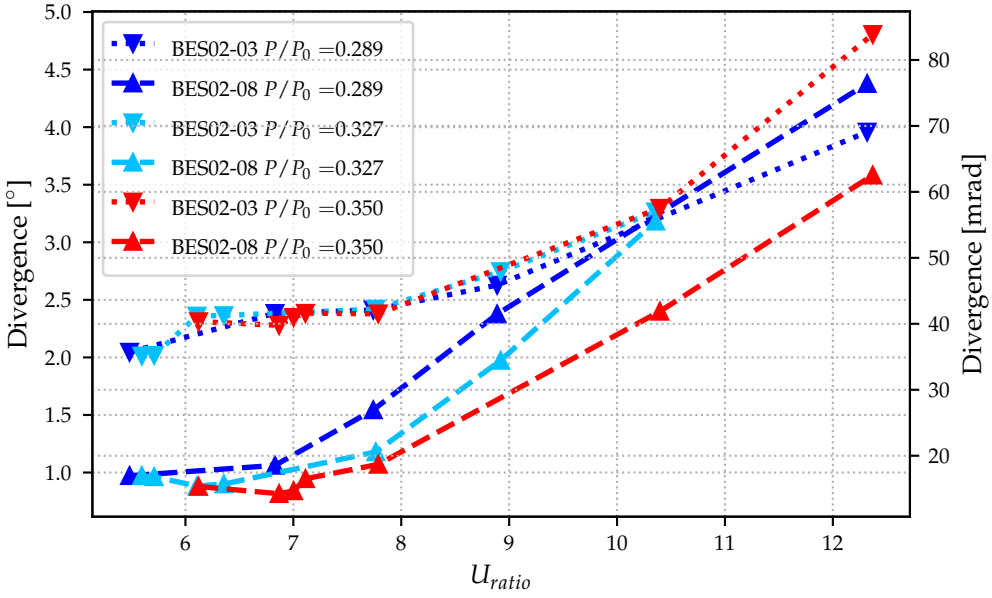

Figure 5.22: Divergence in both mrad and ° as a function of U_{ratio}, for BES02-08 and BES02-03, at selected perveance values.

The data collected for this scan can be directly compared with the BBCNI-simulated ones, as reported in Figure 5.23. In this picture, the BBCNI estimated divergences are plotted together with the experimental data at the same P/P_0 (the blue line) and at the ones computed at the optimum experimental normalised perveance. It is clear that, while the trend depicted is comparable, experimentally the minimum of the divergence in U_{ratio} is less marked and besides the empirical values are higher with respect to the synthetic ones. However, the strong growth of the divergence with increasing U_{ratio} values is preserved, even though it is more pronounced for the BBCNI dataset, and so is the position of the minimum: therefore, one can state that also experimentally there exist an optimum voltage ratio for which the ADCM compensation is effective also on the divergence, located in $5 < U_{ratio} < 7$.

The differences between BBCNI and experiment are due to the various systematic errors that the simulations ignore when deriving the spectra: for lower ratios, the shape of the synthetic Doppler shifted peak is more regular and not affected by all the experimental noise that in reality impacts on the data. For the higher ratios, instead, the Doppler shifted peak is wider for both the experiment and BBCNI, hence the absolute values of the divergence are closer to each other.

Finally, from the difference between the expected Doppler shift and the measured one, the horizontal extra deflection α can be estimated according to equation from (2.23). This quantity allows us to assess how ADCMs compensation works as a function of the studied parameters. To limit the influence of neighbour rows of beamlets, the LOS of BES01-01 (uncompensated half of the grid) and BES01-04 are considered.

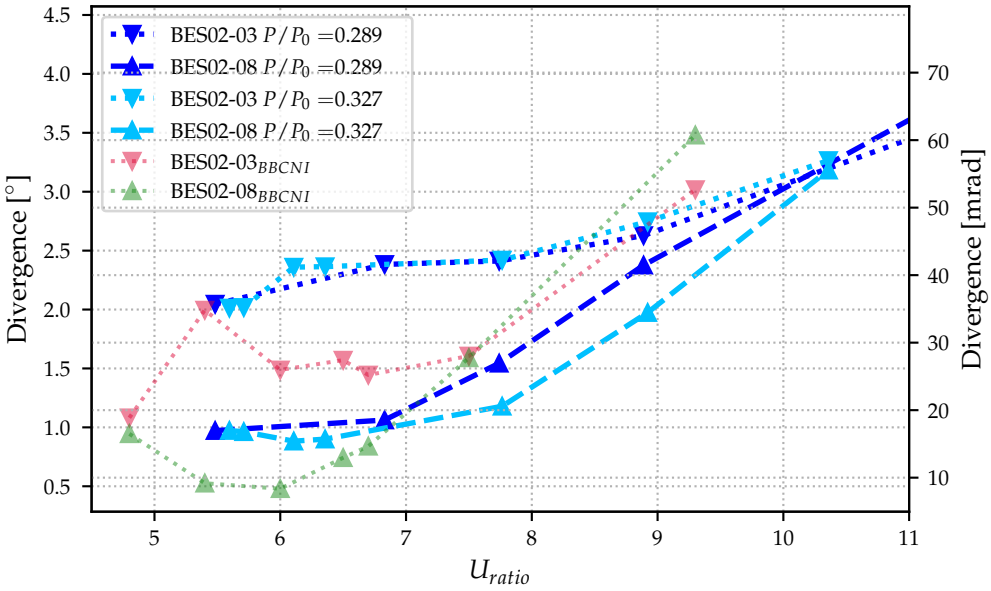

Figure 5.23: Comparison between BBCNI and experimental divergence in both mrad and ° as a function of U_{ratio}, for BES02-08 and BES02-03. $P/P_0 \approx 0.28$ for the BBCNI data and the blue line, while for the light blue line $P/P_0 \approx 0.33$.

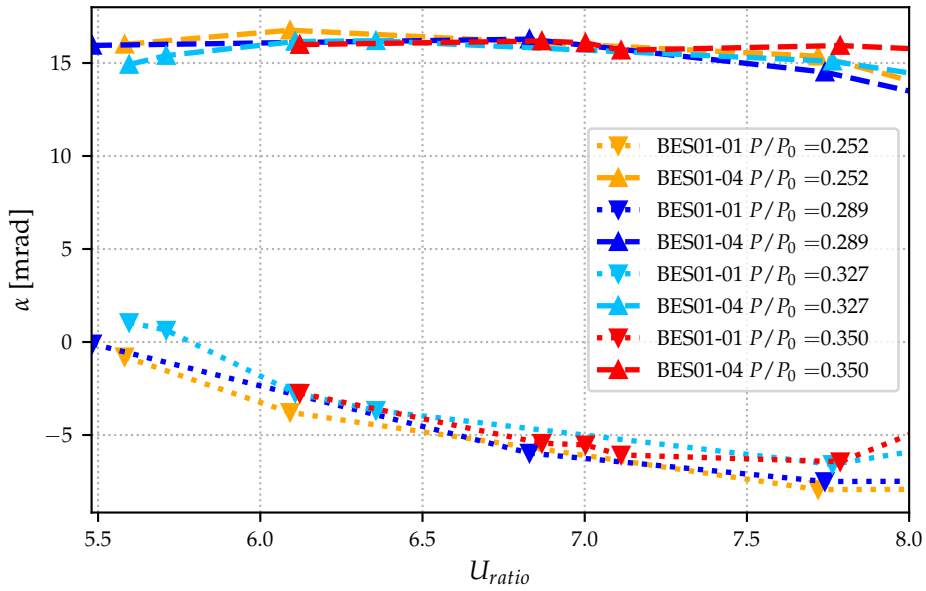

Figure 5.24: Extra horizontal deflection α as a function of U_{ratio}, for different P/P_0 values.

In Figure 5.24, α is plotted for different P/P_0 values as a function of U_{ratio}, restricted to the range $[5.5; 8]$. A clear distinction can be observed between the uncompensated half of the grid and the compensated half: in fact, all the BES01-04 data shows very little dependence on the voltage ratio, while for the uncompensated LOS, the value of α decreases with increasing U_{ratio} values. This happens because, as it can be seen in Figure 6 of [32], when the voltage ratio changes, the contribution to the BES-acquired

spectra of a single row varies due to the different optic. If the beamlets are aligned (compensated half of the grid), the rows contribution to α will be approximately constant, while in the uncompensated case, the different trajectories of beamlet rows will lead to a variation on the α estimation, depending not only on how much each row contribute to the LOS spectra but also on the absolute value of the zig-zag deflection. Seeing that in Figure 5.24 BES01-04 shows a constant behaviour is due to the compensation actuated by the ADCMs, which by correcting the zig-zag deflection ensure that the different row contributions provide the same extra deflection.

$U_{ext} - P_{RF}$ *2D scan at constant voltage ratio*

In this scan, the voltage ratio is kept fixed at 6.5, while the RF power P_{RF} and the total voltage U_{tot} are changed. The data, similarly to what was done for the previous scan, is displayed in Figure 5.25, with the same style convention.

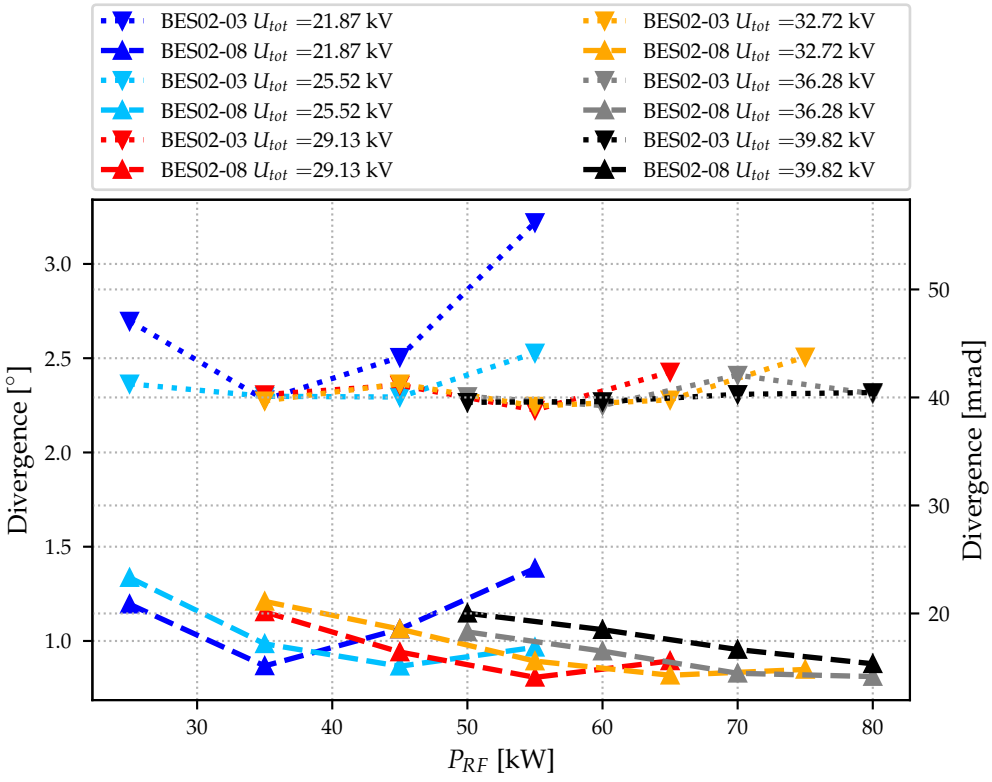

Figure 5.25: Divergence in both mrad and ° as a function of P_{RF}, for BES02-08 and BES02-03, at different total voltages.

The most striking feature of this graph is that, once again, the ADCMs compensated divergence estimates are significantly lower with respect to the uncompensated one, by more than a factor 2. Moreover, it can be observed that all the lines show a

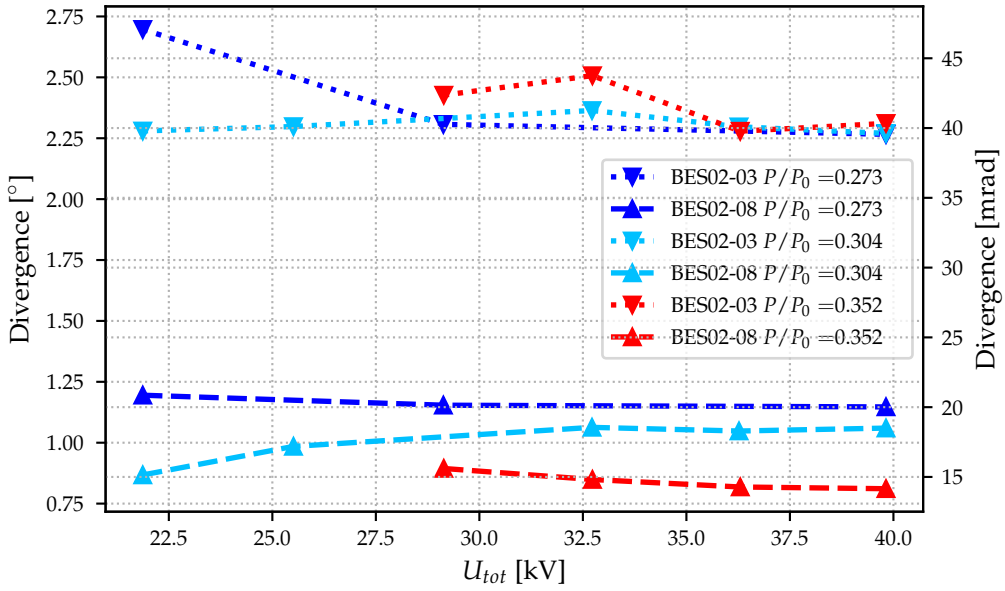

Figure 5.26: Divergence in both mrad and ° as a function of U_{tot}, for BES02-08 and BES02-03, at selected perveance values.

comparable trend: there exist a value of P_{RF} for which the divergence is minimum. For the highest U_{tot} the minimum is not so clearly visible and is probably located at higher values of P_{RF}, out of the experimental range. This dependence is less marked for the uncompensated half of the grid, while it is more visible for BES02-08. However, it is not particularly marked, especially for $U_{tot} > 29$ kV, and the significant difference in divergence is preserved independently from P_{RF}.

Similarly to what was done for the U_{ratio} scan, also in this case to gain more insight about the divergence behaviour as the total voltage changes, a plot of the divergence as a function of U_{tot} (Figure 5.26) is generated. Data is grouped by normalised perveance values, and three subsets are displayed, corresponding to three different P/P_0 values.It is evident that the total voltage has only a very slight influence on the divergence, as it was assumed by looking at the CFC pictures in section 5.2.1 for the U_{tot} scan: in Figure 5.26 all the lines show a flat tendency, with a slight shift upwards when the P/P_0 value is changed. This is consistent with the theory: since the voltage ratio is not changed and that each colour represent a certain perveance regime, the optic (and hence the divergence) is expected to be constant, given that the meniscus shape and the electrostatic lens should not be influenced.

Finally for this scan, a comparison between the experimental results and the simulations is included in Figure 5.27. The simulations do not perfectly match the empirical results: in fact, for Figure 5.27, the difference between BES02-03 and BES02-08 is preserved, and so is the independence from U_{tot} for the compensated divergence, but the decreasing trend that the simulations showed for BES02-03 is completely absent experimentally. Moreover, the divergence of BES02-08 is bigger

experimentally of about $5 - 7$mrad, and even more for the uncompensated LOS. The increased divergence can be due to many systematic errors that the simulations do not take into account, so this result is expected.

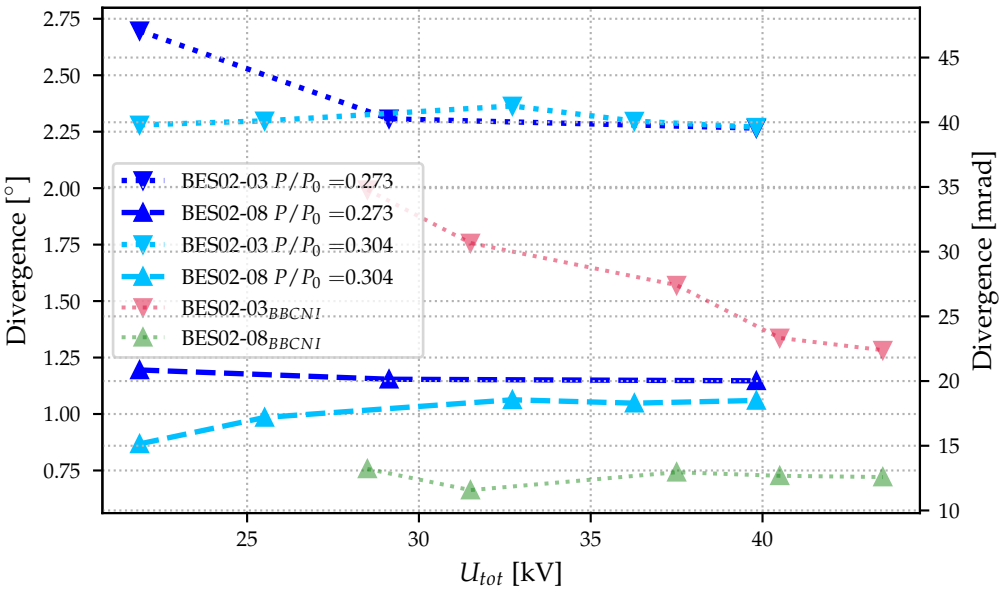

Figure 5.27: Comparison between simulated and empirical data: divergence in both mrad and ° plotted as a function of U_{tot}, for BES02-08 and BES02-03, at selected perveance values.

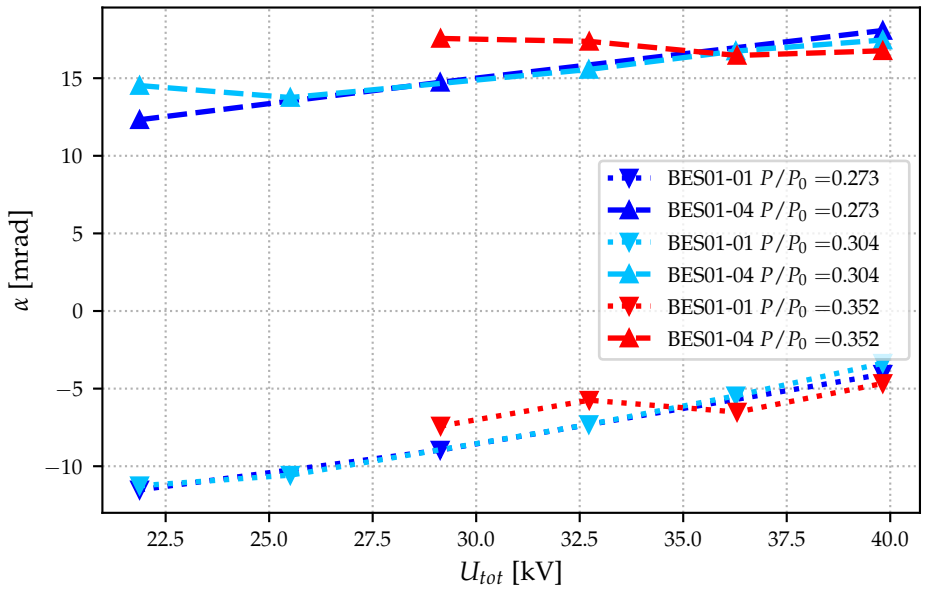

Figure 5.28: Extra horizontal deflection α as a function of U_{tot}, for different P/P_0 values.

Also for this case the extra deflection α can be estimated, plotting its value as a function of U_{tot} for different perveance regimes (Figure 5.28). Differently from

Figure 5.24, in this case both the uncompensated and compensated LOS show the same tendency. This is because, at a fixed ratio, the contribution to the spectra of different beamlet rows is the same, moreover, the zig-zag compensation, as seen in the simulations (Figure 4.26, 4.28), is not particularly affected by the total voltage.

I_{bias} *1D scans at constant perveance*

The bias current has a peculiar impact on the divergence. It can be seen, when plotting the divergence versus I_{bias} (Figure 5.29), that as the current increase, the beamlet divergence increases for the compensated half, while it decreases for the uncompensated one. BES02-08 reflects what already observed with the CFC (Figures 5.9, 5.10): in fact, the beamlet resolution was worsened by I_{bias}, despite the constant perveance regime. However, BES02-03 seems to present an unexpected behaviour, with its divergence improving as the bias current increase. When the plasma grid current is reversed, this tendency is preserved, with only a slight average reduction of the BES02-03 divergence.

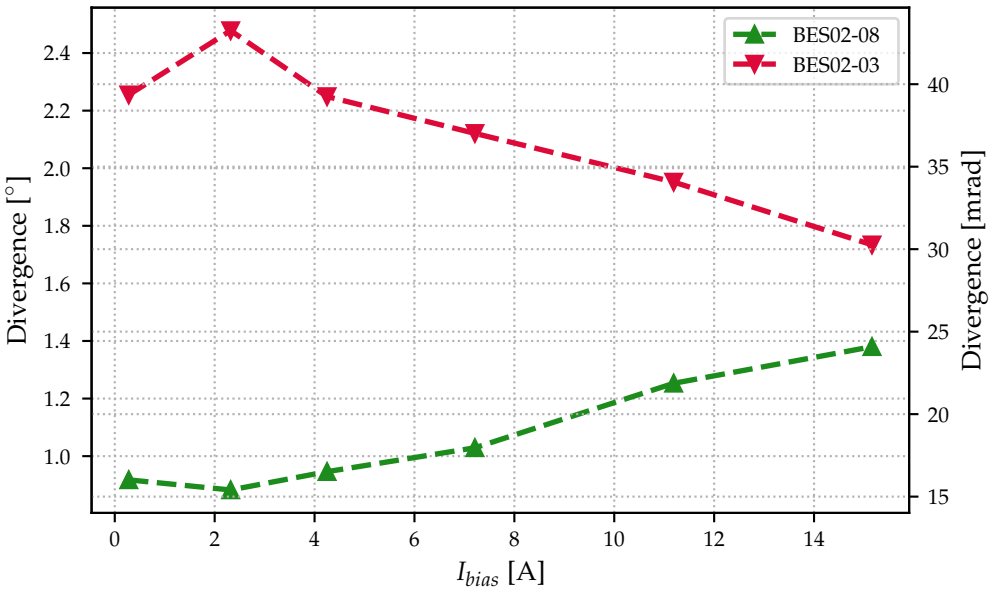

Figure 5.29: Divergence in both mrad and ° as a function of I_{bias}, for BES02-08 and BES02-03.

p_{fill} *1D scans at constant perveance*

The dependence on the filling pressure already highlighted in section 5.2.1 can be better seen in Figures 5.30 (standard FF direction) and 5.31 (reversed FF). In fact, for the lowest p_{fill} values, a steep increase of the divergence can be noticed for the compensated half in both graphs, and also for the uncompensated one for fig. 5.31.

Anyway, in both pictures it is clear that the ADCM addition improves the estimate of the divergence: the green line is always below the red one, with a difference

between the two ranging from a minimum of 5 mrad (fig. 5.31, for $p_{fill} = 0.7$ Pa) to 20 mrad (fig. 5.30, for $p_{fill} = 0.57$ Pa). The differences between the two plots are once again due to the plasma asymmetry mentioned for the P_{RF} scans when commenting Figures 5.19 and 5.20, which not only varies the values represented, but change the divergence trend for BES02-03.

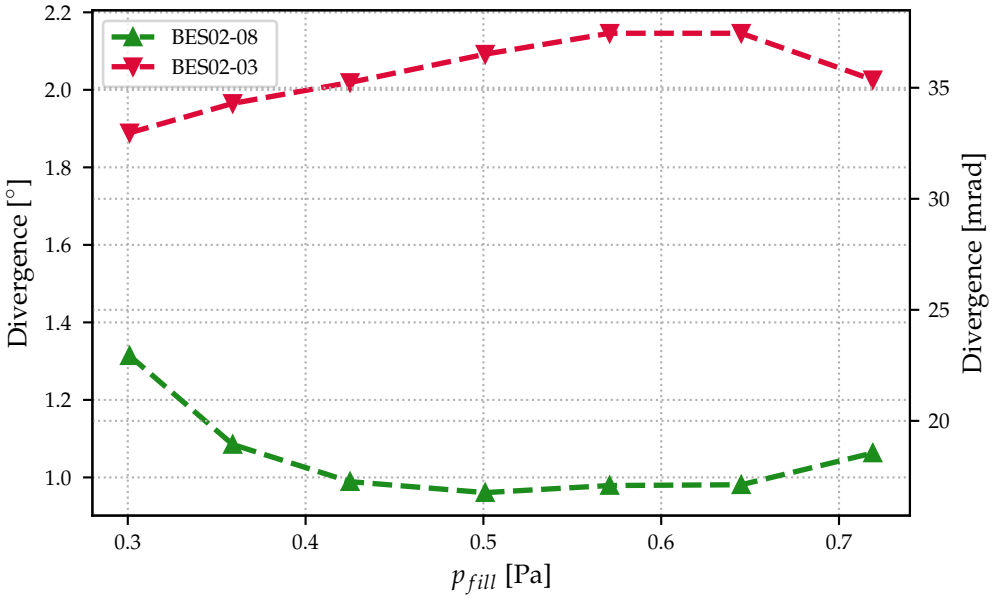

Figure 5.30: Divergence in both mrad and ° as a function of p_{fill}, for BES02-08 and BES02-03.

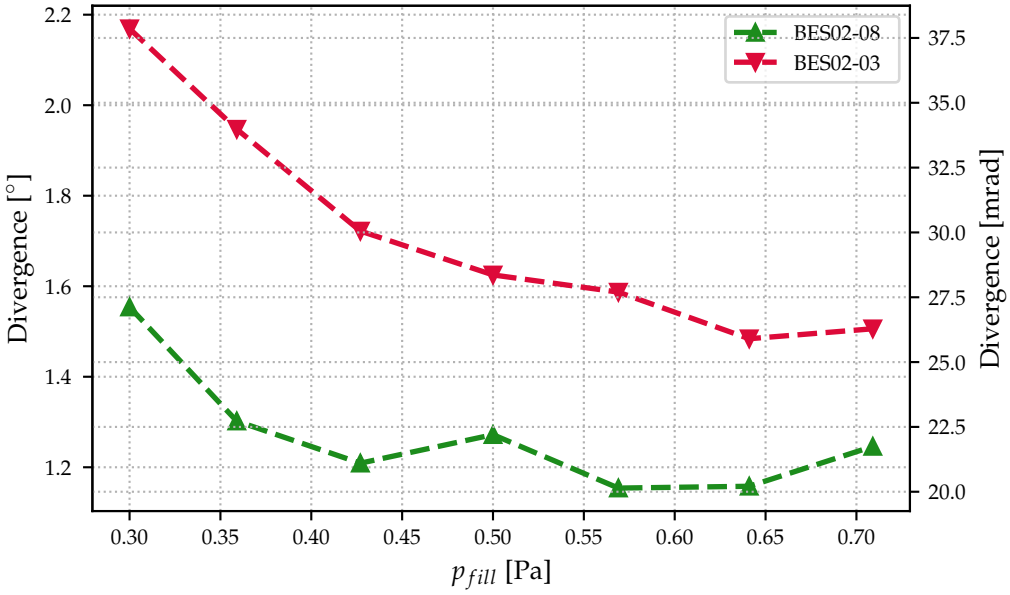

Figure 5.31: Divergence in both mrad and ° as a function of p_{fill}, for BES02-08 and BES02-03. I_{PG} is reversed.

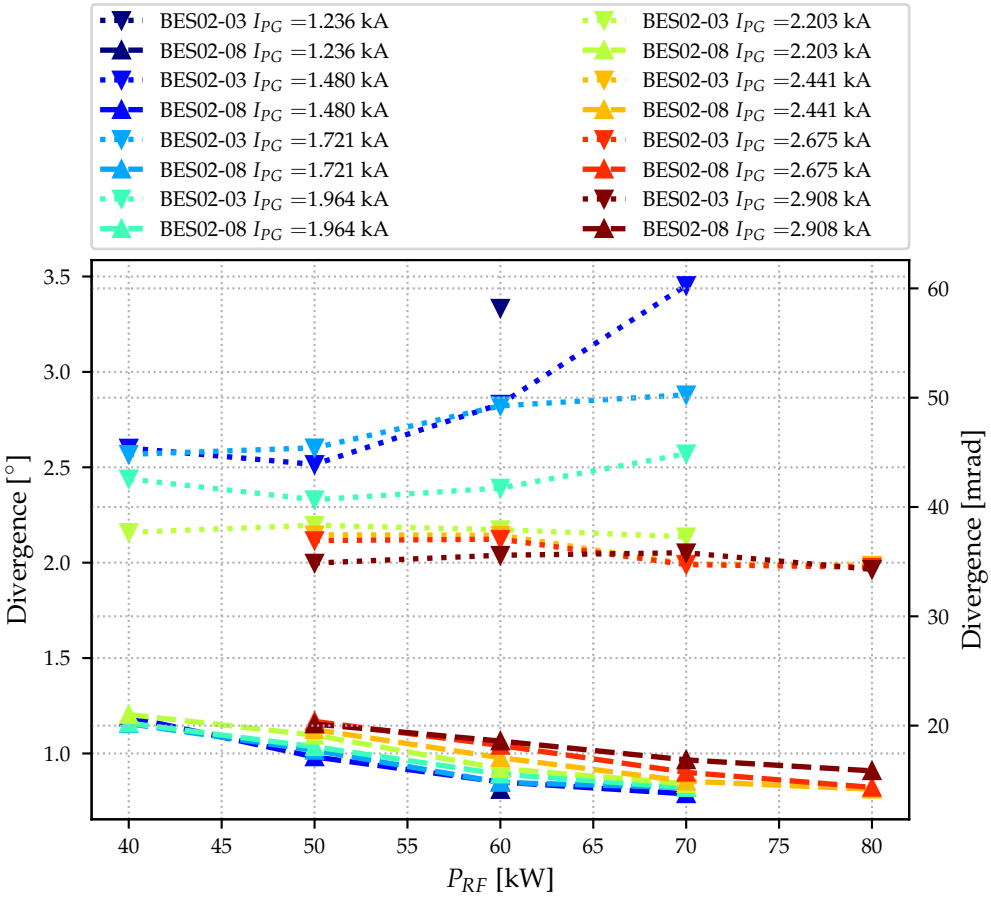

Figure 5.32: Divergence in both mrad and ° as a function of P_{RF}, for BES02-08 and BES02-03, for different values of I_{PG}.

$I_{PG} - P_{RF}$ *2D scans*

For these last experimental scans, the parameters considered are the plasma grid current I_{PG} (which could be in the standard direction or reversed) and the RF power P_{RF}. The divergence values are presented in Figures 5.32 (standard I_{PG} direction) and 5.33 (reversed I_{PG}), with the same style convention previously applied.

Concerning Figure 5.32, one can immediately see the action of the ADCMs compensation: the dashed lines (BES02-08) show only a very slight decreasing tendency with P_{RF} raising, and their values are all < 20 mrad. Conversely, the BES02-03 values are all > 35 mrad, and for values of the plasma grid current smaller than 2 kA, a growth of the divergence when P_{RF} increase is present. Observing the spectra, one can see that this is caused by the bimodal shape of the Doppler shifted peak, that seems to be more defined and wider for the highest values of P_{RF}, but only for the uncompensated half: the new magnetic configuration helps in obtaining Doppler peaks with only one maximum, which can then be approximated with a gaussian.

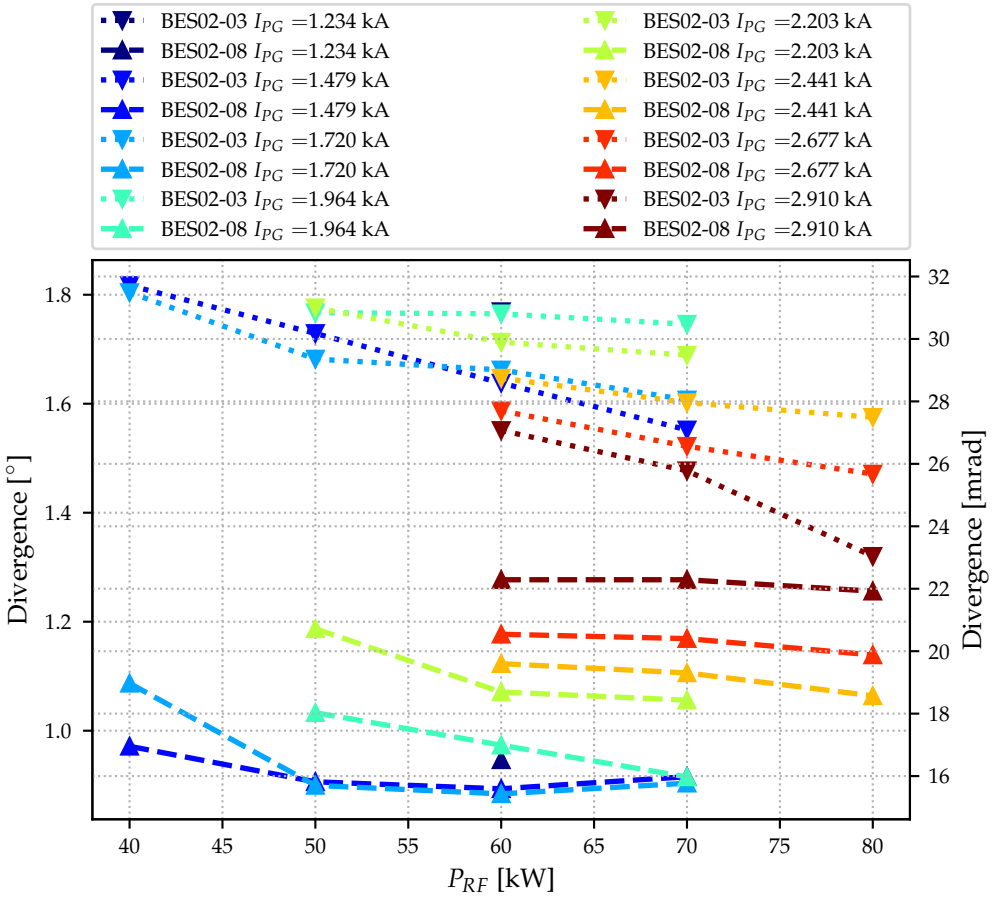

Figure 5.33: Divergence in both mrad and ° as a function of P_{RF}, for BES02-08 and BES02-03, for different values of I_{PG} (reversed). Only one point is collected for $I_{PG} = 1.2$kA due to the high ratio of co-extracted electrons/negative ions in that conditions.

However, the decreasing tendency for BES02-08 reflects the one observed with the CFC in section 5.2.1, in which the beamlets were better resolved for bigger RF powers, and the changes in I_{PG} (and as a consequence in the magnitude of the filter field) impacted on the vertical position of the beamlets. This FF-induced shift might be the cause of the changes in the divergence for the uncompensated part of the grid: in fact, the light collected by BES02-03 will derive from different beamlet rows, hence the distribution of the spectra and consequently the inferred divergence will be different.

Moreover, one must consider that for lower values of I_{PG} the magnitude of the filter field may be too low to properly deflect the co-extracted electrons properly. The high ratio of co-extracted electrons/negative ions is also the reason why only one point is collected for $I_{PG} = 1.2$kA.

One would expect that Figure 5.33, representing an analogous situation with respect to 5.32, with simply a reversed I_{PG}, would show totally comparable trends.

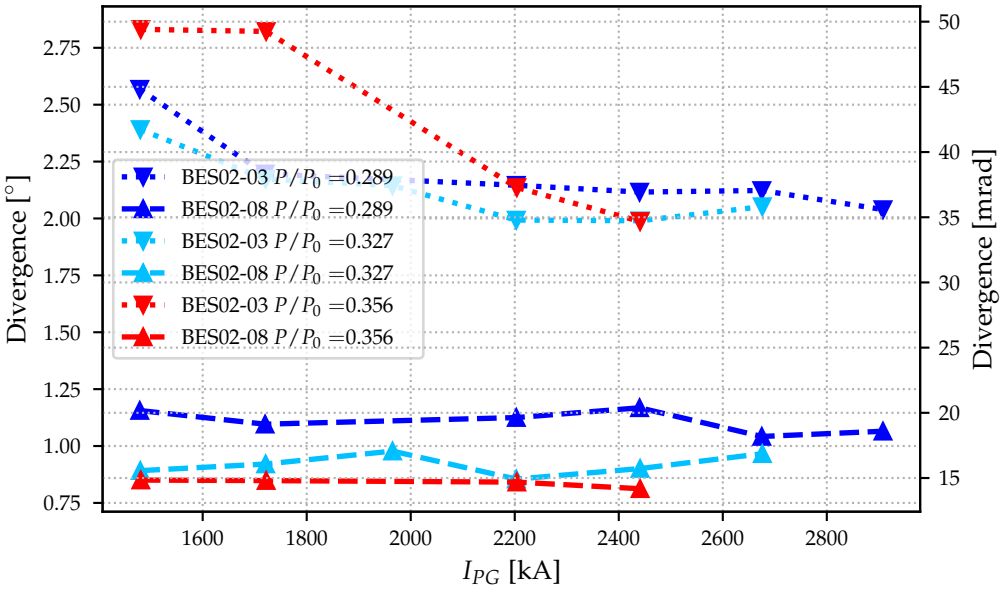

Figure 5.34: Divergence in both mrad and ° as a function of I_{PG}, for BES02-08 and BES02-03, for selected perveance values.

What happens, instead, is that with the reversed FF, the dependence of the divergence on P_{RF} for the uncompensated half of the grid changes significantly: it can be seen that the divergence decreases with larger P_{RF} values, more and more steeply with I_{PG} growing. Besides, the uncompensated divergences range between $[24;32]$mrad, a much narrower and lower range with respect to the standard FF orientation ($[34;60]$mrad).

Concerning the compensated half, instead, it can be noticed that BES02-08 data are not nicely superimposed anymore, meaning that a trend also in I_{PG} emerge: it seems that with the magnitude of the FF increasing, the differences between the top and bottom divergence tend to even out, despite the compensated half still showing lower values. This could be due to a decreasing local perveance with an increasing FF, which leads to beamlets with different optics, as also pointed out for the experimental CFC analysis in Figures of page 75.

This asymmetric behaviour is probably due to the plasma asymmetries induced by the magnetic field, however, it is anyway unexpected how heavy the impact is on the divergence. To further inspect this phenomenon, Figures 5.34 and 5.35 are produced, representing how the divergence varies as a function of I_{PG}, respectively in the standard and reversed direction. Like for the other 2D scans, data is split according to the normalised perveance values.

It can be observed that the aforementioned difference is present when comparing the two graphs. For the standard FF, the PG current seems not to have any particular effect on the compensated half of the grid, while it makes the divergence decrease for the uncompensated one. On the other hand, in the reversed FF configuration,

increasing I_{PG} leads to a growth in the divergence for BES02-08 and to a reduction for BES02-03. Regardless, the compensation magnets manages to keep the divergence lower, despite this unexpected behaviours arising.

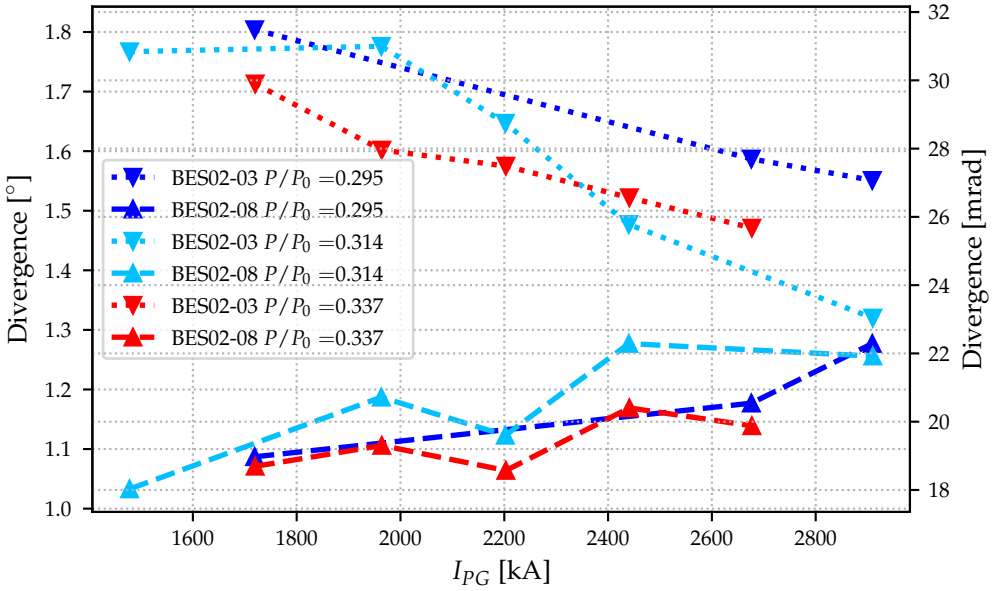

Figure 5.35: Divergence in both mrad and ° as a function of I_{PG}, for BES02-08 and BES02-03, for selected perveance values. I_{PG} is reversed.

6
Conclusion

In this work, a comparison of experimental and computational results has been successfully carried out, thanks to the particle tracking codes and the data collected. In particular, it can be stated that the ADCM addition to the grid system of BUG-MLE is functional for correcting the zig-zag deflection, as shown by both simulations (section 4.3) and CFC data analysis (section 5.2.1), within the ITER requirements for the horizontal misalignment ($\pm$2mrad, Table 1.2).

More specifically, in the experiment, the ADCMs manage to compensate the horizontal deflection for voltage ratios U_{ratio} between 5 and 7, as designed by the simulations. The RF power P_{RF}, the total voltage U_{tot} and the filling pressure p_{fill} did not have a particular effect on the performance of the correction in the CFC measurements. In the simulation, the horizontal beamlet position is not sensitive to the injected current density and the total potential when the U_{acc}/U_{ext} ratio is kept constant.

The filter field is not expected to influence the horizontal position of the beamlets on the CFC. Nevertheless, it indirectly influences the ion-optics via the plasma drift which leads to an inhomogeneous grid illumination. The bad electrical contact between insert and plasma grid frame complicates the analysis since the middle beamlets are deflected less vertically. In the compensated beam half, the deflection correction seems less effective at low I_{PG} currents.

Concerning the beamlet divergence, the BES simulations (section 4.4) and experimental analysis (section 5.2.2) produced qualitatively agreed. The main relationships between the various parameters scanned and the difference between the top and bottom half of the grid are generally consistent between simulations and empirical data, but the simulations tend to report lower divergence values. Of course, this is comprehensible if one considers the systematic errors (i.e., surface production, or errors specifically due to the telescope acceptances) that the simulations ignore while

modelling the experimental apparatus. Quantitative agreement is not expected, since the plasma region is highly simplified in the modelling.

The beamlet divergence, comparing the ADCMs compensated half of the grid and the uncompensated half, showed many dependencies on the experimental conditions, and substantial differences between the 2 halves. In particular, the optimum divergence for the compensated half corresponds to voltage ratios $5 < U_{ratio} < 7$, i.e. the same optimum outlined for the best deflection correction. Besides, an ideal P/P_0 value that minimise the divergence exists for a fixed U_{tot}. The plasma grid current dependence is an indirect consequence of the plasma inhomogeneity, due to the fact that if the PG illumination is not regular, the current density injected in different apertures will be affected and so will the divergence. This phenomenon is much more relevant for the uncompensated half of the grid, meaning that the ADCMs have an impact also in these conditions, despite the aforementioned technical issue which induced an extra-asymmetry when I_{PG} is reversed. The bias current I_{bias} cannot be incremented too much to have clearly distinguishable beamlets with low divergence, and the filling pressure makes the beamlets too divergent to be distinguishable at the ITER-required value of 0.3 Pa.

In conclusion, in this thesis the robustness of the correction effect of the ADCMs has been analysed, showing that indeed they are good tools for approaching the ITER-like parameters concerning the misalignment tolerance, with efficient action for a wide set of experimental parameters. Furthermore, it has been assessed that the ADCMs indeed improve the beamlet divergence estimation and have a clearly distinguishable impact when comparing top and bottom half of the grid, making the target goal of 7 mrad divergence closer.

References

[1] H. Ritchie, "Energy mix," 2019. [Online]. Available: https://ourworldindata.org/grapher/energy-consumption-by-source-and-region?stackMode=absolute&country=~OWID_WRL

[2] IEA, "Evolution of global GDP, total primary energy demand and energy related CO2 emissions," 2019. [Online]. Available: https://www.iea.org/data-and-statistics/charts/evolution-of-global-gdp-total-primary-energy-demand-and-energy-related\-co2-emissions-relative-to-2019

[3] IAEA, "Evaluated nuclear data file (ENDF)," 2021. [Online]. Available: https://www-nds.iaea.org/exfor/endf.htm

[4] A. Bradshaw, T. Hamacher, and U. Fischer, "Is nuclear fusion a sustainable energy form?" *Fusion Engineering and Design*, vol. 86, no. 9, pp. 2770–2773, 2011, proceedings of the 26th Symposium of Fusion Technology (SOFT-26). [Online]. Available: https://www.sciencedirect.com/science/article/pii/S0920379610005119

[5] V. Toigo *et al.*, "The PRIMA test facility: SPIDER and MITICA test-beds for ITER neutral beam injectors," *New Journal of Physics*, vol. 19, no. 8, p. 085004, Aug 2017. [Online]. Available: https://doi.org/10.1088/1367-2630/aa78e8

[6] ITER. [Online]. Available: https://www.iter.org/

[7] K. Berkner, R. Pyle, and J. Stearns, "Intense, mixed-energy hydrogen beams for CTR injection," *Nuclear Fusion*, vol. 15, no. 2, pp. 249–254, Apr 1975. [Online]. Available: https://doi.org/10.1088/0029-5515/15/2/009

[8] IAEA, *ITER Technical Basis*. Vienna: ITER EDA Documentation Series No. 24, IAEA, 2002.

[9] R. S. Hemsworth *et al.*, "Overview of the design of the ITER heating neutral beam injectors," *New Journal of Physics*, vol. 19, no. 2, p. 025005, Feb 2017. [Online]. Available: https://doi.org/10.1088/1367-2630/19/2/025005

[10] E. Speth, M. Ćirić *et al.*, "RF ion sources for fusion applications: design, development and performance," 1999.

[11] B. Heinemann *et al.*, "Upgrade of the BATMAN test facility for H- source development," *AIP Conference Proceedings*, vol. 1655, no. 1, p. 060003, 2015. [Online]. Available: https://aip.scitation.org/doi/abs/10.1063/1.4916472

[12] D. Wünderlich, S. Mochalskyy, U. Fantz, P. Franzen *et al.*, "Modelling the ion source for ITER NBI: from the generation of negative hydrogen ions to their extraction," *Plasma Sources Science and Technology*, vol. 23, no. 1, p. 015008, Jan 2014. [Online]. Available: https://doi.org/10.1088/0963-0252/23/1/015008

[13] M. Bacal, "Physics aspects of negative ion sources," *Nuclear Fusion*, vol. 46, no. 6, pp. S250–S259, May 2006. [Online]. Available: https://doi.org/10.1088/0029-5515/46/6/s05

[14] U. Fantz, P. Franzen, W. Kraus, M. Berger, S. Christ-Koch, M. Fröschle, R. Gutser, B. Heinemann, C. Martens, P. McNeely, R. Riedl, E. Speth, and D. Wünderlich, "Negative ion RF sources for ITER NBI: status of the development and recent achievements," *Plasma Physics and Controlled Fusion*, vol. 49, no. 12B, pp. B563–B580, Nov 2007. [Online]. Available: https://doi.org/10.1088/0741-3335/49/12b/s53

[15] E. Speth, H. Falter, P. Franzen, U. Fantz, M. Bandyopadhyay, S. Christ, A. Encheva, M. Fröschle, D. Holtum, B. Heinemann, W. Kraus, A. Lorenz, C. Martens, P. McNeely, S. Obermayer, R. Riedl, R. Süss, A. Tanga, R. Wilhelm, and D. Wünderlich, "Overview of the RF source development programme at IPP garching," *Nuclear Fusion*, vol. 46, no. 6, pp. S220–S238, May 2006. [Online]. Available: https://doi.org/10.1088/0029-5515/46/6/s03

[16] M. Cavenago and P. Veltri, "Deflection compensation for multiaperture negative ion beam extraction: analytical and numerical investigations," *Plasma Sources Science and Technology*, vol. 23, no. 6, p. 065024, Sep 2014. [Online]. Available: https://doi.org/10.1088/0963-0252/23/6/065024

[17] G. Chitarin, A. Kojima, P. Agostinetti, D. Aprile, C. Baltador, J. Hiratsuka, M. Ichikawa, N. Marconato, E. Sartori, G. Serianni, P. Veltri, M. Yoshida, M. Kashiwagi, M. Hanada, and V. Antoni, "Experimental validation of an innovative deflection compensation method in a multi-beamlet negative-ion accelerator," *AIP Conference Proceedings*, vol. 1869, no. 1, p. 030026, 2017. [Online]. Available: https://aip.scitation.org/doi/abs/10.1063/1.4995746

[18] S. Mochalskyy, A. Lifschitz, and T. Minea, "3D modelling of negative ion extraction from a negative ion source," *Nuclear Fusion*, vol. 50, no. 10, p. 105011, Sep 2010. [Online]. Available: https://doi.org/10.1088/0029-5515/50/10/105011

[19] A. Pimazzoni, "Investigation of the parameters of a particle beam by numerical models and diagnostic calorimetry," Ph.D. dissertation, Università degli Studi di Padova, 2018. [Online]. Available: http://paduaresearch.cab.unipd.it/10906/

[20] R. Hollinger, *Ion Extraction*. John Wiley & Sons, Ltd, 2004, ch. 5, pp. 61–86. [Online]. Available: https://onlinelibrary.wiley.com/doi/abs/10.1002/3527603956.ch5

[21] H. de Esch and L. Svensson, "Negative ion beam halo mitigation at the 1MV testbed at IRFM," *Fusion Engineering and Design*, vol. 86, no. 4, pp. 363–368, 2011. [Online]. Available: https://www.sciencedirect.com/science/article/pii/S0920379611002687

[22] G. Bracco, C. Breton, C. de Michelis, M. Mattioli, and J. Ramette, "High-power neutral-beam angular-divergence evaluation from spectrally resolved Doppler measurements," *J. Opt. Soc. Am.*, vol. 71, no. 11, pp. 1318–1326, Nov 1981. [Online]. Available: http://www.osapublishing.org/abstract.cfm?URI=josa-71-11-1318

[23] C. F. Burrell, W. S. Cooper, R. R. Smith, and W. F. Steele, "Doppler shift spectroscopy of powerful neutral beams," *Review of Scientific Instruments*, vol. 51, no. 11, pp. 1451–1462, 1980. [Online]. Available: https://doi.org/10.1063/1.1136124

[24] G. Orozco, F. Bonomo, N. den Harder, B. Heinemann, A. Hurlbatt, R. Nocentini, R. Riedl, and C. Wimmer, "Design and first results of a retractable 1D-CFC beam target for BATMAN upgrade," *Fusion Engineering and Design*, vol. 165, p. 112225, 2021. [Online]. Available: https://www.sciencedirect.com/science/article/pii/S0920379621000016

[25] W. Ott and F. P. Penningsfeld, "Spectroscopic determination of species and divergence of hydrogen beams in the W7AS neutral beam injectors," Tech. Rep., 1993. [Online]. Available: http://hdl.handle.net/11858/00-001M-0000-0027-6327-F

[26] D. Ciric, H. Falter, J. Fanthome, P. Massmann, and K. Mellon, "Beam profiles measurement using a unidirectional CFC-target and infrared imaging," 1995.

[27] A. Pimazzoni, E. Cescon, M. Dalla Palma, D. Gaule, and G. Serianni, "Thermo-mechanical analysis of unidirectional carbon-carbon composite for thermal imaging diagnostic of a particle beam," *Fusion Engineering and Design*, vol. 146, pp. 2457–2461, 2019, sI:SOFT-30. [Online]. Available: https://www.sciencedirect.com/science/article/pii/S0920379619305526

[28] N. Den Harder, R. Nocentini, G. Orozco, B. Heinemann *et al.*, "The ITER-HNB plasma grid and extraction grid in BUG: Design of a magnetic deflection correction system," Max-Planck-Institute für Plasmaphysik, Tech. Rep., Nov 2020.

[29] T. Kalvas *et al.*, "IBSIMU: A three-dimensional simulation software for charged particle optics," *Review of Scientific Instruments*, vol. 81, no. 2, p. 02B703, 2010. [Online]. Available: http://ibsimu.sourceforge.net/

[30] A. Hurlbatt *et al.*, "The particle tracking code BBCNI for large negative ion beams and their diagnostics," *Plasma Physics and Controlled Fusion*, vol. 61, no. 10, p. 105012, Sep 2019. [Online]. Available: https://doi.org/10.1088/1361-6587/ab3c13

[31] G. Ozorco, private communication.

[32] A. Hurlbatt, N. den Harder, U. Fantz, and the NNBI Team, "Improved understanding of beamlet deflection in iter-relevant negative ion beams through forward modelling of beam emission spectroscopy," *Fusion Engineering and Design*, vol. 153, p. 111486, 2020. [Online]. Available: https://www.sciencedirect.com/science/article/pii/S092037962030034X